Doubly-Strange Hypernuclear Production in E885 at the AGS

A dissertation
by

Pavel Khaustov

Submitted to the Physics Department
in partial fulfillment of the requirements for the degree of

Doctor of Philosophy

Carnegie Mellon University

May, 1999

Abstract

The Alternating Gradient Synchrotron (AGS) D6 1.8 GeV/c K^- beam line and 48D48 spectrometer have been used to accumulate the largest-to-date data sample of strangeness=-2 producing (K^-,K^+) reaction on a diamond target. A total of about 3×10^5 (K^-,K^+) events have been collected and analyzed. Various S=–2 hypernuclear states are expected to be produced either directly or via Ξ^- capture at rest on carbon:

$$\begin{aligned} K^- + {}^{12}\mathrm{C} &\rightarrow K^+ + \left\{ {}^{12}_{\Xi}\mathrm{Be}^*,\ {}^{12}_{\Lambda\Lambda}\mathrm{Be}^* \right\}, \\ K^- + {}^{12}\mathrm{C} &\rightarrow K^+ + X + \Xi^-,\ \ (\Xi^-, {}^{12}\mathrm{C})_{\mathrm{atom}} \rightarrow {}^{12}_{\Lambda\Lambda}\mathrm{B}^* + n. \end{aligned}$$

The directly produced ${}^{12}_{\Xi}$Be and ${}^{12}_{\Lambda\Lambda}$Be hypernuclear states can be identified through the reconstruction of the missing mass. The measurement of the neutron energy in coincidence with production of a free Ξ^- can be used to find the masses of ${}^{12}_{\Lambda\Lambda}\mathrm{B}^*$ hypernuclear states and branching ratios of their formation via Ξ^- capture on carbon.

The measurement of missing mass in E885 indicates the existence of a signal below the threshold of free Ξ^- production, which could not be explained by background or effects of limited resolution. Although the resolution is not sufficient to observe discrete hypernuclear states as peaks, the excess of events in the region of missing mass, kinematically inaccessible in free Ξ^- production, can be compared with theoretical predictions. A good agreement between the data and theory is achieved for a Ξ-nucleus potential well depth $V_{0\,\Xi}$ of about 16 MeV.

An upper limit on the cross section of direct production of double-Λ hypernuclei, averaged over $\theta < 14^\circ$, has been set to be about 6.5 nb/sr for the ground state and 10.2 nb/sr for a 10 MeV excitation state.

The neutron spectrum showed no apparent peaks from the neutron-emission channel of double-Λ-hypernuclear formation from $(\Xi^-, {}^{12}\mathrm{C})_{\mathrm{atom}}$. The upper limit on the branching ratio of the above process has been set to be at or below 4% in the region of expected neutron energies.

Acknowledgements

First I would like to thank my advisor, Gregg Franklin, for the guidance and support he gave me throughout the course of the analysis and for his invaluable advise, both in academic and everyday practical matters. Gregg's office door was always "open".

Curtis Meyer, who advised me during the preparation stage of the experiment, introduced me to the Medium Energy Group and made me feel welcome. His contribution to my education is greatly appreciated.

The success of the experiment is in a large part due to my fellow E885 graduate students, Mike Landry and Kazuhiro Yamamoto.

I am grateful to Alain Berdoz and Dan Carman, who worked hard to set up the experiment and keep it running.

Brian Quinn built and set up the Secondary Level Trigger and was the mastermind behind the DAQ setup. Brian was always available for consultations, even during his skiing trip to Europe.

I thank Al Biglan for his designing the electronics for the CCD readout and building and testing the prototypes.

Morgan May shared his unique experience in the field of strangeness physics and his ideas with the collaboration. His active role in defining the directions of the analysis and his contributing ideas during the course of the analysis are greatly appreciated.

Rich Magahiz should be credited with determining the initial set of Second Level Trigger cuts.

Bernd Bassaleck's neutron detector simulation was indispensable in the course of the analysis. Bernd's energy always cheered people up.

The unrelenting concern of Kent Paschke in the well-being of the neutron detectors and associated electronics and his leadership in the neutron detector calibration resulted in clean and manageable neutron data.

My discussions with Phil Koran helped me advance my analysis at a greater rate.

Our conversations with Rod McCrady made our shared windowless office at CMU much more bearable.

Adam Rusek provided excellent on-site support. His help during the setup and running of the experiment was essential.

Reinhard Schumacher's help during the run and his input on the analysis presentation are greatly appreciated.

Gary Wilkin, our expert technician, built the scintillating fiber detector and helped me and guided me on every step of building the scintillating detector calibration system.

I thank Kim Minihan for her logistics support.

The success of the experiment is also due to all other members of the collaboration.

Finally I thank my wife Galya for her patience and support during all these years.

E885 Collaboration List

D. Alburger, R. E. Chrien, M. May, P. H. Pile, A. Rusek, R. Sawafta[1], R. Sutter
Brookhaven National Laboratory, Upton, New York 11973, USA

A. R. Berdoz[2], A. Biglan[3], D. Carman, G. B. Franklin, P. Khaustov, P. Koran,
R. Magahiz[4], R. McCrady[5], C. A. Meyer, K. Paschke,
B. P. Quinn, R. A. Schumacher
Carnegie Mellon University, Pittsburgh, Pennsylvania 15213, USA

T. Burger, H. Fischer, J. Franz, H. Schmitt
Fakultät für Physik, University of Freiburg, D-79104 Freiburg, Germany

T. Iijima
KEK, High Energy Accelerator Research Organization, Tsukuba, Ibaraki 305, Japan

V. Zeps
University of Kentucky, Lexington, Kentucky 40507

A. Ichikawa, K. Imai, Y. Kondo, K. Yamamoto, M. Yosoi
Kyoto University, Sakyo-ku, Kyoto 606, Japan

F. Takeuchi
Kyoto Sangyo University, Kyoto 603, Japan

F. Merrill
Los Alamos National Laboratory, Los Alamos, New Mexico 87545, USA

C. A. Davis, L. Gan[7], M. Landry, L. Lee, S. A. Page,
W. D. Ramsay, W. T. H. van Oers
University of Manitoba, Winnipeg, Manitoba R3T 2N2, Canada

B. Bassalleck, J. Lowe, R. W. Stotzer[8]
University of New Mexico, Albuquerque, New Mexico 87131, USA

---

[1]Present address: A&T State University, Greensboro, North Carolina 27411, USA
[2]Present address: SFA Inc., Largo, Maryland 20774, USA
[3]Present address: Union Switch & Signal, Pittsburgh, Pennsylvania 15219, USA
[4]Present address: Syncsort Inc., Woodcliff Lake, New Jersey 07675, USA
[5]Present address: Los Alamos National Laboratory, Los Alamos, New Mexico 87545, USA
[7]Present address: Hampton University, Hampton, VA 23668, USA
[8]Present address: ASAP, Albuquerque, NM 87110, USA

Contents

Chapter 1

S=−2 hypernuclei

1.1 Baryon-baryon interaction at low energies

The perturbative approach to solving QCD does not work at low energies due to the non-perturbative nature of strong interactions at low energies. The lattice QCD calculations have had only limited success, managing to predict the masses of the ground state hadrons (see, for example [1]). This situation has caused the creation of many models, whose validity and predictive power have to be tested in experiments.

The potential models for the nucleon-nucleon (NN) interaction fit an extensive volume of available bound state and scattering data very well [2]. The complications of the many-body problem are replaced by a one-body local potential $V_N(r)$.

Due to the lack of experimental data, a new approach is needed to build a model for hyperon-nucleon (YN) and hyperon-hyperon (YY) interactions. Physics considerations must be used to extend the available experimental knowledge on NN and YN interactions to the areas where no experimental data exists.

Several One-Boson Exchange (OBE) models, utilizing symmetry considerations combined with available NN and very limited ΛN [3] and ΣN [4] scattering data, have appeared: first, Nijmegen D and F hard core models and a soft core model [5], and, later, Jülich models A and B [6]. The new models treat baryon-baryon (BB) interactions in a unified manner. As implied by their name, the BB interaction is described by an exchange of nonets of pseudoscalar (π, η, η', K), vector (ρ, ω, ϕ, K^*) and scalar (a_0, ϵ, f_0, K_0^*) mesons. The coupling constants are derived from data and symmetry considerations: flavor SU(3) and spin-flavor SU(6) for Nijmegen and Jülich models respectively. The experimentally observed short range repulsion, which is not reproduced by OBE mechanism, is implemented in these models by introducing hard (or soft) cores. The progress is ongoing and the Nijmegen group recently presented their new OBE soft-core model [7].

The high number of competing models reflects the lack of experimental data and resulting remaining ambiguity.

1.2 Hypernuclear spectroscopy

The short, of the order of 100 ps, life times of the strange baryons (hyperons) make the construction of low-energy (corresponding to non-perturbative QCD region) hyperon beams not feasible. There are, however, attempts to compliment the the bubble chamber ΛN and ΣN scattering data using a new scintillating fiber technique [8], where rate limitations of bubble chambers no longer apply. Therefore, observing hypernuclei (nuclei with one or more hyperons) seems to be the best way to expand our knowledge of the YN and YY interaction.

The OBE models describe the two-body BB interaction in free space, from which effective BB interaction in the nuclear medium (G-matrix) and baryon-nucleus single-particle potential are derived. It is the single-particle potential that is measured in experiments and so the underlying OBE models are tested. Hypernuclear spectroscopy offers an insight into the BB interaction.

The effective BB interaction is usually decomposed into the central, spin-spin, spin-orbit and tensor parts:

$$V(r) = V_c(r) + V_\sigma \sigma_{\mathbf{1}} \cdot \sigma_{\mathbf{2}} + V_1 \mathbf{l_{12}} \cdot \sigma_{\mathbf{1}} + V_2 \mathbf{l_{12}} \cdot \sigma_{\mathbf{2}} + V_T[3(\sigma_{\mathbf{1}} \cdot \mathbf{r})(\sigma_{\mathbf{2}} \cdot \mathbf{r}) - 3\sigma_{\mathbf{1}} \cdot \sigma_{\mathbf{2}}],$$

where $\sigma_{\mathbf{1,2}}$ are Pauli spin matrices, $\mathbf{l}$ and $\mathbf{r}$ are the relative angular momentum and coordinate.

The ultimate goal of hypernuclear spectroscopy is a high-resolution measurement of hypernuclear states with consequent determination of all central, spin-orbit, spin-spin and tensor strengths of the interaction. Experimental difficulties, however, make it an impossible task to accomplish in a single experiment. Although an important insight is gained with only a knowledge of the potential well depth, the measurement of the weaker spin-dependent interaction strength should prove to be invaluable in constructing the comprehensive model of BB interaction at low energies. Magnetic spectrometer resolution is limited to a few MeV and the hypernuclear γ-ray experiments that have the advantage of much higher resolution (of the order of 1 keV for Ge detector) are well positioned to achieve the goal of the determination of spin-dependent (spin-orbit, spin-spin and tensor) interaction strengths.

Information on the hypernuclear states can be gained in several ways:

- Direct-production-type experiments give the energy of the produced hypernuclei by determining missing mass,
- Detection of hypernuclear γ-rays allows the high resolution determination of the hypernuclear states spacing,
- Measurement of the energy of the pion from the mesonic decay of Λ hypernuclei will give its ground-state energy,
- Detection of the neutron from, for example, $(\Xi^-, {}^{\mathrm{A}}\mathrm{Z})_{\mathrm{atom}} \rightarrow {}^{\mathrm{A}}_{\Lambda\Lambda}(\mathrm{Z}-1) + \mathrm{n}$ will give the binding energy of the Λ's.

1.2.1 S=–1 hypernuclei

The Λ hypernuclei are the best studied of all hypernuclei, due to the relatively high cross section of direct production in strangeness-exchange (K^-,π^-), (K^-,π^0) and (π^+,K^+) reactions through elementary processes:

$$\begin{aligned} K^- + n &\rightarrow \Lambda + \pi^-, \\ K^- + p &\rightarrow \Lambda + \pi^0, \\ \pi^+ + n &\rightarrow \Lambda + K^+. \end{aligned}$$

All three reactions can populate the same hypernuclear states, but the former pair has a much higher cross section due to much lower momentum transfer and higher elementary cross section. From [9, 10], the differential cross section for ground state Λ hypernuclear production at $\theta = 0^\circ$ is:

- 0.1 mb/sr for $^{12}C(K^-, \pi^-)^{12}_{\Lambda}C$, $p_{K^-} = 800$ MeV/c.
- 0.015 mb/sr for $^{12}C(\pi^+, K^+)^{12}_{\Lambda}C$, $p_{\pi^+} = 1040$ MeV/c.

The Λ potential well depth has been determined to be $V_0^\Lambda \approx 30$ MeV [11]. The spin-dependent part of the ΛN interaction, however, requires further investigation. It is generally believed that the spin-orbit term of ΛN interaction is much smaller that the one for NN interaction. Various measurements, however, disagree on its magnitude. W. Brükner *et al.* [12] set a limit of 0.3 MeV on the energy level splittings between the $(p_{1/2})_\Lambda$ and $(p_{3/2})_\Lambda$ states in $^{16}_{\Lambda}O$. M. May *et al.* [13] found the energy splittings between the $(p_{1/2})_\Lambda$ and $(p_{3/2})_\Lambda$ states in $^{13}_{\Lambda}C$ (Λ coupled to the $J = 0^+$ ^{12}C ground-state core) to be 0.36 ± 0.3 MeV. By detecting γ-rays from $(5/2^+, 2/3^+) \rightarrow 1/2^+$ in $^{9}_{\Lambda}Be$ and observing only a single peak, M. May *et al.* [14] found that the $5/2^+$-$2/3^+$ doublet splitting is less than 0.1 MeV. A (π^+,K^+)$^{89}_{\Lambda}Y$ spectrum [15] and emulsion data of $^{16}_{\Lambda}O$ [16] suggest a considerably larger strength of the spin-orbit interaction.

It can not be excluded, however, that a more sophisticated theoretical treatment may reconcile some of the measurements. For example, a cluster-model calculation of Hiyama [17] reproduce a larger spin-orbit splitting for $^{16}_{\Lambda}O$ and a much smaller one for $^{9}_{\Lambda}Be$.

New results from hypernuclear x-ray experiments are anticipated and expected to add to our understanding of ΛN interaction.

Σ hypernuclei, if they exist, should be produced along with Λ hypernuclei in the (K^-,π^-) reaction through elementary processes:

$$\begin{aligned} K^- + n &\rightarrow \Sigma^0 + \pi^-, \\ K^- + p &\rightarrow \Sigma^+ + \pi^-. \end{aligned}$$

The (K^-,π^+) reaction can be used to probe for creation of Σ hypernuclei via:

$$K^- + p \rightarrow \Sigma^- + \pi^+.$$

The width of Σ hypernuclear states should be naively expected to be much wider than those for Λ hypernuclei due to conversion in the nuclear medium:

$$\begin{aligned} \Sigma^- + p &\rightarrow \Lambda + n, \\ \Sigma^0 + n &\rightarrow \Lambda + n, \\ \Sigma^+ + n &\rightarrow \Lambda + p. \end{aligned}$$

However, the observed peak in the excitation energy distribution for ^{4}He(K^-, π^-)$^4_\Sigma$He below the threshold of free $\Sigma^{0,+}$ production is only $\approx$7 MeV wide [18, 19]. An explanation for this rather narrow conversion width was offered by Harada et al. [20, 21]. They argued that the nuclear core and Σ wave functions overlap was reduced due to the repulsive central part of the 3N-Σ potential and that the binding in the T=1/2 $^4_\Sigma$He state was provided by the strong Lane (isospin-dependent) term.

No such peak was found in the ^{4}He(K^-,π^+)X reaction. T. Harada [21] pointed out that the reaction populates only T=3/2 Σ hypernuclear states and that there are no nuclear bound states due to a repulsive core in the potential for T=3/2.

1.2.2 S=–2 hypernuclei

The S=–2 sector is a totally new territory to test OBE models. The Nijmegen models D and F predict a different sign of ΞN potential well depth [22] ($V_{0\,\Xi}$ = 23 MeV and -28 MeV respectively) and establishing the potential well depth (or merely fact of the Ξ-hypernuclear existence) will be a valuable step towards establishing experimental constraints. The same models predict different strength of $\Lambda\Lambda$ interaction (Y. Yamamoto *et al.* [23] give $\Delta B_{\Lambda\Lambda}$ for $^{13}_{\Lambda\Lambda}$B as 4.67 MeV and -0.08 MeV for Nijmegen models D and F respectively). The Λ-Λ binding energy is defined as the change in the total binding energy of the two Λ's due to the Λ-Λ interaction: $\Delta B_{\Lambda\Lambda} = B_{\Lambda\Lambda} - 2\,B_\Lambda$.

The study of Ξ hypernuclei will add to the understanding of the hyperon-nucleon interaction. The double-Λ hypernuclei shed light on the hyperon-hyperon interaction.

There is very little experimental information on the Ξ and double-Λ hypernuclei. This is explained by the relatively low cross section for Ξ^- production:

$$\sigma_{K^- + p \rightarrow K^+ + \Xi^-}(\theta = 0^\circ) \approx 35\ \mu\text{b/sr},$$

high momentum transfer and the two-step nature of direct double-Λ hypernuclear production:

$$K^- + p \rightarrow K^+ + \Xi^-,\ \Xi^- + p \rightarrow \Lambda + \Lambda,$$

or

$$K^- + p \rightarrow \pi^0 + \Lambda,\ \pi^0 + p \rightarrow \Lambda + K^+.$$

A. J. Baltz *et al.* [24] predicted the cross section of direct double-Λ production in the reaction $^{16}\mathrm{O}(\mathrm{K}^-,\mathrm{K}+)^{16}_{\Lambda\Lambda}\mathrm{C}^*$ to be a few nb/sr for $p_{K^-} = 1.1$ GeV/c. Cross sections can be expected to be higher for the incident K^- momentum of 1.8 GeV/c because 1.1 GeV/c is below threshold for Ξ^- production while 1.8 GeV/c is at the peak of the two-body Ξ^- production cross section [25]. C. B. Dover *et al.* [26] pointed out the possibility of Ξ and double-Λ hypernuclear states mixing which would introduce an amplitude for direct one-step double-Λ hypernuclear production and could make the cross section of double-Λ hypernuclear production considerably larger.

Double-Λ hypernuclei can also be produced by stopping Ξ^-'s with subsequent formation of $(\Xi^-,{}^{\mathrm{A}}\mathrm{Z})$ atoms and conversion $\Xi^- + \mathrm{p} \to \Lambda + \Lambda$. Again, short lifetime of the Ξ^- results in a high probability of its decay before its stop.

Despite the experimental difficulties, there have been reports of observing double-Λ and Ξ hypernuclei in emulsion exposed to K^- beam. Double-Λ hypernuclei were created via Ξ^- capture by a nucleus, followed by conversion $\Xi^- + \mathrm{p} \to \Lambda + \Lambda$. Ξ hypernuclei were produced directly in the $(\mathrm{K}^-,\mathrm{K}^+)$ reaction. The emulsion's unique qualities, such as great spatial and energy resolution (provided particle identification is correct), are fully utilized when interpreting events with complicated topology and a number of short tracks. However, unique event interpretation is not always possible.

The observed double-Λ hypernuclei and Λ-Λ binding energies are:

- $^{10}_{\Lambda\Lambda}\mathrm{Be},\ \Delta\mathrm{B}_{\Lambda\Lambda} = 4.5\ \mathrm{MeV} \pm 0.4\ \mathrm{MeV}$ [27],
- $^{6}_{\Lambda\Lambda}\mathrm{He},\ \Delta\mathrm{B}_{\Lambda\Lambda} = 4.6\ \mathrm{MeV} \pm 0.5\ \mathrm{MeV}$ [28],
- $^{13}_{\Lambda\Lambda}\mathrm{B},\ \Delta\mathrm{B}_{\Lambda\Lambda} = 4.8\ \mathrm{MeV} \pm 0.7\ \mathrm{MeV}$, or in other interpretation $^{10}_{\Lambda\Lambda}\mathrm{Be}, \Delta\mathrm{B}_{\Lambda\Lambda} = -4.9\ \mathrm{MeV} \pm 0.7\ \mathrm{MeV}$ [29].

In the last experiment, unlike the previous two, the outgoing K^+ is identified and, therefore, the creation of Ξ^- is firmly established. However, there are two interpretations of the last event with opposite signs of the Λ-Λ binding energy. If the former interpretation is the true one, all three observations of double-Λ hypernuclei produce attractive and close values of the Λ-Λ binding energy with the Λ's bound to a nuclear core and in the ground state (relative state $^1S_0$): $\Delta\mathrm{B}_{\Lambda\Lambda} \approx 4$–$5$ MeV.

Variational calculations of α-cluster models for the first two events were carried out by A. R. Bodmer *et al.* [30]. Fixing parameters of the theory using the experimental value of $\Delta\mathrm{B}_{\Lambda\Lambda}$ for the first $^{10}_{\Lambda\Lambda}\mathrm{Be}$ event, they predicted the value of $\Delta\mathrm{B}_{\Lambda\Lambda}$ for $^{6}_{\Lambda\Lambda}\mathrm{He}$ to be about 3.6 MeV or less, depending on the values chosen for other parameters of the theory. This is 1 MeV or more lower than the value found experimentally. This suggests possibility of en experimental error in either $^{10}_{\Lambda\Lambda}\mathrm{Be}$ or $^{6}_{\Lambda\Lambda}\mathrm{He}$ event.

C. B. Dover and A. Gal [31] derived the Ξ^--nucleus potential well depth by fitting the following observations of Ξ hypernuclei in emulsion:

- $^{8}_{\Xi}\mathrm{He},\ \mathrm{B}_{\Xi} = 5.9\ \mathrm{MeV} \pm 1.2\ \mathrm{MeV}$ [32],
- $^{11}_{\Xi}\mathrm{B},\ \mathrm{B}_{\Xi} = 9.2\ \mathrm{MeV} \pm 2.2\ \mathrm{MeV}$ [33],

- ${}^{13}_{\Xi}$C, $B_\Xi = 18.1$ MeV $\pm$ 3.2 MeV [34],
- ${}^{15}_{\Xi}$C, $B_\Xi = 16.0$ MeV $\pm$ 4.7 MeV [35],
- ${}^{17}_{\Xi}$O, $B_\Xi = 16.0$ MeV $\pm$ 5.5 MeV [35],
- ${}^{28}_{\Xi}$Al, $B_\Xi = 23.2$ MeV $\pm$ 6.8 MeV [35],
- ${}^{29,30}_{\Xi}$Mg, $B_\Xi = 2.4$ MeV $\pm$ 6.3 MeV [35].

They obtained the value of 21 MeV $\pm$ 4 MeV or 24 MeV $\pm$ 4 MeV by assuming values for the nucleon size parameter $r_0 = 1.25$ fm or 1.1 fm respectively. The last hypernucleus with abnormally low binding energy was assumed to be in an excited state.

C. B. Dover and A. Gal noted [31]: "None of these interpretations is statistically unique, and in some cases the evidence is far from being compelling".

J. K. Ahn *et al.* recently reported evidence for bound Ξ hypernuclei produced in the (K^-,K^+) reaction on a scintillating fiber target [36]. The comparison of their missing mass spectrum with a theoretical calculation, shown in Figure 1.1, favored the Ξ-nucleus potential well depth $V_{0\,\Xi} \approx 17$ MeV. Based on their estimated error in the determination of the potential depth equal to 2 MeV r.m.s., they concluded that the case of $V_{0\,\Xi} = 24$ MeV is improbable. However, they might have underestimated their systematic error. Due to their very low count of events below zero excitation energy, to estimate the statistical error they integrated their spectrum up to the excitation energy of 7 MeV. This region is fed by both the unbound hypernuclear states production and the quasi-free Ξ^- production processes (their resolution is only 9.5 MeV r.m.s.). The following two points indicate the weak points of their estimate of the systematic error:

- The prediction power of DWIA, which was used to produce the theoretical missing mass spectrum, for those processes might well be considerably worse than the 30% accuracy obtained for the bound or almost bound hypernuclear states produced in lower momentum transfer (K^-,π^-) [9] and (π^+,K^+) [10] reactions.
- The smearing of the spectrum due to the finite experimental resolution must be taken into account when calculating the error. The close proximity to the region of quasi-free Ξ production results in an influx of events into the region of low excitation energy from the quasi-free region of the spectrum and greater error.

Ideally, one needs to measure peaks in the missing mass spectrum to settle the question of the Ξ-hypernuclear existence and strength of the potential. But even a low resolution measurement with an order of magnitude higher statistics could result in a much stronger statement due to

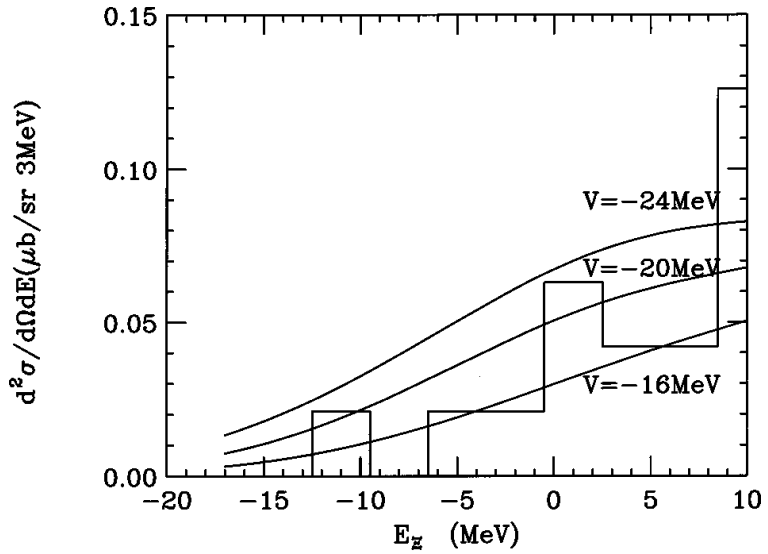

Figure 1.1: Missing Mass spectrum as a function of excitation energy of Ξ^- in ${}^{12}_{\Xi}$Be measured in E224 at KEK. The curves show the theoretical prediction for three values of $V_{0\,\Xi}$ potential. The integration interval is E$\leq$7 MeV and contains 3 events below zero and 7 events above zero excitation energy.

- higher statistics and consequent better statistical error and
- lower systematic error by avoiding the higher excitation energy region of the spectrum.

To summarize, the existing data are far from compelling and high statistics, high resolution measurements are needed to fix the strength of ΞN and $\Lambda\Lambda$ interaction and, possibly, investigate the spin dependence.

1.3 Hypernuclear production in E885 at AGS

In E885, the incident K^- of momentum 1.8 GeV/c strikes a proton bound in a carbon nucleus and a Ξ^- and K^+ are produced:

$$K^- + p \rightarrow K^+ + \Xi^-.$$

The cross section for Ξ^- production at $p_{K^-} = 1.8$ GeV/c on the free proton is ≈ 35 μb/sr at small forward angle. When using nuclear targets, in addition to free Ξ^- production, hypernuclear Ξ and double-$\Lambda\Lambda$ states are accessible as well.

When the final-state Ξ^- is bound, a Ξ hypernucleus is formed. This process is called direct hypernuclear production. Direct hypernuclear production is identified through the reconstruction of missing mass, which leads to the determination of

the hypernuclear state energy. The missing mass resolution in E885 for the reaction $K^- + {}^{12}C \to K^+ + X$ is 6.1 MeV r.m.s. and it is not sufficient to observe hypernuclear states as discrete peaks, but observation of an excess of events in the bound region of the missing mass spectrum would be a clear indication of hypernuclear formation. The direct production of Ξ and double-Λ hypernuclei are studied in E885 via reactions:

$$\begin{aligned} K^- + {}^{12}C &\to K^+ + {}^{12}_{\Xi}Be^*, \\ K^- + {}^{12}C &\to K^+ + {}^{12}_{\Lambda\Lambda}Be^*. \end{aligned}$$

Direct hypernuclear production is not the only mechanism available for hypernuclear production. A sufficiently slow Ξ^- will further slow down through ionization losses and may be captured by a nucleus before it decays. This mechanism was widely used in pre-spectrometer era emulsion experiments. In E885, direct production and nuclear capture mechanisms compliment each other. The advantage of direct production is the direct observation of energy levels, the disadvantage being a relatively low yield, compared to the nuclear capture, due to the low cross section. The following mechanism of double-Λ hypernuclear formation via Ξ nuclear capture at rest is studied in E885:

$$K^- + {}^{12}C \to K^+ + X + \Xi^-, \ (\Xi^-, {}^{12}C)_{\rm atom} \to {}^{12}_{\Lambda\Lambda}B^* + n.$$

These reactions can be approximately treated as if the target proton was free and the nuclear core was a spectator. The production of unbound Ξ^-'s on nuclear ($A > 2$) targets is often referred to as "quasi-free Ξ^- production". The most sophisticated approximation technique to-date describing the hyperon production on nuclear targets, both for bound and unbound final states, is called the Distorted Wave Impulse Approximation (DWIA). A short description of DWIA is given in Appendix B. In the S=–1 sector the DWIA calculations were found to reproduce the experimental cross sections for (K^-,π^-) and (π^+,K^+) reactions with $\approx$30% accuracy. Using DWIA, a connection between the potential and observed hypernuclear states can be made.

Chapter 2

Experimental Setup

2.1 Overview

E885 employed the (K^-,K^+) reaction to create strangeness S=−2 systems. The incident K^- beam is produced by striking the platinum production target with high energy protons and selecting and transporting secondary kaons through the beam line. Since particles of many types and various momenta are produced on the production target, the beam line is essential to select particles of the certain momentum and type. 100% particle content purity is not attainable and some contamination is unavoidable. Typical K^- beam parameters during the run were $0.5 - 1.0 \times 10^6$ K^-'s/spill with 1:1 K/π ratio. The side view of the apparatus downstream of the beam line is shown in Figure 2.1. The momentum of the incident particle is measured using information from the MT+MP scintillator hodoscope located in the beam line and information from 3 drift chambers (ID1-3) located immediately after the beam line. Given the particle momentum, the amplitude in the IC Cherenkov counter and the beam line time-of-flight are used to suppress pions.

The momentum of the K^+ is measured in the 48D48 spectrometer. Similarly to the case of the incident particle, amplitude in the FC Cherenkov counter along with the measured momentum and time-of-flight is used to select kaons. In addition to pions, protons are another source of background in the spectrometer. To reduce hardware trigger rate, an aerogel Cherenkov counter with high refraction index, FC0, is used to suppress protons. The measured momenta of the incident and secondary particles allow calculation of the missing mass.

All the detectors were assigned two-letter names, where the first letter designates the location and the second letter does the detector type. There are several regions:

- mass slit region includes detectors in the beam line and has the corresponding letter designation M;
- "incident" region includes detectors downstream of the last beam line quadrupole magnet Q9 and upstream of the target and has the corresponding letter designation I;

- "forward" region includes detectors downstream of the the target and upstream of the spectrometer's magnet and has the corresponding letter designation F;
- "back" region includes detectors downstream of the spectrometer's magnet and has the corresponding letter designation B.

The detectors types and corresponding letter designations are:

- scintillator hodoscopes – P,
- scintillator detectors used for timing – T,
- Cherenkov detectors – C,
- drift chambers – D,
- gas microstrip chambers – M.

The gas microstrip detectors were not used in this analysis. Other detectors which did not conform to this naming scheme were Neutron Detector (ND) and scintillating fiber detector (SCIFI).

The coordinate system has the z-axis pointing along the beam direction, the y-axis pointing upward and the x-axis pointing to the left if looking downstream. The origin of the coordinate system was chosen so that the center of the beam has $x = 0$ and $y = 0$ and the z coordinate of the origin is 200 cm upstream of the spectrometer's magnet center. The center of the target has the coordinates $x = 0$ cm, $y = 0$ cm and $z =$ -20 cm.

2.2 D6 Beam Line

The D6 beam line [37], shown in Figure 2.2, is used to transport negative kaons to the experimental area. The kaons are produced as a result of interaction of high energy protons with the production platinum target. Two stages of electrostatic separation result in a clean kaon beam with a K/π ratio of about 1:1 at the central beam momentum of 1.8 GeV/c and momentum spread of about 150 MeV. Momentum of the incident particle is determined from measurements made by the MP beam line hodoscope and the ID1-3 drift chambers.

2.3 Scintillator detectors

2.3.1 MP and MT beam line scintillator detectors

The horizontal position of the beam in the beam line is measured by the MP scintillator hodoscope which consists of 72 rectangular elements overlapping by 1/3 of their

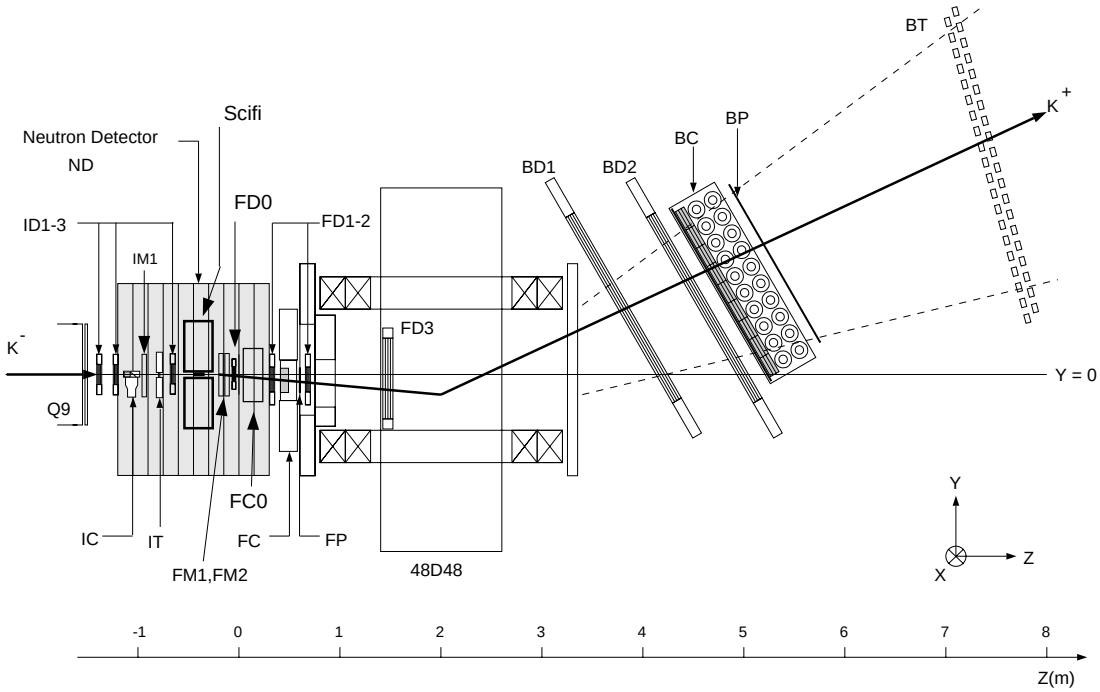

Figure 2.1: Detector configuration for E885. The drift chambers ID1-3 determine K^- trajectory and, combined with the beam line hodoscope MP (not shown here), the K^- momentum. Drift chambers FD0-3, BD1-2 determine the K^+ trajectory through the spectrometer. Scintillators IT and BT determine the K^+ time-of-flight. Hodoscopes FP and BP determine the spectrometer acceptance. Aerogel Cherenkovs IC, FC, and BC reject pions, while FC0 rejects protons. Above and below the target are the scintillating fiber detectors. On the left and right of the target are the neutron detectors.

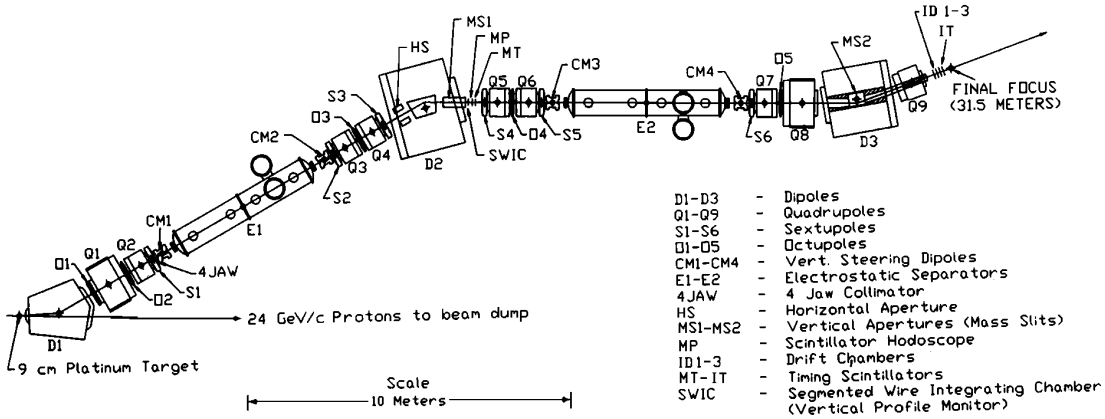

Figure 2.2: Plan view of the D6 beamline at the BNL AGS.

detector name	single element dimensions, cm			overall detector dimensions, cm		number of elements
	x	y	z	x	y	
MP	0.7	1.5	0.3175	33.0	1.5	72
MT	3.7	1.5	0.635	33.0	1.5	9
IT	2.5	3.0	0.635	10.0	3.0	4
FP	24.0	1.5	0.4	24.0	24.0	16
BP	21.0	180.0	1.27	126.0	180.0	6
BT	200.0	8.5	5.0	200.0	330.0	40

Table 2.1: Scintillator detectors parameters.

widths with the elements on each side. Each element is viewed by a single 0.525-inch R647-01 photomultiplier coupled through an adiabatic light guide. Timing is provided by the MT scintillator detector, which is segmented horizontally similarly to MP but built of elements larger in x and z dimensions and has only 9 elements. The segmentation reduces the counting rate of a single element and allows background suppression by requiring correlation between the MP and MT elements that are hit in a particular event. Each MT element is viewed directly by two 2-inch RCA8575 photomultipliers. Dimensions of the detectors are given in Table 2.1.

2.3.2 IT scintillator counter

Time reference is provided by the IT scintillator counter positioned in the path of the incident beam. The detector consists of four elements, each element is viewed by two 2-inch RCA8575 PMTs through short light guides with the same cross-section as

the scintillator. Similar to MT and MP the segmentation is horizontal. Dimensions of the detector are presented in Table 2.1.

2.3.3 FP scintillator hodoscope

To maintain reasonable DAQ live time, the trigger requirement demands that only the events with the secondary particle likely to be within the spectrometer acceptance and far enough from the beam are allowed to cause triggers. The FP scintillator hodoscope, which is segmented in the y direction serves to select such reaction products. FP consists of 16 scintillator counters. Each counter has dimensions 24.0 cm×1.5 cm×0.4 cm. The overall hodoscope dimensions are 24.0 cm×24.0 cm×0.4 cm. Each element is viewed by two 1-inch Hamamatsu H3167 photomultipliers.

2.3.4 BP scintillator hodoscope

The BP scintillator hodoscope is located in the back spectrometer region behind the BD2 drift chamber. BP defines the acceptance of the spectrometer in the back region and ensures that all accepted particles have passed through the larger-area back aerogel Cherenkov detector BC. BP is segmented in the x-direction and consists of 6 counters, each with dimensions 21 cm×180 cm×1.27 cm. It is inclined by 30° with respect to the y-axis. Each hodoscope element is viewed by two 2-inch Amperex XP2262 photomultipliers.

2.3.5 BT time-of-flight wall

The BT scintillator hodoscope is the last detector and is designed to measure the position and time-of-flight. Kaon decays are further suppressed by placing a cut on the residual of the track segment measured by the BD drift chambers projected onto BT. Measurement of the secondary particle momentum, track length and time-of-flight allow reconstruction of its mass. The hodoscope consists of 40 scintillator logs with dimensions 200.0 cm×8.5 cm×5.0 cm. Each log is viewed by two 2-inch H1949 Hamamatsu photomultipliers.

2.4 Wire chambers

2.4.1 ID1-3 drift chambers

The ID1-3 drift chambers measure the incident particle track in the region between the Q9 magnet and the target. Each chamber consists of three double planes rotated by 60° with respect to each other with 48 wires in a double plane and the wire spacing of 0.508 cm. The wires in the three planes are strung in the following directions:

$\hat{\mathbf{y}}$, $\hat{\mathbf{x}}\cos(30^\circ) + \hat{\mathbf{y}}\sin(30^\circ)$ and $\hat{\mathbf{x}}\cos(150^\circ) + \hat{\mathbf{y}}\sin(150^\circ)$. Use of double planes with one plane shifted by a half of wire spacing allows the resolution of the hit position ambiguity and is critical for rejection of accidental coincidences in this high-rate environment.

2.4.2 FD0-3 drift chambers

The FD0-3 drift chambers measure the secondary particle track in the region between the target and the magnet. The magnet's fringe field is neglected for the purpose of the track fitting and FD0-2 hits are fitted with a straight line. FD0-2 are similar to ID1-3 but rotated by 90° around the z-axis relative to ID1-3 and about twice as large in order to intercept the scattered particles. The FD1-2 chambers consist of three double planes rotated by 60° with respect to each other with 96 wires in a double plane and the wire spacing of 0.508 cm. The wires in the three planes are strung in the following directions: $\hat{\mathbf{x}}$, $\hat{\mathbf{x}}\cos(60^\circ) + \hat{\mathbf{y}}\sin(60^\circ)$ and $\hat{\mathbf{x}}\cos(120^\circ) + \hat{\mathbf{y}}\sin(120^\circ)$. FD0 has only one double plane with 48 wires strung in the x direction.

The FD3 drift chamber has a rectangular frame to match the magnet gap. It has 4 wire planes, a double plane strung in the x direction and two single planes in the following directions: $\hat{\mathbf{x}}\cos(60^\circ) + \hat{\mathbf{y}}\sin(60^\circ)$ and $\hat{\mathbf{x}}\cos(120^\circ) + \hat{\mathbf{y}}\sin(120^\circ)$.

2.4.3 BD1-2 drift chambers

The track of the secondary particle in the back area is measured by the BD1-2 drift chambers. The chambers have a total of 9 drift planes. The wires are strung in the following directions: $\hat{\mathbf{x}}$, $\hat{\mathbf{x}}\cos(30^\circ) + \hat{\mathbf{y}}\sin(30^\circ)$ and $\hat{\mathbf{x}}\cos(150^\circ) + \hat{\mathbf{y}}\sin(150^\circ)$. This measurement in conjunction with the track measurement before the spectrometer magnet is used to determine the particle momentum. The momentum is determined by requiring the two segments, before and after the magnet, to match, given the spectrometer magnet field between the two.

2.5 Cherenkov detectors

2.5.1 IC and FC Cherenkov detectors

Both IC and FC detectors are used for K/π separation and are located near the target. Their radiators are made of silica aerogel. The IC Cherenkov detector is placed between the drift chambers ID1 and ID2. The radiator is made of 3 pieces of aerogel with an index of refraction n=1.029. Dimensions of a single piece are 10.0 cm×5.0 cm×2.0 cm. Overall radiator dimensions are 10.0 cm×5.0 cm×6.0 cm. Cherenkov light is detected by a single 5-inch Hamamatsu R1250 photomultiplier.

The FC Cherenkov detector is placed between the drift chambers FD1 and FD2. The radiator is made of 16 pieces of aerogel with the index of refraction n=1.037. Di-

mensions of a single piece are 11.5 cm×11.5 cm×2.0 cm. Overall radiator dimensions are 23.0 cm×23.0 cm×8.0 cm. Cherenkov light is detected by 4 3-inch Hamamatsu R5543 fine mesh photomultipliers.

2.5.2 BC Cherenkov detector

To suppress pions from the (K^-,π^+) reaction and pions from kaon decays occuring before the BD drift chambers in the back of the spectrometer another Cherenkov detector, named BC, was used. It is located in the back area after the BDs and before the BT time-of-flight wall. The radiator is made of 162 aerogel pieces with the index of refraction n=1.04. Dimensions of a single piece are 21.0 cm×21.0 cm×3.0 cm. Overall radiator dimensions are 126.0 cm×189.0 cm×9.0 cm. The aerogel is viewed by 40 5-inch RCA8854 photomultipliers.

2.5.3 FC0 Cherenkov detector

The FC0 Cherenkov detector is placed between the drift chambers FD0 and FD1 and is used for K/p separation. The radiator is made of 8 aerogel bars with the index of refraction varying from n=1.136 for the top one down to n=1.107 for the bottom one. Dimensions of a single element are 13.0 cm×1.8 cm×3.6 cm. Overall radiator dimensions are 13.0 cm×14.0 cm×3.6 cm. The aerogel is viewed by 8 2-inch Hamamatsu H1161Q photomultipliers.

2.5.4 Target

The production carbon target was made of synthetic diamond with the dimensions 8 cm×1 cm×5 cm. The denser diamond was chosen over graphite in order to achieve a higher Ξ^- stopping rate.

2.6 Scintillating Fiber (SCIFI) detector

To observe charged particles around the target two SCIFI arrays, shown in Figure 2.3, are placed above and below the target. Bicron BCF-12 single cladding 1 mm×1 mm square scintillating fiber was used. The fiber core is made of polystyrene and the cladding of acrylic. Some fiber characteristics are provided in Table 2.3. Each of the two SCIFI arrays consists of 100 fiber layers with 76 fibers per layer. BC-600 Optical Cement was used to glue fibers in a layer. Each fiber layer has an estimated 50μm-thick layer of glue on only one side. The layer orientation alternates successively by 90°. The region where the layers of different orientation cross, a two-projection view is provided. From two projections in this region, a full 3-dimensional track can be reconstructed.

Scintillation light is detected by 4 Image Intensifiers (IITs) (Figure 2.4), 2 per SCIFI array. IITs provide an amplified optical image of the event. Two Delft IITs and two Hamamatsu IITs are used to read out SCIFI arrays, two IITs per SCIFI array. Both types have 3 amplification stages, first stage being electrostatic one. The second and third stages incorporate Micro-Channel Plates (MCP) and are gateable. The first stage has constant 20 kV voltage applied to it. Although the first stage has a modest gain, it serves a very important purpose – amplification of a weak signal to the degree that the second IIT stage has a few photoelectrons. This is important because the MCP has a substantial inefficiency due to the significant probability that a photoelectron will not strike the internal surface of a channel and will not create an avalanche. It also does demagnification to match the smaller size input window of the second IIT stage. Gating the second and third stages by the experimental trigger prevents the IIT image from saturating with background. The second IIT stage is gated by the first level trigger and the third stage by the second level trigger. P-24 type phosphor is used in the first stage and P-20 type phosphor in the second and third stages. The phosphor decay time varies with the signal width. Defined as a time after which the phosphor brightness is 10% of the initial, the decay time is 3μs–40μs for P-24 and 10μs– 0.6 ms for P-20. The lower value is for the input pulse duration of 100 ns and the upper for 1 ms. The relatively fast P-24 phosphor in the first stage helps reduce the background resulting from event pile-up and the slower P-20 phosphor is needed to retain the image while the second level trigger decision is made. The second stage IIT gate width was 3μs and 2μs for Hamamatsu and Delft respectively and the third stage IIT gate was 150 μs for both Hamamatsu and Delft. Having found that the image quality degenerates at trigger rates higher than 60 Hz, an additional IIT trigger hold-off of 15 ms was added to keep the rate sufficiently low. Characteristics for the IITs used in the experiment are summed up in Table 2.2.

The Dalsa CA-D1 CCD cameras with resolution of 256×256 pixels are used to digitize the optical image from the last phosphor of the IITs. The image sensor of the camera has the dimensions of 4.096 mm×4.096 mm. Lenses between the IIT output window and the camera are used to demagnify and focus the optical image on the camera's image sensor. The cameras ran at their maximum frame rate of 203 frames per second. Only frames strobed by the IIT trigger are sent to the data acquisition system and written to tape. The SCIFI event included the line and pixel number at the time of the trigger to be able to allow inference of the timing of the trigger with respect to the frame. On average, half of all events have associated IIT images. This is due to the higher dead time imposed on the IIT trigger rate to keep images of a satisfactory quality.

2.7 Neutron detector

The neutron detector provides high detection efficiency (≈10%) and high timing resolution in a wide range of neutron energies. This is achieved by arranging 100 scin-

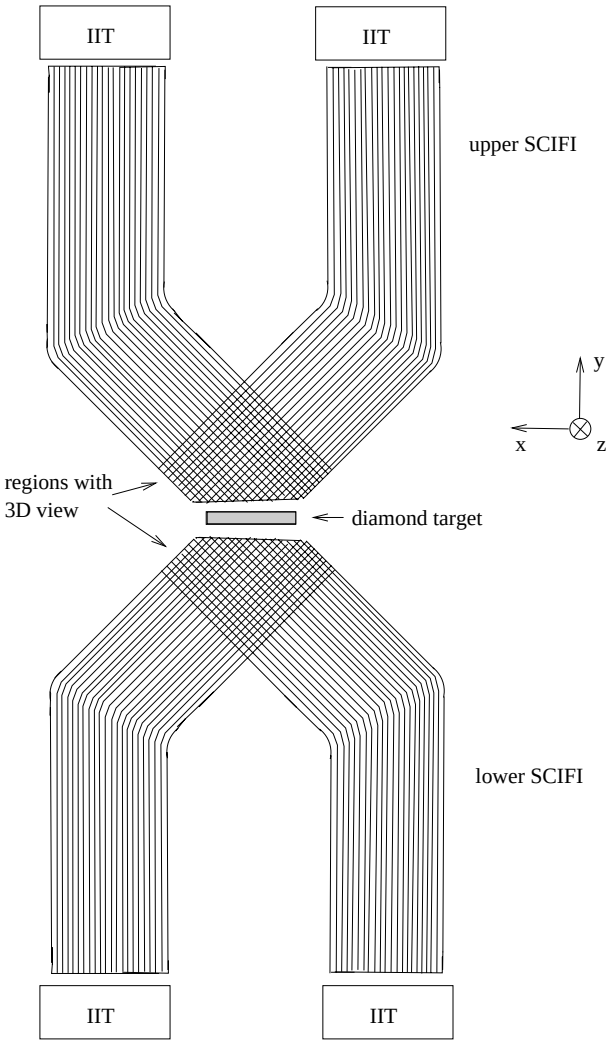

Figure 2.3: Schematic view of the SCIFI detector. Two SCIFI arrays, above and below the target, detect charged particles in the proximity of the diamond target. There are 100 fiber layers in each SCIFI stacked along the z-axis. Orientation of the fiber layers alternates by 90° to provide two projections. In the regions where the fiber layers cross, a 3-dimensional reconstruction of the tracks is done. Each arm of a SCIFI detector is viewed by an image intensifier.

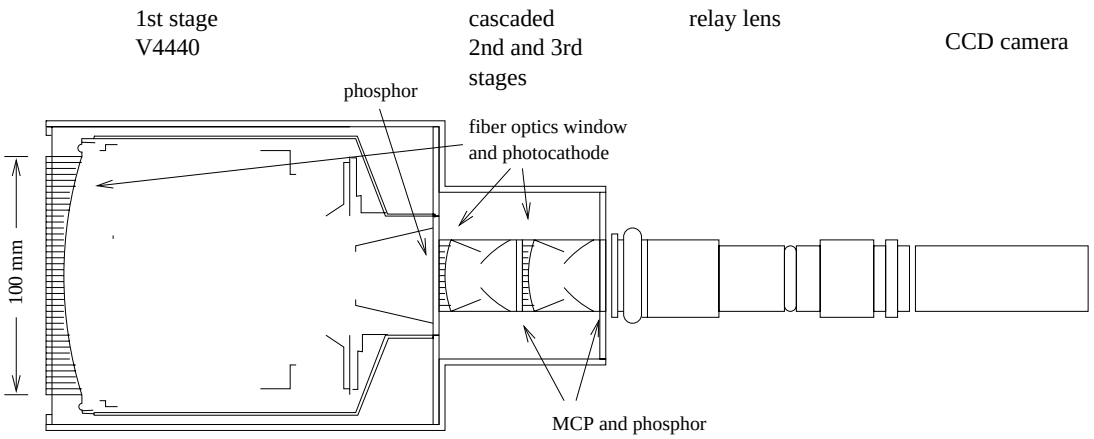

Figure 2.4: Schematic view of the IIT system (Hamamatsu IIT shown). Light from the SCIFI illuminates the 1st IIT stage photo-cathode through the fiber optics input window and resulting photoelectrons are accelerated in the electric field and strike the phosphor. Further amplification occurs in the cascaded 2nd and 3rd stages, which incorporate Micro-Channel Plates (MCP). The last two stages are gated by the experimental trigger to prevent pile-up. Optical image from the last phosphor is focused by the relay lens on the CCD camera image sensor. The camera digitizes the images at the rate of 203 frames per second and sends them to the data acquisition system.

IIT type	photon gain [a]		phosphor type		input and output window diameter, mm	
	stage 1	stages 2,3	stage 1	stages 2,3	stage 1	stages 2,3
Hamamatsu V4440	10 [b]	3×10^3 [c]	P-24	P-20	100, 25	25, 25
Delft PP0040C	$\geq$8 [d]	10^3 [e]	P-24	P-20	80, 16	16, 16

Table 2.2: Parameters of the image intensifiers

.

[a] Defined as the ratio of the number of photons at the output and input windows.
[b] At cathode-anode voltage = 20 kV.
[c] At MCP voltage = 900 V.
[d] At cathode-anode voltage = 20 kV.
[e] At MCP voltage = 750 V.

Fiber	emission color	emission peak, nm	attenuation length, m	core refractive index	cladding refraction index	photons per MeV [a]
BCF-12	blue	435	2.2	1.60	1.49	8000

Table 2.3: Scintillating fiber parameters.

[a] For minimum ionizing particle.

tillator logs with dimensions 5.08 cm×182.9 cm×15.24 cm vertically in two stacks one on each side of the target, as shown in Figure 2.5. Each log is viewed by one photomultiplier on each end. Their mean time provide the time-of-flight information and time difference coordinate along the log. A layer of veto counters on each side is used for charged particle identification. Neutrons usually appear as isolated hits in the bulk of the detector. If a veto counter in the line of flight fired, the hit is declared to be caused by a charged particle and discarded. A clustering algorithm is used to associate adjacent hits with a single neutron.

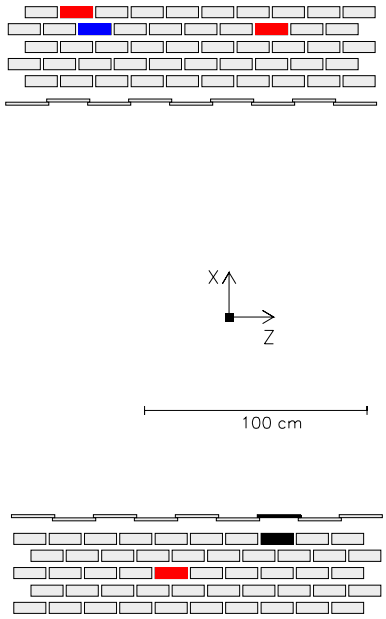

Figure 2.5: Plan view of the neutron detector. One hundred signal scintillator logs and 18 veto counters are set up vertically on the target's two sides. Incident particle line of flight is along the z-axis. The target is shown as a solid rectangle at the origin.

A relatively busy event, shown in Figure 2.5, was chosen to demonstrate different kinds of hits: isolated neutron hits with a single scintillator log fired, a neutron causing a cluster of 2 adjacent logs to fire and a charged hit. The neutron energy is determined by its time-of-flight and distance between the target and the center of the log that fired.

2.8 Trigger

E885 trigger consists of two stages called first level trigger and second level trigger. Both of them were implemented in hardware. The first level trigger uses discriminated signals from scintillator and Cherenkov detectors for rough event categorization. The second level trigger correlated BT y-position and time-of-flight to FD3 pattern in

order to suppress (K^-,p) events which had been found to be the main background source to the (K^-,K^+) trigger. The proton from the (K^-,p) process, which has a much higher cross section than the cascade production, can fire FC0 with some probability and thus mimics a (K^-,K^+) event. Also, such a proton can be accompanied by a pion or pions that fire FC0.

2.8.1 First level trigger

Various logical combinations of discriminated signals from the scintillator and Cherenkov detectors form the first level triggers. The detector names are used to designate a logical signal from the detector. Signal from IT represents a beam particle which is categorized as either a "kaon" or "pion", depending on whether the IC Cherenkov counter fired or not. Hence "Kbeam" and "πbeam" trigger definitions:

$$\begin{aligned} \text{Kbeam} &= \text{IT} \cdot \overline{\text{IC}} \\ \pi\text{beam} &= \text{IT} \cdot \text{IC} \end{aligned}$$

The IT signal is an OR of its 4 elements. Similarly, the scattered particle is categorized as either a "kaon" or "pion".

$$\begin{aligned} \text{Kscat} &= \text{FP} \cdot \text{BP} \cdot \text{FC0} \cdot \overline{(\text{FC} \cdot \text{BC})} \\ \pi\text{scat} &= \text{FP} \cdot \text{BP} \cdot (\text{FC} + \text{BC}) \end{aligned}$$

The FP signal is the logical OR of signals from elements 1 through 12 - the part just below the beam. The BP signal is the logical OR of signals from its 6 elements. The Cherenkov detector signals are discriminated signals of the analog sum of all photomultipliers viewing the aerogel. The combinations above are used to form "πK", "Kπ" and "KK" triggers:

$$\begin{aligned} \text{KK} &= \text{Kbeam} \cdot \text{Kscat} \\ \pi\text{K} &= \pi\text{beam} \cdot \text{Kscat} \\ \text{K}\pi &= \text{Kbeam} \cdot \pi\text{scat} \end{aligned}$$

In addition to the above triggers a minimum bias "ITBT" triggers is used with the definition:

$$\text{ITBT} = \text{IT} \cdot \text{BT},$$

where BT is the logical OR of the BT logs 17-24, 28.

We have found that the first level trigger rate was too high for the image intensifier (IIT) normal operation. To reduce the IIT trigger rate, the correlation between the FP and BT elements is used. Multi-input coincidence units called "Matrix" are used to produce a "KKM" trigger for certain FP-BT combinations with the definition:

$$\text{KKM} = \text{KK} \cdot \text{M},$$

name	definition	what	prescale factor
Kbeam	$IT \cdot \overline{IC}$	incident K^-	8×10^5
πbeam	$IT \cdot IC$	incident π^-	2×10^6
Kscat	$FP \cdot BP \cdot FC0 \cdot \overline{(FC \cdot BC)}$	outgoing K^+	∞
πscat	$FP \cdot BP \cdot (FC \cdot BC)$	outgoing π^+	∞
KK	Kbeam $\cdot$ Kscat	(K^-,K^+)	1×10^0
KKM	KK $\cdot$ Matrix	IIT trigger	1×10^0
πK	πbeam $\cdot$ Kscat	(π^-,K^+)	4×10^1
Kπ	Kbeam $\cdot$ πscat	(K^-,π^+)	1×10^4
ITBT	$IT \cdot BT$	minimum bias trigger	2×10^3

Table 2.4: First level trigger definitions and their prescale factors.

where M stands for Matrix. A Matrix unit has 12×2 inputs which can be thought of as columns and rows of a matrix. The unit can be programmed to produce a trigger for certain pairs of input signals. The momentum of the kaons from the (K^-,K^+) reaction is, on average, lower than that of the protons from the (K^-,p) reaction (main background source). Tuning the matrix to accept the range of momentum corresponding to the (K^-,K^+) reaction allows partial rejection of the proton background. The summary of the first level triggers used is given in Table 2.4 along with their prescale factors in the trigger mix.

2.8.2 Second level trigger

Most of the first level KK triggers are elastic and inelastic (K^-,p) events due to the much higher cross section of the process. The second level trigger uses position information from the FD3 drift chamber and BT time-of-flight wall along with IT-BT time-of-flight to suppress by a factor of about 20 (K^-,p) events that contaminate KK triggers. The principle of the second level trigger operation can be described in the following way:

- The position of the particle trajectory at FD3 and BT roughly determine its momentum and path length.
- Particles with different masses will have different time-of-flight. Therefore making an appropriate time-of-flight cut, dependent on the position of the trajectory at FD3 and BT, will result in preferential selection of particles with the desired mass.

In E885 the second level trigger has to be fast, because it is used to gate the second stage of the IIT. Software decision for the second level trigger used in the previous experiments on D6 line took $\sim$150 μs. That is too long for E885 because the IIT

image would fade too much. Therefore hardware trigger is implemented with the the LCS 2372 Memory Lookup Unit (MLU) and LCS 4516 Logic Unit used to make the decision. The FD3 y-position is provided as a 16 bit word (FD3 bits). Each bit represents the logical OR of a group of 6 wires, 3 from each of the two y-planes. Each group of 6 wires covers 4.445 cm. The location of the BT log which fired determines the BT y-position. Thus, the whole acceptance is broken into several small regions, small enough to impose an efficient time-of-flight cut for each region to select kaon and suppress protons.

The IT-BT time-of-flight is measured by a LeCroy Fast Encoding and Readout TDC (FERET) system with 500 ps resolution/ch, which consisted of three LeCroy 4303 16-input Time-To-Charge Converters, three LeCroy 4300B 16-input Fast Encoding & Readout Charge ADC (FERA) and single LeCroy 4301 Fast Encoding & Readout Driver module. The FERA output is a sequence of 16-bit words, one header word per FERA module and one word per BT log hit. The header word has the bits indicating from which FERA module the following data words will come. The data word has information on the time-of-flight and the FERA channel number. The latter can be related to the BT log number if the FERA station number, from which the data word came, is known. The FERA output needs to be restructured to be suitable for its use as a 16-bit address for the MLU input. After appropriate bit manipulations, IT-BT time-of-flight (10 bits) and the BT log number (6 bits) are encoded into a 16-bit word to be used as the MLU input. The MLU is essentially a programmable memory unit with the capacity of 65536 16-bit words. The combinations of BT log – IT-BT time-of-flight are used in sequence to address 16-bit words in the MLU which represent the allowed FD3 bits. The MLU is programmed to suppress the protons and pions and let the kaons through. The MLU output changes as the MLU input changes and the output serves as one of the two inputs to the Logic Unit, the other being the actual FD3 bits. If the logical AND of any of the MLU output words, which are the allowed FD3 patterns, and the actual FD3 bits is not zero then the event is accepted.

2.9 Data Acquisition System

A diagram of E885 Data Acquisition system (DAQ) is shown in Figure 2.6. Two Fast Intelligent Controllers FIC 8232 (FIC1) and FIC 8231 (FIC2) are used in a single VME crate. Four Fastbus crates with the front end electronics are read out through the Fastbus LCS 1821 Segment Manager/Interface (SM/I) – VME LCS 1190 Dual Port Memory (DPM) uni-directional link. Fastbus initialization is done by FIC1 through CAMAC interface modules LCS 2891A, that talk directly to the Fastbus SM/I's. The SM/I modules write Fastbus data to DPM. The IIT digitized image is written to DPM by the specially designed 2 "Big Boards", one Board for each IIT system. Before writing data to DPM, the "Big Boards" suppress the digitized image pixels that are below the adjustable threshold value and compress data. Also,

some information is read from the CAMAC crates, such as the event and IIT trigger patterns, scalers, FD3 bit pattern. As the event readout is complete, FIC1 releases the trigger and DAQ is ready to accept a new event. At this moment data read out from Fastbus and IIT are located in DPM and CAMAC data are located in FIC1 memory. Then FIC1 initiates a Direct Memory Access (DMA) write to FIC2 memory. When the write is completed the DPM becomes available for new event readout and FIC1 sends an "OK to read out" signal to the corresponding Fastbus crates and IIT "Big Boards". Thus deadtime is reduced by allowing a second event to be captured in the front-end modules while the preceding event is still being transfered from DPM's (subsequent triggers, if any, would then be hold off until this event has moved entirely to DPM's and FIC memory). FIC2 formats events in its memory and writes them to an 8 mm tape. A fraction of the events is sent to a μVAX II through a BIT3 VME-Qbus bus interconnect for online monitoring and analysis.

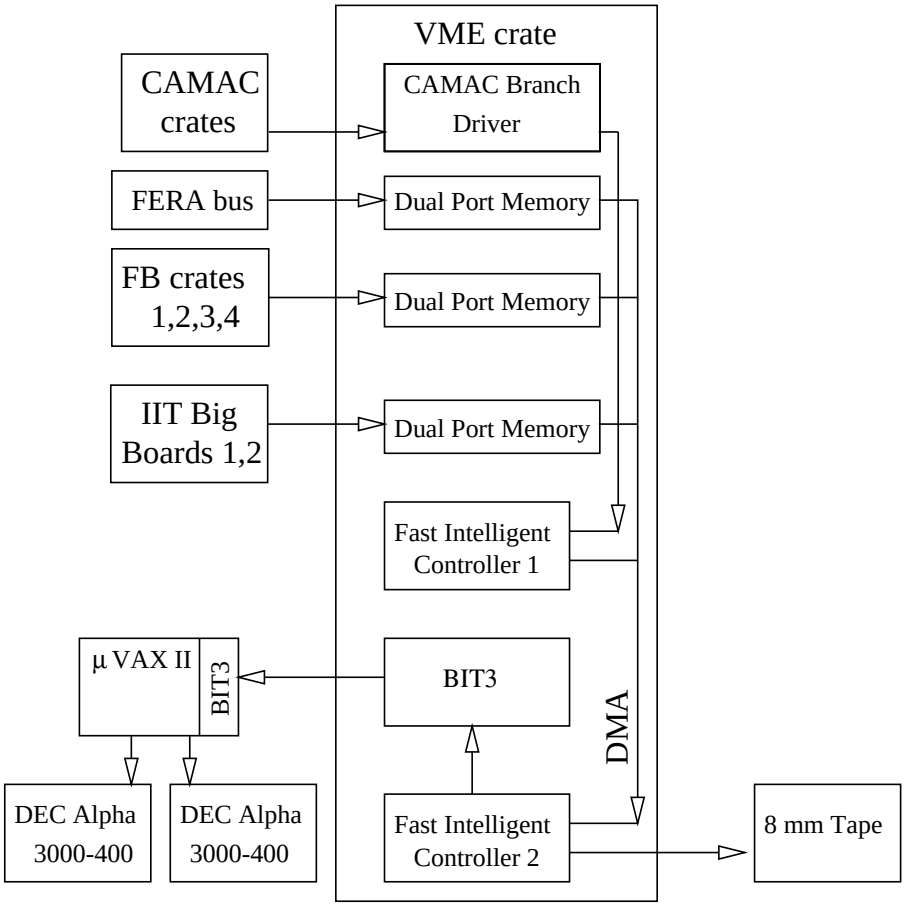

Figure 2.6: A diagram of the Data Acquisition System (DAQ) used in E885. ADCs and TDCs are read out from 4 Fastbus crates by means of an asynchronous high-speed write to the Dual Port Memory (DPM) modules in the VME crate. The IIT information is written to DPM by the specially designed "Big Boards" 1 and 2. CAMAC crates with the event and IIT trigger patterns, scalers and FD3 bit pattern information are read out by the Fast intelligent Controller 1 (FIC1) through the CAMAC Branch Driver.

Chapter 3

Event Reconstruction

The S=–2 producing reaction used in E885 is $^{12}C(K^-, K^+)X$. The dominant mechanism for producing an S=–2 system occurs as a K^- strikes a target proton inside the carbon nucleus and a K^+ and Ξ^- are produced: $K^- + p \rightarrow K^+ + \Xi^-$. This depiction of the reaction is called "elementary", because it shows only the particle transformation and does not reflect the multi-body nature of the collision. The incident K^- and outgoing K^+ are directly detected and momentum analyzed.

The goal of event reconstruction is the identification and measurement of energy-momentum of all or some particles participating in a reaction. An array of detectors (see Figure 2.1) is used for the purpose, which can be divided into in-beam and out-of-beam ones.

The in-beam detectors measure the primary (beam) particle and secondary (scattered) particles. The out-of-beam detectors (neutron and scintillating fiber detectors) are used to observe the properties of the created S=–2 systems. The in-beam detectors can be further divided into two groups: the beam line with MP, MT, IT, IC, ID1-3 can be thought of as the primary particle spectrometer, and FD1-3, FC0, FC, BD1-2 and BT as the secondary particle spectrometer.

This chapter describes how tracking and particle identification are done. The issue of background is discussed briefly and two lists of cuts used for hypernuclear production analysis are presented.

3.1 Analysis Software

The initial stage of data analysis is performed using IDA – Interactive Data Analysis package. IDA provides the data, memory and histogram management framework, on which so-called analyzers are built. An analyzer is a set of routines that serve a well-defined purpose in the analysis, for example track finding in the back region of the spectrometer. Apart from providing the end result, analyzers usually provide additional information, such as the detector subsystem performance.

IDA provides a convenient way to manipulate data through subroutine calls. The user is not concerned with how data is stored and retrieved from memory. The so-

called SYNOP variables are the IDA data structures that can be defined, written to memory and retrieved from memory. A typical IDA control flow is the following:

- An event is read from a disk or tape to a buffer in memory.
- Unpacking is done using the UNPACK analyzer. Physical addresses, like FB crate, slot and channel numbers are mapped to corresponding SYNOP variables. The mapping is done using a map supplied by the user.
- Event analysis is done by calling various analyzers.
- Histograms are filled.
- (Data Reduction only) Selected events are sent to one or more streams.

IDA provides the additional functionality of writing events that satisfy the user-defined tests to one or more streams. That is a useful feature for doing data reduction.

The result of running IDA is usually an HBOOK histogram file. On a more advanced stage of the analysis, when event reconstruction routines are stable and cut studies are being done, events are dumped into a user-defined ntuple. The author has written an ntuple analyzer that parses a text file with instructions on how to map SYNOP variables to ntuple variables and creates and fills a column-wise ntuple. The use of ntuples greatly facilitates the analysis.

3.2 In-beam tracking

The first stage of tracking is finding trajectory segments or positions in the following four regions, where only low fringe magnetic field exists:

- Mass slit region, located just downstream of the first mass list. The primary particle position is measured by scintillator hodoscopes MP and MT.
- Incident beam region, located between the last beam line magnet and the target. The primary particle trajectory is measured by drift chambers ID1-3.
- Forward spectrometer region, located between the target and the spectrometer magnet. The secondary particle trajectory, prior to its entering the magnet, is measured by drift chambers FD0-2.
- Back spectrometer region, located between the spectrometer magnet and BT. The secondary particle trajectory, after being bent by the magnet, is measured by drift chambers BD1-2.

The 48D48 spectrometer fringe magnetic field is neglected and trajectories in drift chambers are found by fitting hits to a straight line. Generally, there are several hit combinations and therefore several track candidates in each region and they are sorted by χ^2. FD3 is located inside the spectrometer magnetic field, where the secondary particle's track is bending, and cannot be used on this stage.

The second stage of tracking consists of connecting the trajectories found in the first stage (mass slit and incident beam regions for primary and forward and back regions for secondary particles) and finding the momenta of the primary and secondary particles. The task can be briefly summarized as finding a magnitude of the particle's momentum that would provide a trajectory connecting the two segments separated by a region with known magnetic field with the least χ^2. The solution is found through iterative fits, where the iteration parameter is the momentum of the particle; the primary particle track measurements in the incident beam and in the mass slit regions are combined to find the primary momentum and the secondary particle track measurements in the forward and back spectrometer regions are combined to find the secondary momentum. The trajectory measurement by FD3 is used only in the second stage.

As the result of the tracking, momenta of both primary and secondary particles, $\vec{p}_{prim}$ and $\vec{p}_{sec}$ are found.

3.3 Particle identification

Particle identification is designed to distinguish pions from kaons in the incident beam and kaons from pions and protons in the secondary beam. It is done by measurement of pulse height in Cherenkov detector(s), particle momentum, time-of-flight and flight path length. IC is used to identify the primary particle and FC, FC0 and BC are used to identify the secondary particle. Particle identification initially is done on the trigger level and is further refined in offline analysis.

On the trigger level, firing of IC (FC) qualifies the primary (secondary) particle as a pion. Since the surviving secondary particles are mostly protons, FC0 is used to distinguish between kaons and protons. Firing of FC0 is required when selecting secondary kaons in order to suppress proton knockout reactions. The second level trigger uses the secondary particle's time-of-flight and trajectory measurements at FD3 and BT to reduce proton knockout background by an order of magnitude.

Software cuts made during offline analysis are of similar nature. The IC and FC signals were corrected for 60 Hz noise and tighter cuts on the amplitude of the signal in both IC and FC allowed further suppression of background resulting from misidentification. Cuts were placed on primary particle's path-length-corrected time-of-flight and the secondary particle's mass.

The primary particle's momentum and path length are found from the position of the MP hodoscope element that is hit and particle's trajectory in ID1-3. The time-of-flight is measured between MT and IT. The cut is made on the path length-corrected

time-of-flight, defined as $T = T_{IT} - T_{MT} + \Delta L/c$, where $T_{IT} - T_{MT}$ is the time-of-flight between IT and MT, ΔL is the deviation of the particle's flight path length from that of the central ray length, and c is the speed of light. The beam line particles occupy a small volume in the phase space and the path length correction has little effect. So effectively, the cut on path length-corrected time-of-flight is essentially a cut on the particle's time-of-flight.

The secondary particle's momentum and path length are found from trajectories in FD0-3 and BD1-2. The time-of-flight is measured between IT and BT. The cut is made on the secondary mass, reconstructed from the measured time-of-flight, momentum and path length. The path length and momentum of the secondary particle vary a lot and a simple time-of-flight cut would not suffice. Figure 3.1 show the raw secondary mass distribution.

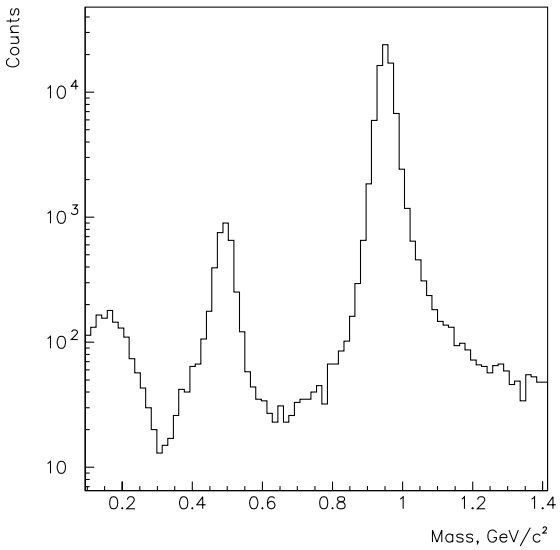

Figure 3.1: Secondary mass distribution for a subset of raw data. More than 90% of the raw data are (K^-,p) events.

3.4 Neutron Detection

The neutron detector arrays provide high detection efficiency [38] and high timing resolution in a wide range of neutron energies. A neutron is detected through its elastic and inelastic interaction in plastic scintillator (n-p scattering, n-^{12}C interaction). The two photomultipliers, viewing the log from the opposite ends provide the timing and amplitude of the signal from the neutron interaction: A_1, T_1 and A_2, T_2, where

the index denotes tubes 1 and 2 and A and T stand for amplitude and timing respectively. Assuming constant speed of the signal propagation in the scintillator and exponential attenuation (assumptions which are well confirmed and generally used for scintillator detectors), the following information can be found:

- Timing of the interaction $= T' + (T_1 + T_2)/2$,
- Coordinate of the interaction along the log $= \frac{c}{2}\,(T'' + T_1 - T_2)$,
- Energy deposition $= \sqrt{A_1 A_2}$.

c is the signal propagation speed in the scintillator log and was found in special calibration measurements. T' is fixed by measuring time-of-flight of prompt photons, which are emitted from the target as a result of nuclear de-excitation. The negligible delay between the moment of the beam particle impact on the target and emission of a prompt photon allows the calculation of the time-of-flight of the photon between the target and the interaction point in the neutron detector. Then the difference between the expected and measured time-of-flight will be equal to T'. T'' is determined from cosmic ray calibration runs, where cosmic tracks going through the center of the log are selected by trigger counters. The timing was monitored during the run and any small shifts were corrected. This resulted in keeping the systematic timing errors to less than 100 ps.

There are two additional calibration coefficients which are absorbed into T and A in the formulas above. They are coefficients that are used to convert digitized timing (TDC channel) and amplitude (ADC channel) information to ns and MeV.

The TDC channel to timing conversion coefficient should be, according to the manufacturer, within 1% of the nominal value. This was confirmed. But even 1% variation will cause a considerable time-of-flight error for slow neutrons. For that reason the nominal value was not used. All TDC channels were calibrated using delayed trigger and that suppressed the potential error by an order of magnitude.

The ADC channel to amplitude conversion coefficients were inferred from the cosmic ray run, where the energy deposition in the logs was known. The ADC calibration done before and after the run showed no changes in the gain and that justified the use of the calibration done after the run for analysis of the data.

To summarize, the neutron detectors provided the energy deposition and the position and the time of an interaction. The energy of the neutron is determined from its time-of-flight and the distance between the target and neutron interaction point in the neutron detector.

The efficiency of detecting a neutron originating in the target and with direction of flight uniformly distributed in space is shown in Figure 3.2 as a function of the inverse of the neutron velocity in units of beta inverse for 1 MeV threshold. It was calculated with the DEMONS [41] code. The neutron detection efficiency is sensitive to the value of the amplitude threshold. The hardware amplitude threshold, determined by the discriminator threshold settings and the photomultiplier gain, was set to about

0.5 MeV. To remove the uncontrollable influence of the hardware threshold, a uniform software threshold was applied. A value of 1 MeV was chosen, since it is safely above the hardware threshold and its effect on the neutron detection efficiency could be calculated in Monte Carlo simulation. The software threshold is applied to the earliest log (the one that determines the neutron energy) and a cluster with the earliest log falling below the threshold is discarded. The systematic shift in the measured time-of-flight due to picking the earliest log which only appeared earliest due to timing fluctuations is ignored in Monte Carlo simulation because it should not be significant due to having only 20% clusters with more than one element.

Another important characteristic of the neutron detector is its neutron energy resolution. The expected width of a mono-energetic neutron peak was calculated in Monte Carlo (calibrated by the observed timing resolution for cosmic rays) and shown in Figure 3.3. Although the finite width (<0.1 MeV [39]) of the (Ξ^-,^{12} C) atomic state causes variation of the neutron energy, its contribution can be neglected, because the neutron energy resolution is considerably worse ($\approx$ 1 MeV). The factors contributing to the error are:

- uncertainty of the flight path length resulting from the finite target and log sizes and timing resolution,
- uncertainty of time-of-flight due to finite timing resolution.
- uncertainty in stopping time of the Ξ^-.

The finite timing resolution contributes to the uncertainty in the flight path length because the coordinate along the log is calculated from the time difference. The timing resolution was measured [40] using both cosmic rays and laser flasher and is parameterized as $\sigma = 0.41/\sqrt{E}$ ns, where E is the energy deposition in MeV. The average Ξ^- stopping time was calculated in Monte Carlo and was found to be 0.14 ns.

Only the first (earliest) interaction of the neutron is of interest, since it determines the neutron energy through time-of-flight. Sometimes, however, a neutron-nucleus interaction will result in photon emission and firing of other logs in proximity to the primary interaction. In order to reduce such a background, a clusterization is done. All adjacent logs that fired are associated with a single cluster and the log where the primary interaction occured (earliest log) is determined as the log with the smallest time-of-flight.

Most neutron clusters will have only one element - 80%, and only 20% will have two or more. Therefore the reduction of the neutron background via clusterization is about 20%.

The clusterization also reduces background from charged particles. For example, a stopped π^- will be sometimes absorbed by a nucleus and cause its disintegration and emission of particles. The clusterization will correctly associate signals in neighboring logs as belonging to the charged cluster and prevent a potential misidentification of them as neutron events.

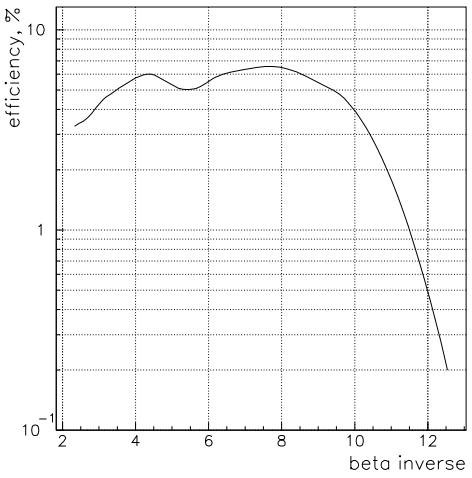

Figure 3.2: Neutron detection efficiency for 1 MeV threshold as a function of the initial neutron beta inverse. Neutrons are emitted isotropically at the target location.

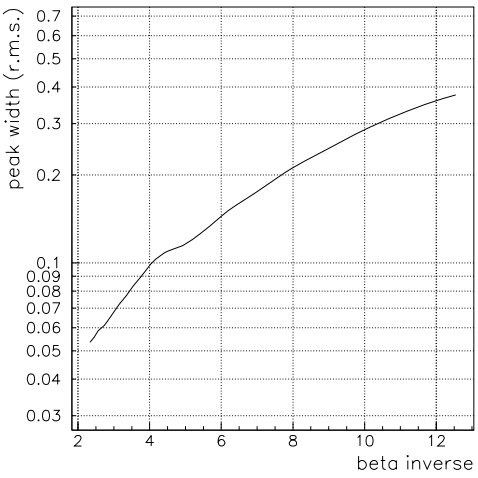

Figure 3.3: Neutron detector resolution. Shown is the width (r.m.s.) of a mono-energetic neutron peak in units of beta inverse as a function of the neutron velocity in units of beta inverse. The error is determined by the flight path length and time-of-flight uncertainties.

3.5 Useful kinematic quantities: Missing Mass, Excitation Energy and Binding Energy

A very important kinematic quantity is the missing mass, which is defined as the invariant mass of the object created but not detected in a reaction. Here the object may consist of several particles. If the object consists of a single particle, then the missing mass is equal to the particle's mass. Applying the definition to the case of a spectrometer-type experiment

$$\mathrm{M} \equiv \sqrt{(\mathrm{E_p} + \mathrm{M_T} - \mathrm{E_s})^2 - (\mathbf{p}_\mathrm{p} - \mathbf{p}_\mathrm{s})^2},$$

where $\mathrm{E_p}$ and $\mathbf{p}_p$ are the primary particle's energy and momentum, $\mathrm{M_T}$ is the mass of the target nucleus, $\mathrm{E_s}$ and $\mathbf{p}_s$ are the secondary particle's energy and momentum. Since this is an invariant quantity, it can be easily seen that the physical meaning of the missing mass is the energy in the object's rest frame. Therefore, discrete states would appear as peaks on a missing mass plot and could be identified, provided resolution and background allow it.

Excitation energy of an object is defined as a difference between the missing mass of the object and some offset energy: $\mathrm{E_{exc}} = \mathrm{M} - \mathrm{E_0}$, where $\mathrm{E_{exc}}$, M and $\mathrm{E_0}$ are ex-

citation energy, missing mass and offset respectively. The offset can be chosen as a particle disintegration threshold, so that negative excitation energies would correspond to bound states. But it can also be chosen as the ground state energy. Even though missing mass and excitation energy are very simply related, the presentation of excitation energy distribution has an advantage of explicit display of a meaningful quantity, as seen from the second example below.

- (K^-,K^+) reaction on hydrogen: $K^- + p \to K^+ + \Xi^-$. Both kaons are detected, the target proton's state is known. The Ξ^- is not detected, but its momentum and energy are found from the energy-momentum conservation law. The missing mass distribution will exhibit a peak with the width determined by the experimental resolution and can be used to study resolution. The peak centroid should be at the Ξ^- mass, 1321 MeV/c^2. The latter fact is used for missing mass scale calibration.

- (K^-,K^+) reaction on carbon: $K^- + {}^{12}C \to K^+ + X$. The baryon content of X is ${}^{11}B + \Xi^-$. Similarly to the previous case, the energy and momentum of X are known from energy-momentum conservation law. Most often the X is a cascade plus nuclear core and missing mass distribution is continuous. But if the X is a Ξ hypernucleus then missing mass is equal to the mass of the created hypernuclear state. It is convenient to choose the sum of the ${}^{11}B$ and Ξ^- masses as the zero of excitation energy: $E_{exc} = M - (M_{^{11}B} + M_{\Xi^-})$. Then bound Ξ hypernuclear states will have negative excitation energy equal to the binding energy of the Ξ^-: B_Ξ.

The binding energy of a particle(s) in a nucleus is defined as the difference between the sum of the nucleus and particle(s) masses and the mass of the particle(s)-nucleus state. In application to Ξ and double-Λ hypernuclei:

$$B_\Xi = M_{^A_Z} + M_{\Xi^-} - M_{^{A+1}_{\ \ \Xi}(Z-1)},$$

$$B_{\Lambda\Lambda} = M_{^A_Z} + 2M_\Lambda - M_{^{A+2}_{\Lambda\Lambda}Z}.$$

A new notion of Λ-Λ binding energy is introduced for double-Λ hypernuclei, describing Λ-Λ interaction: the Λ-Λ binding energy is defined as the change in the total binding energy of the two Λ's due to the Λ-Λ interaction:

$$\Delta B_{\Lambda\Lambda} = B_{\Lambda\Lambda} - 2\,B_\Lambda$$

In the formulas above, A and Z are the number of baryons (hyperons + nucleons) and the charge respectively.

3.6 Background

To reduce background, in addition to the above particle identification cuts, a combination of goodness-of-fit, vertex and multiplicity cuts are applied. Figure 3.4 shows

the vertex distribution in z for the raw data. As seen from Figure 3.1, (K^-,p) reaction is the main background constituting more than 95% of the raw data.

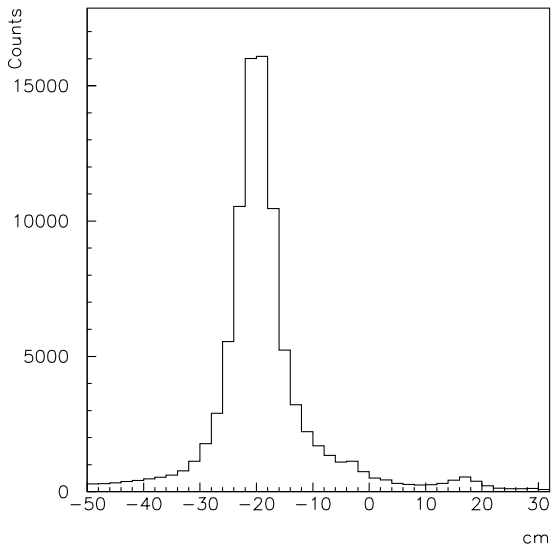

Figure 3.4: Vertex distribution in z for a subset of raw data. σ_{peak}=3.3 cm. The vertex resolution, obtained by subtracting the contribution from the finite target thickness, is σ=3 cm.

The tightness of the cuts is determined by how critical the purity of the data sample is. In this analysis, two set of cuts were used: a very tight one for the direct Ξ hypernuclear production signal and a loose one for the search for double-Λ hypernuclei. A brief summary of the cuts is given in Section 3.7.

3.7 Cuts

The goodness-of-fit, shown in Figure 3.5, is defined as

$$(\sum_{i=1}^{5} \frac{(x_{measured} - x_{fit})^2}{\sigma_{ix}^2} + \sum_{i=1}^{5} \frac{(y_{measured} - y_{fit})^2}{\sigma_{iy}^2})/5,$$

where summation is done over five drift chambers (FD1-3 and BD1-2) measurements in x and y, and σ_{ix} and σ_{iy} are intrinsic chamber resolutions for i-th drift chamber in x and y. The denominator is the number of degrees of freedom. The number of degrees of freedom is calculated as number of measurements (10 = 5 chambers$\times$ 2 projections) minus number of parameters (5 = 3 momentum projections + x and y coordinates of the trajectory at $z = 0$). Due to the effects of multiple scattering,

fringe magnetic field and non-perfect chamber alignment, the goodness-of-fit is on average considerably greater than unity, which would have been expected without those effects.

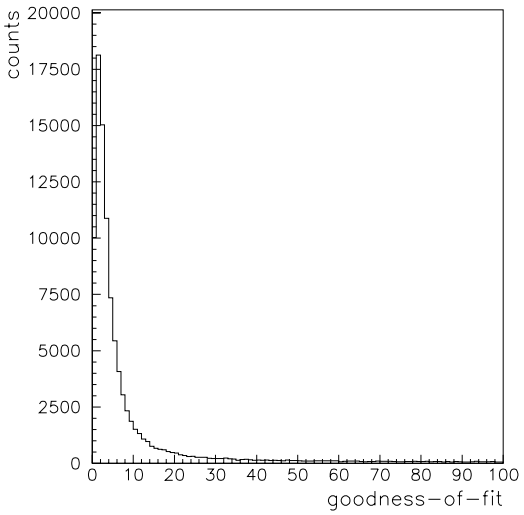

Figure 3.5: Goodness-of-fit distribution for a subset of raw data.

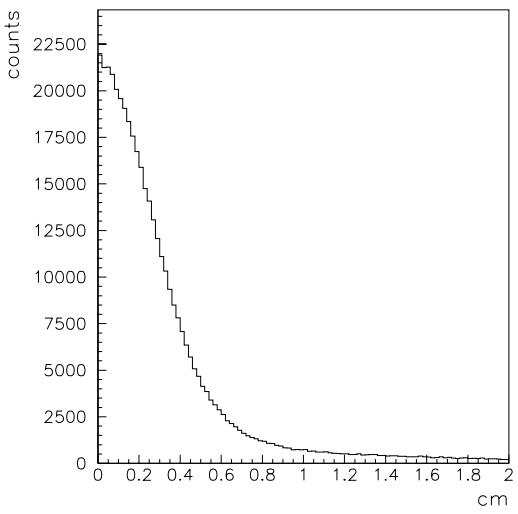

Figure 3.6: Distance of closest approach distribution for a subset of raw data.

The summary of the cuts is presented in the following two subsections. The particular values chosen for the cuts on a particular parameter were obtained by either visual evaluation of the distribution of the parameter and selecting cuts that would eliminate the tails of the distribution and still preserve most of the data or evaluating the influence of the cuts on the background level in the region of the missing mass where no or little signal should be expected.

3.7.1 Cuts used in direct Ξ and double-Λ hypernuclear production analysis

- 3σ cut on the reconstructed secondary particle's mass: less than 0.53 GeV/c^2 and greater than 0.45 GeV/c^2.
- 60 Hz-corrected IC and FC Cherenkov amplitudes less than 350 ADC channels.
- Flight-path-length-corrected time of flight in the beam line between MT and IT is consistent with the beam particle being a kaon within a 1 ns window.
- Only one hit or two hits in adjacent elements in MP within a 5 ns window.
- Time of MP hit within a 2 ns window from the expected time.

- Events for which beam momentum reconstruction failed are rejected.
- Vertex cuts:
  - 3 σ vertex z-position cut around the centroid of the vertex z-position distribution, dependent on the scattering angle θ. The θ-dependence reflects the vertex resolution dependence on θ. σ changes from 1.9 cm for large angles to 4 cm for small angles ($\theta < 3^\circ$).
  - Vertex x-position less than 5 cm from the target center: less than 5 cm and greater than -5 cm.
  - Vertex y-position less than 0.5 cm from the target center: 0.5 cm and greater than -0.5 cm.
  - Distance of closest approach, defined as the distance between the primary and secondary tracks, less than 0.5 cm.
- Distance between the BD track projected onto BT wall and BT hit less than 10 cm both in x and y.
- All four FD3 planes must have a hit.
- Secondary particle goodness-of-fit less than 50.
- ID track projected onto IT must be consistent with the IT element being hit.
- ID track χ^2 less than 5.

3.7.2 Cuts used in double-Λ hypernuclear formation via Ξ^- capture on carbon analysis

- Mass of the secondary particle less than 0.56 GeV/c^2 and greater than 0.34 GeV/c^2.
- Vertex z-position less than 10 cm from the target center: less than -10 cm and greater than -30 cm.
- Secondary particle goodness-of-fit less than 50.
- Missing mass less than 11.637 GeV/c^2. This cut is made in order to optimize the neutron spectrum signal-to-noise ratio and is discussed in Chapter 5.

The secondary mass cut is asymmetric relative to its centroid because both experimental and simulated secondary mass distribution exhibit a tail on the left which comes from secondary kaon decays in the back region of the spectrometer and it was found that using those events in the tail would improve the signal-to-noise ratio.

Chapter 4

Monte Carlo detector simulation

Monte Carlo simulation is used for

- Acceptance studies for various reactions,
- Ξ^- stopping rate calculation.

The primary focus of the acceptance studies was on the Ξ^- and double-Λ production detection. The Ξ^- stopping probability is used to calculate the yield of the double-Λ hypernuclei as a function of the missing mass. The efficiency of neutron detection was studied separately in the DEMONS [41] simulation package. Our Japanese collaborators also investigated the acceptance for different decay modes of the H-dibaryon.

The E885 detector simulation was done in GEANT 3.21. The detector geometry, as described for GEANT, is shown in Figure 4.1. For historical reasons tracking of the produced K^+ in the spectrometer was done by custom written code. The trajectory of the K^+ was found by numerically solving the equation of motion in the known magnetic field of the spectrometer using the Runge-Kutta method. The decay of the K^+ was simulated as well. To make the simulation more realistic, the empirical detector inefficiencies were incorporated into simulation. The K^+ was accepted if it (or its charged decay products) hit all the detectors in the forward and back regions of the spectrometer. In case of the K^+ decay, the same cuts used in event reconstruction were imposed, suppressing most decays and letting a small fraction of them through. To speed up the tracking, it was later replaced by the matrix formalism. In the new approach, the spectrometer phase space was divided into many smaller regions and linear optics approximation was used to find matrix solution for each region.

The flow of the simulation code can be described as follows:

- Free Ξ^- or direct hypernuclear production,
- Tracking the outgoing K^+,
- Ξ^- tracking or simulation of hypernuclear decay modes.

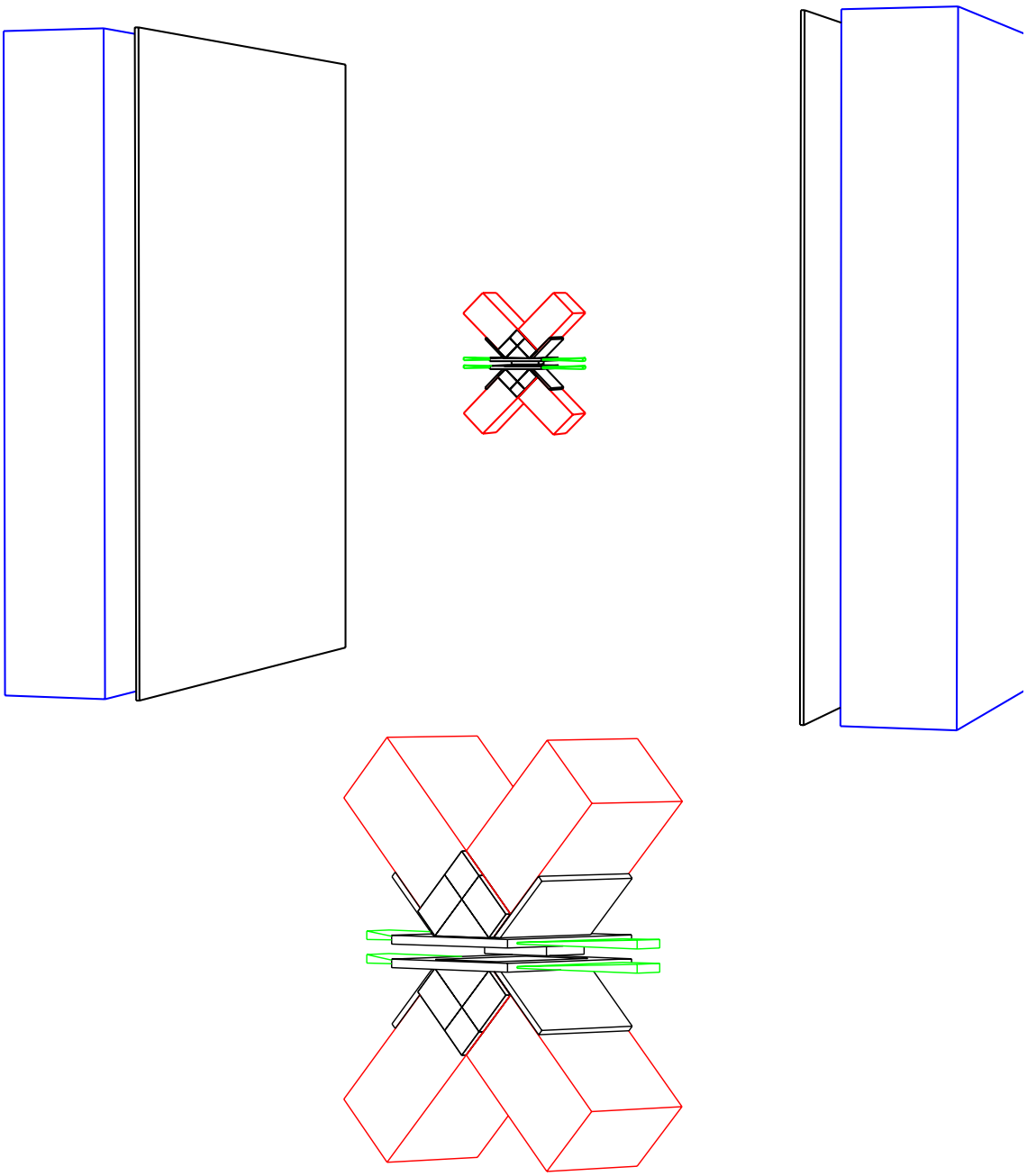

Figure 4.1: The region around the target drawn by GEANT. The upper picture shows scifi and neutron detectors. The lower pictures shows scifi detector only. The initial Ξ^- is generated and handed over to GEANT for tracking. The stop of a Ξ^- is intercepted and the user code controls what happens next. Scenarios include various decay modes of double-Λ hypernuclei or H-dibaryon.

The last part of the simulation is done only for accepted K^+'s and otherwise skipped.

The Ξ^- stopping rate, determined by the Monte Carlo, was multiplied by a factor of 0.8 to account for 20% Ξ^- escaping probability of stopped Ξ^-'s in carbon [42], which was measured in E224 experiment at KEK.

4.1 Ξ^- and hypernuclear production

The initial step of the Monte Carlo is the simulation of (K^-,K^+) reaction on carbon or hydrogen target with $p_{K^-} = 1.8$ GeV/c. Several outcomes are simulated, all of which can be divided into the following two categories: free Ξ^- or hypernuclear production. The hypernuclear production scenario includes Ξ^- or double-Λ creation and several possible decay modes.

The Ξ^- production on hydrogen and hypernuclear production are two-body reactions and the kinematics is simple. The Ξ^- production on carbon involves more than two bodies in the final state. The following simplification is made: the Ξ^- production on carbon is treated as Ξ^- production on hydrogen (that is, a proton) with the following modifications to account for the proton binding in the nucleus:

- The proton has initial momentum not equal to zero (Fermi motion),
- The energy of the proton is modified to conserve energy.

So the collision of the K^+ and the proton bound to the nuclear core is treated as a collision of particles in free space, with necessary modifications to conserve energy and the nuclear core is treated as a spectator. Effectively, the nucleus is treated as sum of two parts, the proton and the nuclear core, that do not interact during the collision and the proton initial momentum and energy fix the kinematics of the Ξ^- production. The momentum distribution of the protons inside the carbon nucleus was derived from the harmonic oscillator model [43]. The incoming K^- interacted with a $1s$ proton with probability 1/3 and with $1p$ proton with probability 2/3, in accordance with the number of protons populating $1s$ and $1p$ orbits. The square of the proton momentum-space wave function gave the probability density function for its momentum distribution.

If the initial proton momentum is p, then the energy of the proton is set to $E = M_p - B_p - p^2/2M_{core}$, where M_p, B_p and M_{core} are the proton mass, binding energy and the core mass. The last term is the recoil energy of the nuclear core. A non-relativistic form for the nuclear core kinetic energy is used because of the core low recoil velocity. The core mass is the mass of the carbon nucleus minus proton mass and plus the proton binding energy: $M_{core} = M_{^{12}C} - M_p + B_p$. The term B_p in the expression for the core mass is used to account for the excitation energy of the proton hole and a term with the same magnitude but the opposite sign is added to the energy of the struck proton in order to conserve energy. It is easily seen that

the total energy of the system (proton plus nuclear core) is equal to the mass of the carbon nucleus and the energy is conserved.

The only remaining issue is the angular distribution of the K^+. Based on the measurement of the (K^-,K^+) differential cross section, that suggest a flat angular distribution in the forward region [44, 31] in the (K^-,p) center of mass frame, the outgoing K^+ was generated uniformly over the accepted solid angle. Since the spectrometer acceptance was limited by $\theta < 14°$, this was justified: larger angles where the differential cross section changes appreciably were cut by the acceptance. Now that the target proton momentum inside the nucleus has been generated, fixing the angle of the K^+ fixes the kinematics of an event completely. The excitation energy spectra for the data and Monte Carlo (Figure 4.2) show good overall agreement. The deviation at about 100 MeV is due mostly to reactions on the remaining hydrogen in the diamond target.

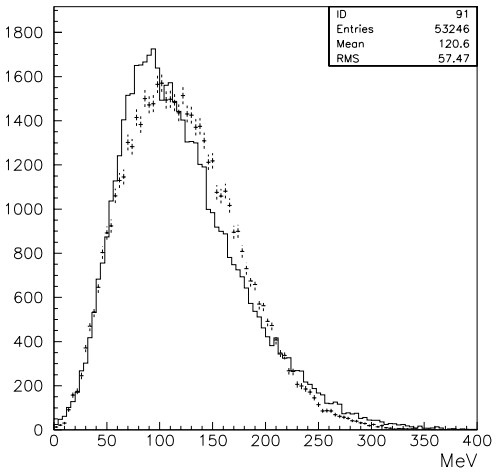

Figure 4.2: Excitation energy spectrum for E>0 region. Solid line - data, error bars - Monte Carlo.

The angular dependence for Ξ^- hypernuclear production was calculated based on DWIA derivation in [31]. The calculation used the spatial part of the wave functions of the reacting proton and created Ξ^-, which were solutions of the Schroedinger equation. The Woods-Saxon form of binding potential with nominal parameters was used:

$$U_B(r) = -V_{0B} f(r) + V_{LS\,B}(\frac{\hbar}{m_\pi c})(\mathbf{l}\cdot\mathbf{s})\frac{1}{r}\frac{df(r)}{dr} + U_{coulomb}(r),$$

$$f(r) = (1 + e^{\frac{r-R}{a}})^{-1},$$

$$R = r_0(A-1)^{1/3},$$

where subscript B indicates the baryon species.

Table 4.1 summarizes the values adopted for the parameters. The proton potential well depth is determined by matching the binding energies of $1s_{1/2}$ and $1p_{3/2}$ proton

r_0, fm	a, fm	$V_{0\Xi}$, MeV	$V_{LS\,\Xi}$, MeV	V_{0p}, MeV	V_{LSp}, MeV
1.1	0.65	20, 16	1	72.5	7

Table 4.1: The values adopted for Woods-Saxon potential

states ($\approx$ 34 MeV and 16 MeV respectively). Two values for Ξ^- potential well depth are tried: 20 MeV and 16 MeV. The choice is motivated by availability of DWIA calculation for the two values in [39]. The Schroedinger equation was solved numerically by iterating over energy and finding solutions that satisfied boundary conditions.

Although the angular distribution depends on what hypernuclear state is created and the depth of the potential, the difference was found to be small and the angular distribution for ground hypernuclear state creation for the potential depth of $V_{0\Xi} = 16$ MeV was used and it is shown in Figure 4.3.

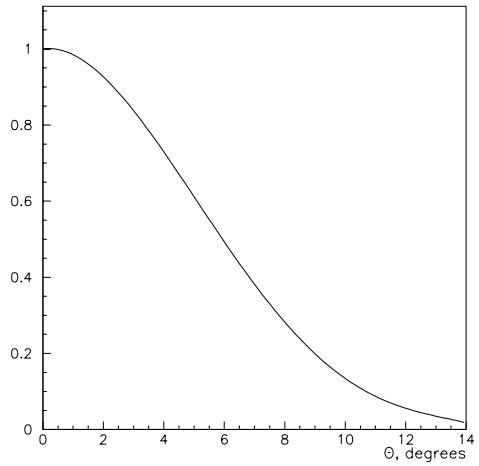

Figure 4.3: Angular dependence of direct Ξ hypernuclear production cross section in the laboratory frame (ground hypernuclear state, $V_{0\Xi} = 16$ MeV).

4.2 Acceptance for various reactions

The geometric spectrometer acceptance ($\approx$ 50 msr) for particles with p = 1.2 GeV/c is shown in Figure 4.4.

The overall acceptance for a particular reaction, as defined here, is the probability for an event to be accepted. The factors affecting this probability are geometric constraints (limited active area of the detectors), kaon decays and detector inefficiencies. Acceptance is calculated for the following 3 reactions:

$K^- + {}^{12}C \rightarrow {}^{12}_{\Xi}Be + K^+$ – direct Ξ hypernuclear production

$K^- + p \rightarrow \Xi^- + K^+$ – Ξ^- production on hydrogen

$K^- + {}^{12}C \rightarrow {}^{11}B + \Xi^- + K^+$ – Ξ^- production on carbon

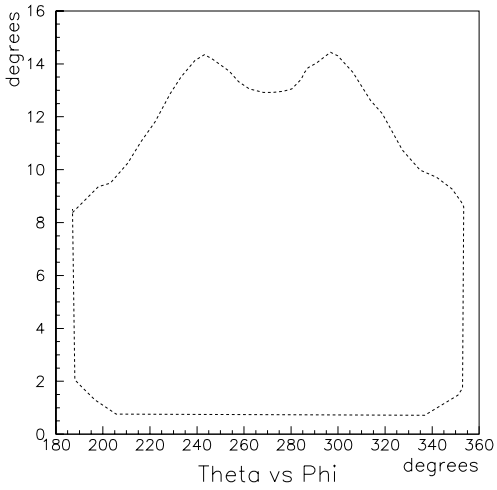

Figure 4.4: Geometric acceptance of the spectrometer for p = 1.2 GeV/c

The acceptance α, shown in Table 4.2, is an integral quantity, defined as the number of events that are accepted divided by the total number of events generated in the cone with $\theta_{K^+_{lab}} < 14°$. The sharp difference between the acceptance for free Ξ^- production and Ξ hypernuclear production is explained by both higher momentum of the secondary K^+ (lower FC0 inefficiency) and more forward-peaked angular distribution for hypernuclear production (larger geometric acceptance).

Reaction	Acceptance α, percent
Ξ^- production on hydrogen	8.1
Ξ^- production on carbon	5.3
Ξ hypernuclear production	14.3

Table 4.2: Acceptance for various reactions

4.2.1 Test of acceptance prediction

The accuracy of detector simulation can be tested through comparison of free Ξ^- production yields from reactions on carbon and hydrogen in CH_2 target. The ratio of the numbers of Ξ^- produced on carbon and hydrogen can be compared to the expected ratio, determined by the relative probabilities of interaction with carbon and hydrogen and acceptances.

The missing mass spectrum for CH_2 data (mass of the target nucleus used was the proton mass) is shown in Fig. 4.5. The peak corresponds to Ξ^- production on hydrogen and the rest of the events are Ξ^- production on carbon. The distribution was fitted with a template of missing mass spectrum from the diamond target data, treated as a proton for missing mass calculation, plus a Gaussian peak. The parameters of

the fit were the scale factor for the template and Gaussian peak width and size. From the fit, the number of events for Ξ^- production on hydrogen and carbon are N^H=480 and N^C=424 respectively. Their ratio can be compared to the expected:

$$\frac{N^H}{N^C} = \frac{\alpha^H \lambda^H}{\alpha^C \lambda^C Z_{eff}},$$

where α and λ are the acceptance and target thickness for a reaction and Z_{eff} = 2.57 [45] is an effective proton number for carbon. The values for α^H (acceptance for production on hydrogen) and α^C (acceptance for production on carbon) are given in Table 4.2 and the ratio of λ^H to λ^C is equal to two for CH_2 target. Substituting all the values gives the expected ratio of 1.19, which is in good agreement with the experimental value of 480/424 $\approx$ 1.13. This serves as a strong evidence in support of the Monte Carlo simulation validity, especially taking into account large difference in the acceptance for the two reactions.

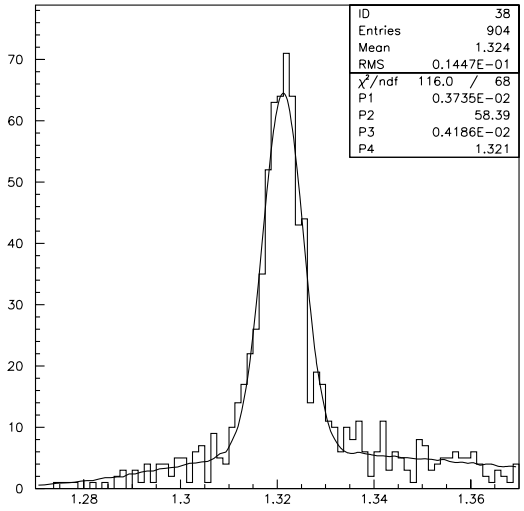

Figure 4.5: Missing Mass for CH_2 target, fitted with the template of missing mass for Ξ^- production on carbon and Gaussian peak. The ratio of events in the peak to the rest of the events can be used to test accuracy of Monte Carlo simulation prediction for detector acceptance. The experimentally observed ratio of 1.19 compared well with the expected value of 1.13.

Chapter 5

Double-Λ hypernuclear formation via Ξ^- capture on carbon

Capture of Ξ^- on nuclei has been used in searches of double-Λ hypernuclei in emulsion (see [27, 28, 29]). The evidence of the double-Λ-hypernuclear existence, however, is not firm. Only three events, interpreted as double-Λ hypernuclear formation with reconstructed kinematics, have been found.

The quantity that determines the available statistics is the number of Ξ^- stops. Due to the short lifetime of the Ξ^-, most of the produced Ξ^-'s will decay before coming to a stop. It is advantageous to use dense targets and higher beam intensities to maximize the yield. These requirements preclude previously used methods of visual detection of the event, because emulsion or scintillator material have relatively low density (low stopping power) and high intensity flux would make the analysis difficult or impossible.

In E885, Ξ^- capture on carbon was used to produce double-Λ hypernuclei. The availability of the high-intensity AGS D6 beam line and the use of high-density diamond target have allowed the accumulation of about 20 000 Ξ^- stops, orders of magnitude greater than previous experiments.

5.1 Detection of Double-Λ hypernuclear formation

A Ξ^- captured by a carbon nucleus forms an atom and starts cascading to lower orbits until it is converted via the reaction $\Xi^- + \mathrm{p} \rightarrow \Lambda + \Lambda$. The Ξ^- atomic calculations [46] indicate that the capture occurs mainly from $3d$ and $4f$ atomic orbits. The tendency towards the capture occuring mostly from the largest angular momentum state for a given principal quantum number ($L = N - 1$) can be understood by considering $\Delta L = 1$ transitions from a very high orbit ($N \gg 1$). A state with the property $L = N - 1$ can only go to a state with $L - 1 = N - 1 - 1$, i.e. a state with the same property.

Capture from $2p$ is strongly suppressed by loss of flux (and negligible from $1s$). According to Y. Akaishi *et al.* [47] the probability of capture from $2p$ orbit is 2.7%

(for $V_{0\,\Xi} = 16$ MeV). Atomic states are those, for which nuclear forces can be treated as perturbation to Coulomb force. Likewise, hypernuclear states are those that are determined by strong interaction. The size of the wave function changes dramatically on transition from atomic to hypernuclear states. Along with the name, labeling of the states changes from atomic quantum numbers to hypernuclear quantum numbers. So, $1p$ atomic and $1p$ hypernuclear states are very different. The excess energy (Q=28 MeV) must be carried away via particle emission or fragmentation. There are theoretical calculations that predict considerable branching ratio for the mode of decay in which a double-Λ hypernucleus is formed and a mono-energetic neutron is emitted:

- $(\Xi^-, {}^6\mathrm{Li})_{\mathrm{atom}} \rightarrow {}^{6}_{\Lambda\Lambda}\mathrm{He} + \mathrm{n}$ – branching ratio = 5%[46],
- ${}^{12}_{\Xi}\mathrm{Be} \rightarrow {}^{11}_{\Lambda\Lambda}\mathrm{Be} + \mathrm{n}$ – branching ratio = 20%[48].

A considerably lower value for the former reaction is given in ref. [39]. Note that the hypernuclei above are assumed to be in their ground state. Factors contributing to the higher branching ratio in the latter case are:

- no delay on atomic cascade during which the Ξ^- may decay,
- more bound state from which the conversion $\Xi^- + \mathrm{p} \rightarrow \Lambda + \Lambda$ happens and consequent smaller energy mismatch between the Ξ and double-Λ hypernuclei.

The double-Λ sticking probability for the case of light nuclei, like carbon, nitrogen and oxygen, was estimated to be about 10% from emulsion experiments [39] – higher than predicted by theory.

In E885, to detect the formation of double-Λ hypernuclei a search for mono-energetic neutrons from the process $(\Xi^-, {}^{12}\mathrm{C})_{\mathrm{atom}} \rightarrow {}^{12}_{\Lambda\Lambda}\mathrm{B}^* + \mathrm{n}$ is performed. The final hypernuclear state is generally excited (but particle stable) and there are several hypernuclear states that can be populated. Given sufficient signal-to-noise ratio, the peak(s) can be reliably identified and measured. The number of events in a peak and its location (neutron energy) can be used to find both the branching ratio for the decay through neutron emission (for a particular hypernuclear state) and the energy of the hypernuclear state. To conserve energy: $\mathrm{M}_{{}^{12}_{\Lambda\Lambda}\mathrm{B}^*} = \mathrm{M}_{(\Xi^-, {}^{12}\mathrm{C})_{\mathrm{atom}}} - \mathrm{M}_{\mathrm{n}} - \mathrm{T}_{\mathrm{n}}$, i.e. the energy of the hypernuclear state is the energy of the $(\Xi^-, {}^{12}\mathrm{C})$ atomic state minus mass and kinetic energy of the emitted neutron (neglecting recoil energy, which is much smaller than the resolution). From neutron energy spectra of double-Λ hypernuclei an important insight into the Λ-Λ interaction can be gained. The study of hypernuclear states by measuring neutron energy is similar to the study of hypernuclear states by measuring photon energy in hypernuclear γ-ray experiments. What particle can be detected is determined by whether the excited state is particle stable. In E885 the excited hypernuclear state (prior to its decay) is not particle stable so decay occurs through fragmentation or emission of particle(s) (via strong process) rather than emission of a photon (electromagnetic process). High neutron detection efficiency and high statistics are critical to be able to detect a peak on top of background.

5.2 Cut optimization and background subtraction

Most neutrons come from π^- capture and other background processes and give a smooth background spectrum (Figure 5.1). Since the Ξ^- stopping probability depends on the Ξ^- initial momentum, the effect of missing mass cut was studied in order to maximize the sensitivity. Missing mass was chosen as a kinematic quantity to cut on because it is in a close relationship with the Ξ^- momentum. Missing mass is the total energy of the (Ξ^- + nuclear core) system in its rest frame and lower values of missing mass correspond to slower Ξ^-'s. This system's rest frame is moving very slowly with respect to the laboratory frame, because the missing momentum is peaked at ≈ 600 MeV/c (for our acceptance) and the missing mass is ≈ 11.6 GeV/c^2 and $\beta \approx = 0.02$. Therefore slow Ξ^-'s in the (Ξ^- + nuclear core) rest frame (low missing mass) will be also slow in the laboratory frame.

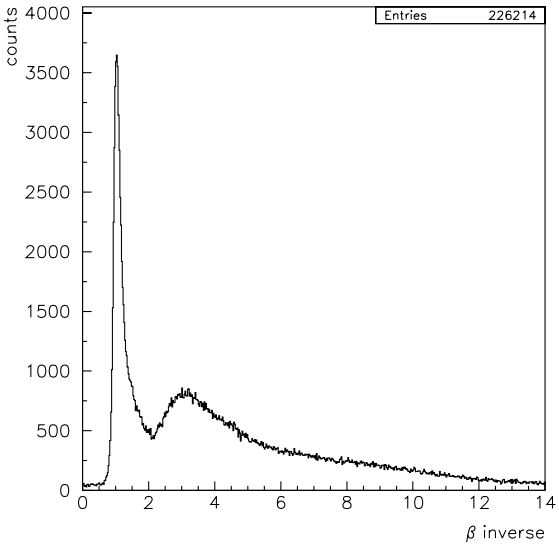

Figure 5.1: Neutron spectrum (data) as a function of β^{-1}. Prominent peak at $\beta^{-1} = 1$ comes from photons. The neutrons form a smooth spectrum with slower neutrons corresponding to higher values of β^{-1}.

The quantity that needs to be maximized is the "quality factor"

$$Q = \frac{S}{\sqrt{B}}.$$

S stands for signal and $\sqrt{B}$ represents the measure of background fluctuation. Any quantity proportional to signal or background can be used in the expression above. Signal is proportional to the number of events times Ξ^- stopping probability. Therefore number of events times stopping probability can be used for S. It was noticed that the shape of the neutron spectrum (excluding γ peak) did not depend on the missing mass cut value. That led to the use of the number of entries in the neutron

spectrum as B. So the expression for Q can be rewritten as

$$Q = \frac{\nu N}{\sqrt{n}},$$

where ν, N and n are Ξ^- stopping probability, number of events and number of entries in the neutron spectrum after missing mass cut, all functions of the missing mass cut value. Using the stopping rate as predicted by Monte Carlo simulation, it was found that the missing mass cut value of 11.637 GeV/c^2 maximizes Q and that value was used for the search of a mono-energetic neutron peak. For the events with the missing mass value less than 11.637 GeV/c^2, 31.7% of the Ξ^-'s would stop and form (Ξ^-,^{12} C) atoms.

The other cuts were loose, because neutron background level is already substantial and adding some background will cause a very little decrease in denominator of the figure of merit, square root of background magnitude. The signal, however is directly proportional to the number of events minus background events picked up as the result of loose cuts. The summary of the cuts is given below:

- Mass of the secondary particle greater than 0.34 GeV/c^2 and less than 0.56 GeV/c^2,
- Vertex z-coordinate within 10 cm of the target (greater than -30 cm and less than -10 cm),
- Momentum of the secondary particle (shown in Figure 5.2) less than 1.4 GeV/c.

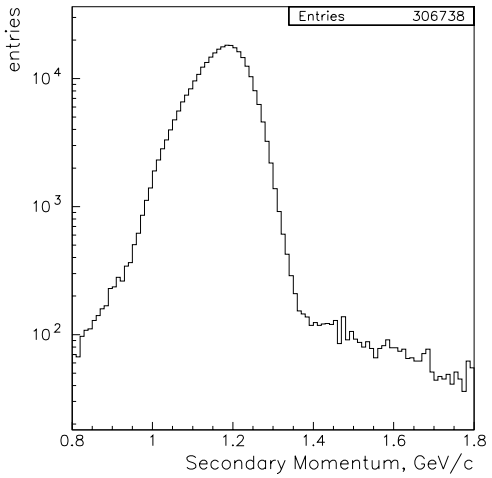

Figure 5.2: Secondary momentum distribution. Events in the high-momentum tail (>1.4 GeV/c) were excluded from analysis.

The background level from the non-(K^-,K^+) events (with the beam or/and secondary particle misidentified as kaons) in the missing mass spectrum was estimated by observing the low-energy tail of the missing mass distribution, shown in Figure 5.3. The

same cuts were used, except the last one (secondary momentum cut would eliminate the tail, naturally). The value of 100 background events per 10 MeV/c^2 wide bin of the missing mass distribution was obtained. Once the background level is estimated,

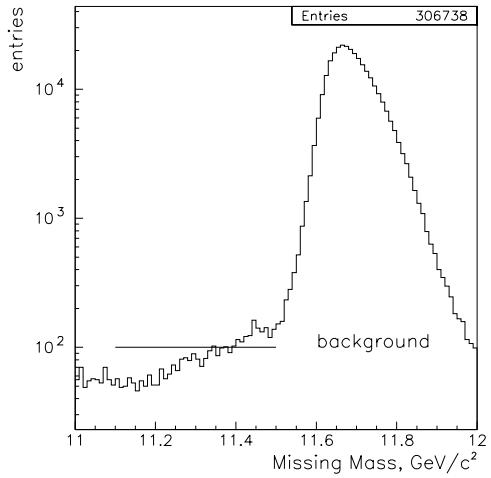

Figure 5.3: Missing mass distribution used for background level estimate. The magnitude of the low-energy tail provides the estimate for the background level. The horizontal line shows the value used.

the cut on the secondary momentum is applied to get rid of the non-physical low-energy tail (which disappears if more severe cuts are made) and the background is subtracted. The subtraction is done assuming flat background and the value of 100 is subtracted from every 10 MeV/c^2-wide bin of the missing mass spectrum. The background subtraction affects the number of Ξ^- stops and the value of the optimal missing mass cut. The result is shown in Figure 5.4. The numbers of total events, estimated background events and estimated Ξ^- stops are respectively 54150, 1370 and 16750 (background is 2.5% of total events).

There is also background, which is ignored in this analysis, from two-step ^{12}C$(K^-,K^+)Y^{(*)}Y^{(*)}X$ reactions, where $Y^{(*)}$ stands for a S=−1 (possibly excited) hyperon. This background is estimated using the total cross section for two-step processes calculated in Intranuclear Cascade Model [49]. Its contribution is estimated to be 1% or less in the region of missing mass less than 11.637 GeV/c^2.

5.3 Neutron emission branching ratio

Detection of a peak in the neutron spectrum would be a clear indication of double-Λ hypernuclear formation via $(\Xi^-,^{12}\mathrm{C})_{\mathrm{atom}} \rightarrow {}^{12}_{\Lambda\Lambda}\mathrm{B}^* + \mathrm{n}$. The energy and number of neutrons in the peak would determine the energy of the hypernuclear state and the branching ratio of its formation via neutron emission.

The expected neutron energy can be found from (the recoil energy of the double-Λ hypernucleus can be neglected)

$$\mathrm{T_n} = \mathrm{M}_{(\Xi^-,{}^{12}\mathrm{C})_{\mathrm{atom}}} - \mathrm{M}_{{}^{12}_{\Lambda\Lambda}\mathrm{B}^*} - \mathrm{M_n}.$$

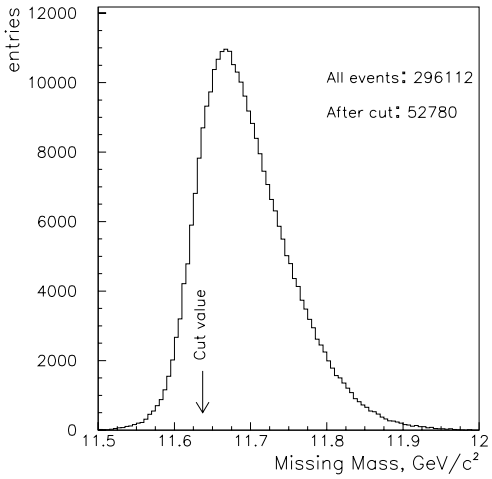

Figure 5.4: Missing mass (background subtracted) for $K^- + {}^{12}C \to K^+ + \Xi^- + X$. Events whose missing mass is less than the value indicated by an arrow passed the missing mass cut and have high Ξ^- stopping probability.

The binding energy of the ground state Λ in ${}^{11}_{\Lambda}B$ is 10.24 MeV [50]. The $(1s_\Lambda 1p_\Lambda)$ states are expected to be populated the most [46], with nuclear core in the ground state or at low excitation energy. Taking the binding energy of the Λ in the $1p$ state to be 10 MeV less than the binding energy of the Λ in the ground state and assuming ground state of the nuclear core, in the weak coupling limit:

$$M_{{}^{12}_{\Lambda\Lambda}B^*} = M_{{}^{10}B} + 2M_\Lambda - 10.24 \text{ MeV} - 0.24 \text{ MeV} - \Delta B_{\Lambda\Lambda}.$$

Neglecting the binding of the Ξ^- in atomic orbit, the kinetic energy of the neutron is $T_n = 11.3 \text{ MeV} + \Delta B_{\Lambda\Lambda}$. So the expected neutron energy is in the neighborhood of 11.3 MeV ($\beta^{-1} = 6.5$). Assuming the range between -4 MeV (repulsion) and 4 MeV (attraction) for $\Delta B_{\Lambda\Lambda}$, the neutron energy should be between 7.3 MeV and 15.3 MeV. Note that this $\Delta B_{\Lambda\Lambda}$ is for the $(1s_\Lambda 1p_\Lambda)$ configuration and is different from the $\Delta B_{\Lambda\Lambda}$ for the $(1s_\Lambda 1s_\Lambda)$ configuration found in emulsion experiments. The latter was determined to be 4 MeV–5 MeV, and the former is most likely considerably smaller due to the smaller overlap of the Λs' wave functions. The neutron energy for the ground state production is $T_n = 11.3 \text{ MeV} + 10 \text{ MeV} + \Delta B_{\Lambda\Lambda}$ and is equal to 25.8 MeV for $\Delta B_{\Lambda\Lambda} = 4.5$ MeV.

The cuts, described in the previous section were used to obtain a neutron spectrum with the maximum sensitivity. The resulting spectrum is searched for an evidence of a peak.

The following claims are made:

- The neutron spectrum consists of a smooth background and, possibly, a mono-energetic neutron peak of Gaussian shape with the known width,
- The shape of the background does not change as a function of the missing mass cut and can be extracted from a neutron spectrum for the events with low Ξ^- stopping probability.

Thus, the neutron spectrum obtained using the optimized cuts consists of a background with the known shape and, possibly, a Gaussian peak. The background shape is extracted by fitting the neutron spectrum for the events with missing mass greater than 11.65 GeV/c^2 (Ξ^- stopping rate is negligible), as shown in Figure 5.5.

The following observations provide justification for the assumptions above:

- Background appears to be smooth and its magnitude changes slowly, background can be well fit with a polynomial (good χ^2).
- The shape obtained from the fit can be scaled to fit the neutron spectra for other missing mass cuts with no worsening of the χ^2.

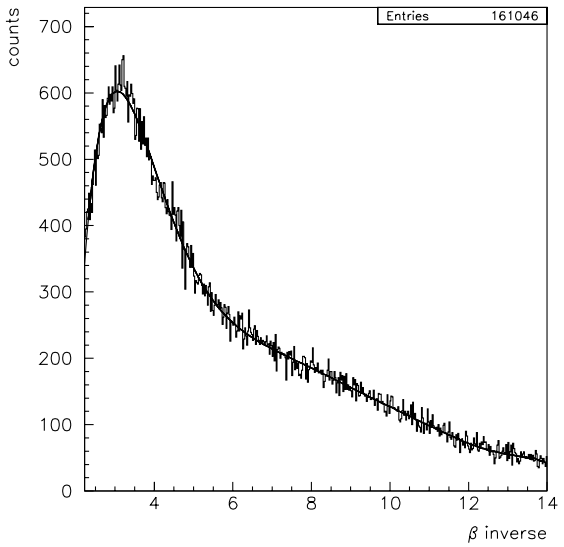

Figure 5.5: Neutron spectrum for events with unlikely Ξ^- stop (background), fitted with polynomial.

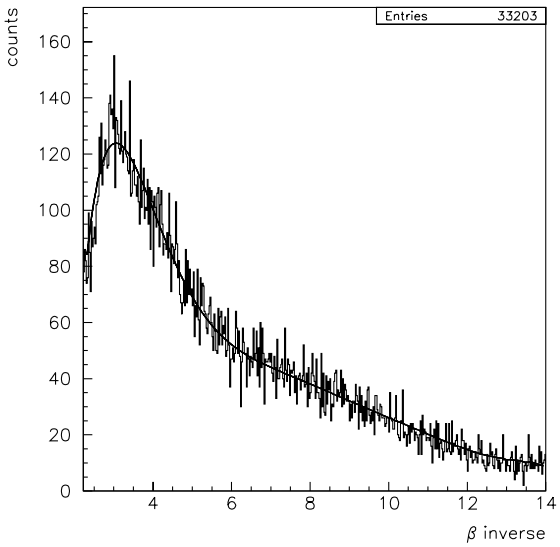

Figure 5.6: Neutron spectrum with optimized cuts (highest sensitivity), fitted with scaled background (scale factor is the only parameter of the fit).

Shown in Figure 5.6 is the neutron spectrum with optimized cuts, with a fitted scaled background on top. The scaled background fits the spectrum very well and no sign of a mono-energetic peak is present. When the same spectrum is fitted with the scaled background plus a Gaussian peak of known width at a given location, the magnitude of the peak and associated statistical error can be used to set an upper limit on the number of events in the peak. The statistical nature of the background will cause the number of events in the fitted peak to swing between negative and positive values, as the center of the fitted peak is moved along the range of β^{-1}. Therefore, the problem of non-physical negative upper limits arises. To avoid that

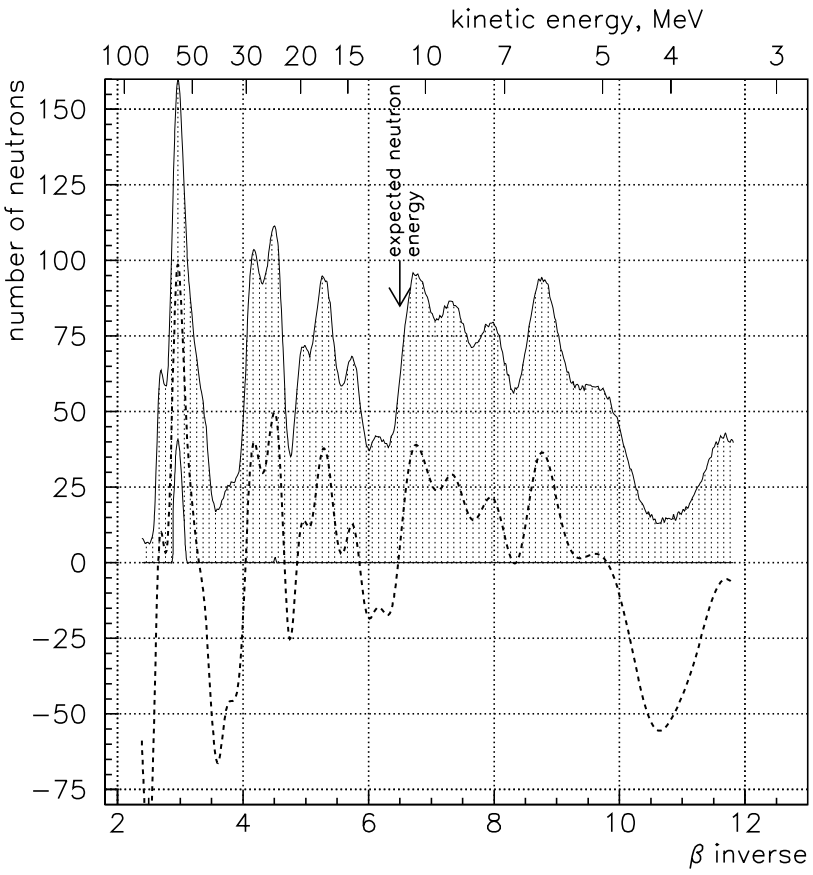

Figure 5.7: The number of mono-energetic neutrons in a Gaussian peak as a function of the neutron β^{-1}. The dashed curve shows the best fit value. The shaded band indicates the 90% confidence level interval for the number of neutrons. The arrow indicates the expected neutron energy, with the assumptions described in the text.

problem, an ordering principle, described by Feldman and Cousins[51], is used. A description of the method, along with an example of its application for a particular neutron energy, can be found in Appendix A.

In a single fit, the position of the hypothesized neutron peak is fixed at a particular neutron energy and the corresponding peak width value is used as determined in the Monte Carlo (Figure 3.3). Carrying out fits for a range of neutron energies, boundaries on the neutron count in a mono-energetic neutron peak for the whole range of energies is obtained. As the result of the fit procedure, a set of confidence intervals is obtained, one interval for each value of neutron energy used in the fit. An interval is a pair of numbers: lower and upper limits on the number of neutrons in a hypothesized mono-energetic neutron peak (for most intervals the lower limit is equal to zero). The 90% confidence interval is defined in the following way: if repeated measurements of an

unknown quantity were made and for each measurement its corresponding interval was found then the true value of the unknown would be contained in the found intervals in 90% of the measurements.

The result of such procedure is shown in Figure 5.7. The dashed curve is the best fit value for the number of mono-energetic neutrons as a function of the neutron β^{-1}, determined from the series of fits. The values on the curve fluctuate around zero, staying compatible with being zero in the whole range of neutron energies (except for a high energy region about $\beta^{-1} = 3$, far away from expected energy region). The shaded region is a 90% confidence band, i.e. the interval between lower and upper boundaries at a particular value of neutron energy represents the 90% confidence interval on the number of neutrons.

The neutron count (number of neutrons in a peak) n is converted to branching ratio b, using the knowledge of Ξ^- stopping rate ν (=31.7%) and neutron detection efficiency $\epsilon(\beta^{-1})$, shown in Figure 3.2, according to the formula

$$b = \frac{n}{\epsilon(\beta^{-1})\nu N},$$

where N is the background-subtracted number of events (=52780). Shown in Figure 5.8 is the branching ratio for the reaction $(\Xi^-, {}^{12}\mathrm{C})_{\mathrm{atom}} \rightarrow^{12}_{\Lambda\Lambda}\mathrm{B} + \mathrm{n}$. The dashed curve is found from the best fit value and the shaded region is a 90% confidence band. The size of the interval is determined by the number of Ξ^- stops, the magnitude of the background and the number of events in the hypothesized mono-energetic neutron peak found in the fit. The expected neutron energy for $\Delta\mathrm{B}_{\Lambda\Lambda} = 0$ and B_Λ as described above is indicated by an arrow and the corresponding upper limit is 3.3%. Difference between the nominal and the real values for $\Delta B_{\Lambda\Lambda}$ and B_Λ determines the real neutron energy. It is expected to be within ≈ 4 MeV from the central value.

This is below the two theoretical predictions (for cases different from the one presented here), discussed in Section 5.1:
$(\Xi^-, {}^{6}\mathrm{Li})_{\mathrm{atom}} \rightarrow^{6}_{\Lambda\Lambda}\mathrm{He} + \mathrm{n}$ – branching ratio = 5%[46], ${}^{12}_{\Xi}\mathrm{Be} \rightarrow^{11}_{\Lambda\Lambda}\mathrm{Be} + \mathrm{n}$ – branching ratio = 20%[48].

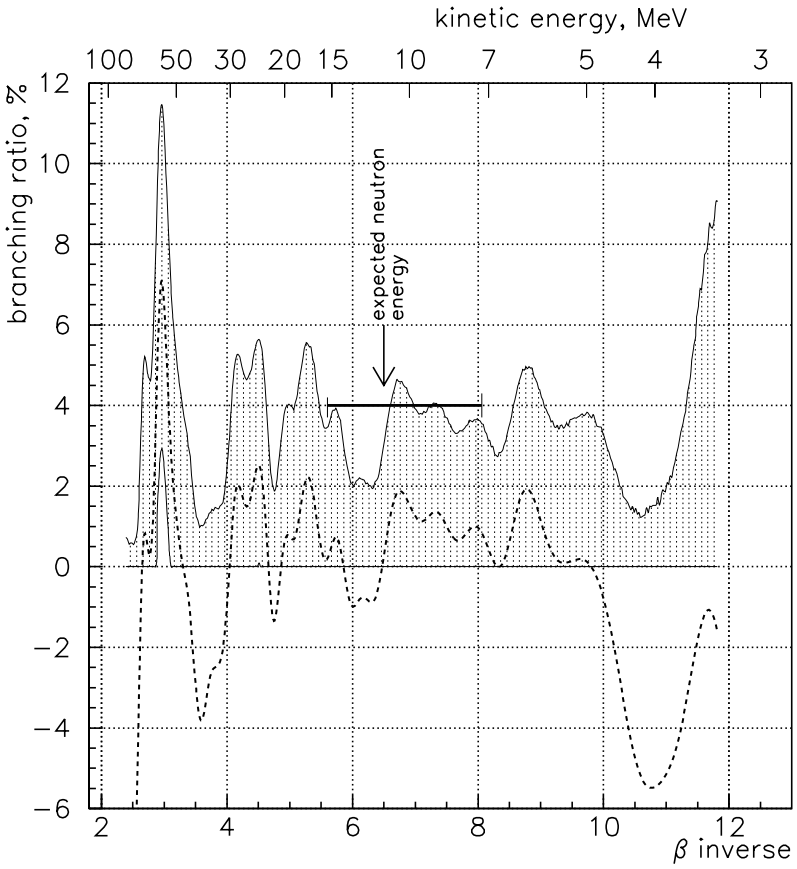

Figure 5.8: The branching ratio for double-Λ hypernuclear formation via neutron emission $(\Xi^-, {}^{12}\mathrm{C})_{\mathrm{atom}} \rightarrow {}^{12}_{\Lambda\Lambda}\mathrm{B}^* + \mathrm{n}$ as a function of the neutron β^{-1}. The dashed curve shows the branching ratio obtained from the best fit value for the number of neutrons in the peak. The shaded band indicates the 90% confidence level interval for the branching ratio. The arrow indicates the expected neutron energy, with the assumptions described in the text and the bar shows the range over which the neutron β^{-1} varies when $\Delta\mathrm{B}_{\Lambda\Lambda}$ varies from -4 MeV to +4 MeV.

Chapter 6

Direct production of Ξ and double-Λ hypernuclei

With the advent of spectrometers, it became possible to study hypernuclei through the reconstruction of missing mass. Hypernuclei in the S=–1 sector have been studied using this method quite successfully. Similarly to production of S=–1 hypernuclei in (π^+,K^+) and (K^-,π^-), the (K^-,K^+) reaction can be used to create S=–2 hypernuclei.

The S=–2 sector is significantly less studied due to:

- lower elementary cross section,
- higher momentum transfer and
- two-step nature of direct double-Λ hypernuclear production.

The cross section for direct double-Λ hypernuclear production is expected to be orders of magnitude smaller than the cross section for Ξ hypernuclear production. A. J. Baltz *et al.* [24] predicted the cross section of direct double-Λ production in the reaction ^{16}O(K^-,K+)$^{16}_{\Lambda\Lambda}$C* to be a few nb/sr for $p_{K^-} = 1.1$ GeV/c. However, C. B. Dover *et al.* [26] pointed out that mixing of Ξ and double-Λ hypernuclear states may introduce an amplitude for direct one-step double-Λ hypernuclear production and make the cross section of double-Λ hypernuclear production considerably larger. In this experiment the statistics were not sufficient to provide definite information about directly produced double-Λ hypernuclear states. Only an upper limit for direct double-Λ hypernuclear production can be established.

C. B. Dover and A. Gal [31] found the Ξ^--nucleus potential well depth to be $\approx$ 21 MeV – 24 MeV based on their analysis of emulsion data. $1p$ and $1s$ single-particle Ξ^- states are expected to be bound for this value of the potential.
J. K. Ahn *et al.* recently reported evidence for bound Ξ hypernuclei produced in the (K^-,K^+) reaction on a scintillating fiber target [36]. Their data, in their interpretation, favored the Ξ^--nucleus potential well depth of $\approx$ 17 MeV and they concluded that the value of 24 MeV for the potential was very unprobable.

Since the Ξ hypernuclear production cross section is much smaller than free Ξ^- production cross section, only the bound or nearly bound states can be identified reliably through their excitation energy. This is the region where free Ξ^- production cross section is zero or small.

High resolution and background suppression are important in order to observe these states. Although the experimental resolution in E885 is not sufficient to observe discrete hypernuclear states, an estimate of cross section can be made and the excitation energy spectrum can be compared to the theoretical predictions for different potential well depths.

6.1 Detection of directly produced hypernuclei

The missing mass value for a directly produced hypernucleus is equal to the mass of the hypernuclear state. Therefore, provided sufficient statistics and resolution, hypernuclear states would appear as discrete peaks in the missing mass distribution. Their width would be determined by their natural width and the experiment's resolution.

It is convenient to plot excitation energy instead of missing mass with the definition of excitation energy as missing mass minus masses of ^{11}B and Ξ^-:

$$E = M - M_{^{11}B} - M_{\Xi^-},$$

where E and M are excitation energy and missing mass respectively. With the above definition, bound Ξ hypernuclear states (states for which the Ξ^- is bound) will map to the region of negative excitation energy and the value of excitation energy will be the negative of the binding energy of the Ξ^-, $-B_\Xi$. Unbound states, along with free Ξ^- production, will contribute to the region of positive excitation energy. The cross section for direct hypernuclear production is expected to be much smaller than the one for free Ξ^- production.

The ground state of the double-Λ hypernucleus $^{12}_{\Lambda\Lambda}$Be is expected to be at the excitation energy of $\approx$ -41.5 MeV for $\Delta B_{\Lambda\Lambda} = 4.5$, assuming $B_\Lambda = 10$ MeV.

Although the region of negative excitation energy, where a signal from direct hypernuclear production is expected, is kinematically unaccessible for free Ξ^- production, the much higher cross section of the latter makes background suppression, resolution and acceptance studies critical for interpretation of the data.

6.2 Normalization of the excitation energy spectrum

Using knowledge of the acceptance for a particular reaction, the excitation spectrum units of "number of events per bin" for that reaction can be converted to "differential cross section per bin". This procedure is called "normalization". Note that normalization depends on acceptance and is, thus, reaction specific.

The data are normalized to the known cross section of free Ξ^- production on hydrogen (hydrogen contained in CH_2 target). The parameters of the CH_2 and diamond targets are given in Table 6.1. Due to the low statistics in the bound region, only an averaged differential cross section over the spectrometer acceptance $\theta_{K^+} < 14^\circ$ can be obtained. It is denoted in the text as $\left\langle \frac{d^2\sigma}{d\Omega dE} \right\rangle$ with averaging over solid angle understood. The Ξ^- production on free protons is taken to have an average cross section of 35 μb/sr [31]. Ξ^- production on carbon, which is present in targets used both in production and calibration running, is used to relate production and calibration data.

Target	Thickness λ, cm^{-2}		Thickness, cm	Density, g/cm^3
	hydrogen	carbon		
Diamond	$\approx 7.6 \times 10^{21}$ [a]	8.27×10^{23}	5	3.3
CH_2	10.5×10^{23}	5.25×10^{23}	13	0.94

Table 6.1: Parameters of the diamond and CH_2 targets

[a] From epoxy glue in the target.

6.2.1 Derivation of normalization formula

The number of detected events per unit missing mass is [a]

$$\frac{dN}{dE} = \lambda \int dt\, I(t)\, \epsilon(t)\, \beta(t) \int d\Omega\, \alpha(E,\Omega)\, \frac{d^2\sigma}{d\Omega dE}, \tag{6.1}$$

where λ is number-density times target length, $\alpha(E,\Omega)$ is the acceptance as a function of the missing mass and the secondary particle angle and is reaction-dependent, $\epsilon(t)$ is the data acquisition live time, $\beta(t)$ is the overall event reconstruction efficiency for a particular set of cuts and $I(t)$ is the beam rate. For a given target, $\epsilon(t)$ and $\beta(t)$ depend mostly on the beam intensity. The first integral can be written as

$$\int dt\, I(t)\, \epsilon(t)\, \beta(t) = B\, \langle \beta \rangle,$$

where

$$B = \int dt\, I(t)\, \epsilon(t)$$

[a] The integration limits are not shown for brevity. The time and energy integration is done from $-\infty$ to $+\infty$ and the solid angle integration is done over a forward cone with $\theta < \theta_{max}$. The same symbol α is used to denote acceptance, whether it is averaged over angle and/or energy or not. The absence of E in the argument list means that the acceptance was averaged over energy and the absence of Ω means that it was averaged over solid angle.

is the integrated flux $\times$ live time (can be thought of as "effective beam") and

$$\langle \beta \rangle = \frac{\int dt\, I(t)\, \epsilon(t)\, \beta(t)}{\int dt\, I(t)\, \epsilon(t)}$$

is the beam-weighted average event reconstruction efficiency.

The second integral in (6.1) can be written as

$$\int d\Omega\, \alpha(E,\Omega)\, \frac{d^2\sigma}{d\Omega dE} = \frac{\int d\Omega\, \alpha(E,\Omega) \frac{d^2\sigma}{d\Omega dE}}{\int d\Omega \frac{d^2\sigma}{d\Omega dE}}\, \frac{\int d\Omega \frac{d^2\sigma}{d\Omega dE}}{\Delta\Omega}\, \Delta\Omega = \alpha(E) \left\langle \frac{d^2\sigma}{d\Omega dE} \right\rangle \Delta\Omega,$$

where

$$\alpha(E) = \frac{\int d\Omega\, \alpha(E,\Omega) \frac{d^2\sigma}{d\Omega dE}}{\int d\Omega\, \frac{d^2\sigma}{d\Omega dE}}$$

is the angle-averaged acceptance and

$$\left\langle \frac{d^2\sigma}{d\Omega dE} \right\rangle = \frac{\int d\Omega \frac{d^2\sigma}{d\Omega dE}}{\Delta\Omega}$$

is the angle-averaged double-differential cross section.

Putting everything together

$$\frac{dN}{dE} = \lambda\, B\, \langle \beta \rangle\, \alpha(E) \left\langle \frac{d^2\sigma}{d\Omega dE} \right\rangle \Delta\Omega. \tag{6.2}$$

Integrating Equation (6.2) over E

$$N = \lambda\, B\, \langle \beta \rangle\, \alpha \left\langle \frac{d\sigma}{d\Omega} \right\rangle \Delta\Omega, \tag{6.3}$$

where

$$\alpha = \frac{\int dE\, d\Omega\, \alpha(E,\Omega)\, \frac{d^2\sigma}{d\Omega dE}}{\int d\Omega\, dE \frac{d^2\sigma}{d\Omega dE}}$$

is the angle- and energy-averaged acceptance and

$$\left\langle \frac{d\sigma}{d\Omega} \right\rangle = \frac{\int d\Omega dE \frac{d^2\sigma}{d\Omega dE}}{\Delta\Omega}$$

is the angle-averaged differential cross section.

Applying the Equations (6.2) and (6.3) to the (K^-,K^+) reaction on CH_2 and diamond targets, the following is obtained for the reactions indicated (subscript and superscript indicate respectively the target material, either CH_2 or diamond, and target nuclei, either hydrogen or carbon):

1. free Ξ^- production on carbon in CH_2 target

$$N^C_{CH_2} = \lambda^C_{CH_2} B_{CH_2} \langle\beta\rangle_{CH_2} \alpha^C \left\langle \frac{d\sigma}{d\Omega} \right\rangle^C \Delta\Omega,$$

2. free Ξ^- production on hydrogen in CH_2 target

$$N^H_{CH_2} = \lambda^H_{CH_2} B_{CH_2} \langle\beta\rangle_{CH_2} \alpha^H \left\langle \frac{d\sigma}{d\Omega} \right\rangle^H \Delta\Omega, \tag{6.4}$$

3. free Ξ^- production on carbon in diamond target

$$N^C_{diam} = \lambda^C_{diam} B_{diam} \langle\beta\rangle_{diam} \alpha^C \left\langle \frac{d\sigma}{d\Omega} \right\rangle^C \Delta\Omega,$$

4. hypernuclear production on carbon in diamond target

$$\left(\frac{dN}{dE}\right)^C_{diam} = \lambda^C_{diam} B_{diam} \langle\beta\rangle_{diam} \alpha^C(E) \left\langle \frac{d^2\sigma}{d\Omega dE} \right\rangle^C \Delta\Omega.$$

From the first two equalities

$$\left\langle \frac{d\sigma}{d\Omega} \right\rangle^C = \frac{N^C_{CH_2}}{N^H_{CH_2}} \frac{\lambda^H_{CH_2}}{\lambda^C_{CH_2}} \frac{\alpha^H}{\alpha^C} \left\langle \frac{d\sigma}{d\Omega} \right\rangle^H \tag{6.5}$$

and from the last two

$$\left\langle \frac{d^2\sigma}{d\Omega dE} \right\rangle^C = \left(\frac{dN}{dE}\right)^C_{diam} \frac{\alpha^C}{\alpha^C(E)} \frac{1}{N^C_{diam}} \left\langle \frac{d\sigma}{d\Omega} \right\rangle^C. \tag{6.6}$$

Substituting result for $\left\langle \frac{d\sigma}{d\Omega} \right\rangle^C$ from Equation (6.5) into Equation (6.6)

$$\left\langle \frac{d^2\sigma}{d\Omega dE} \right\rangle^C = \left(\frac{dN}{dE}\right)^C_{diam} \frac{\alpha^H}{\alpha^C(E)} \frac{\lambda^H_{CH_2}}{\lambda^C_{CH_2}} \frac{N^C_{CH_2}}{N^C_{diam} N^H_{CH_2}} \left\langle \frac{d\sigma}{d\Omega} \right\rangle^H = A \left(\frac{dN}{dE}\right)^C_{diam}, \tag{6.7}$$

where

$$A = \frac{\alpha^H}{\alpha^C(E)} \frac{\lambda^H_{CH_2}}{\lambda^C_{CH_2}} \frac{N^C_{CH_2}}{N^C_{diam} N^H_{CH_2}} \left\langle \frac{d\sigma}{d\Omega} \right\rangle^H$$

is the normalization factor.

Equation (6.7) was used to get the cross section scale for the excitation energy spectrum. Since the hypernuclear production acceptance varies very little with energy over the small region of interest about zero excitation energy, instead of the energy-dependent acceptance $\alpha^C(E)$ the acceptance calculated for a fixed excitation energy of -10 MeV was used. A summary of all the elements in the formula is provided below.

- $\left\langle \frac{d^2\sigma}{d\Omega dE} \right\rangle^C$ – angle-averaged double-differential cross section of hypernuclear production.
- $\left(\frac{dN}{dE} \right)^C_{diam}$ – number of hypernuclear-production events in a missing mass interval dE.
- α^H – angle- and energy-averaged acceptance for free Ξ^- production on hydrogen.
- $\alpha^C(E)$ – angle-averaged acceptance for hypernuclear production. The argument E indicates the dependence on energy.
- $\lambda^H_{CH_2}$ – target thickness for hydrogen in CH_2 target.
- $\lambda^C_{CH_2}$ – target thickness for carbon in CH_2 target.
- $N^C_{CH_2}$ – number of events of free Ξ^- production on carbon in CH_2 target.
- $N^H_{CH_2}$ – number of events of free Ξ^- production on hydrogen in CH_2 target.
- N^C_{diam} – number of events of free Ξ^- production on carbon in diamond target.
- $\left\langle \frac{d\sigma}{d\Omega} \right\rangle^H$ – angle-averaged differential cross section of Ξ^- production on hydrogen.

The measurement of the ratio $N^C_{CH_2}/N^C_{diam}$ is described in the next subsection and the calculation of the normalization factor A is given in subsection 6.2.3.

6.2.2 Calibration Data

Calibration data taken with CH_2 target is used to the get cross section scale for processes in the E<0 region of the excitation energy spectrum. A few things that are not calculated in the Monte Carlo, such as tracking efficiency, reconstruction efficiency, data acquisition live time and other possible losses, are corrected for by normalizing to a known cross section of free Ξ^- production. The amount of calibration data is related to the production data by using the ratio of the total number of

reconstructed events for the Ξ^- production on carbon with an additional correction for the different amounts of carbon in the two targets. This way the dependence of the reconstruction efficiency on the beam intensity is folded into the number of reconstructed events and automatically corrected for as shown in Equation (6.7). This is especially relevant for E885 due to the fact that calibration data was taken with a beam intensity two times lower than the average throughout the run.

The missing mass spectrum for CH_2 data (mass of the target nucleus = proton mass) is shown in Figure 6.1. The peak corresponds to Ξ^- production on hydrogen and the rest of events to Ξ^- production on carbon. The distribution was fitted with a template of the missing mass spectrum from the diamond target data plus a Gaussian peak. Free parameters were the scale factor for the template and the Gaussian peak's width and size. From the fit, the number of events for Ξ^- production on hydrogen and carbon are 480 and 424 respectively.

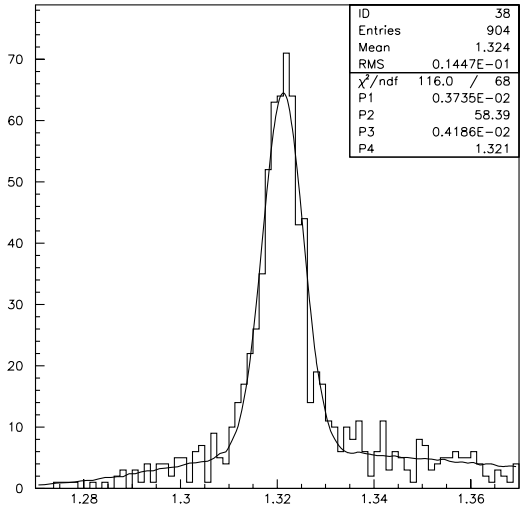

Figure 6.1: Missing Mass for 13 cm long CH_2 target data with all cuts applied, fitted with the template of missing mass for Ξ^- production on carbon and Gaussian peak. Resolution determined from the fit is 4.2 MeV r.m.s. (hydrogen kinematics)

It was found that the ratio of total numbers of reconstructed events of Ξ^- production events on carbon for the two targets

$$\frac{N^C_{diam}}{N^C_{CH_2}} = 125.6 \pm 6.3 \tag{6.8}$$

and the ratio of the live-time and target thickness corrected total beam fluxes

$$\frac{\lambda^C_{diam} B_{diam}}{\lambda^C_{CH_2} B_{CH_2}} = 186.6 \tag{6.9}$$

The values for λ^C_{diam} and $\lambda^C_{CH_2}$ are given in Table 6.1 and the values for the effective beam fluxes B_{diam} and B_{CH_2} are respectively 5.34×10^{11} kaons and 4.50×10^9 kaons.

Should the overall event reconstruction efficiencies for the two cases be equal the ratios (6.8) and (6.9) would be equal too. The significant difference in the two numbers is explained by the reconstruction efficiency dependence on the beam intensity. From

$$\frac{N^C_{diam}}{N^C_{CH_2}} = \frac{\lambda^C_{diam} B_{diam}}{\lambda^C_{CH_2} B_{CH_2}} \frac{\langle \beta_{diam} \rangle}{\langle \beta_{CH_2} \rangle}$$

the ratio of overall event reconstruction efficiencies for diamond and CH_2 targets is

$$\frac{\langle \beta_{diam} \rangle}{\langle \beta_{CH_2} \rangle} = 0.67 \tag{6.10}$$

As was pointed out above, calibration data were taken with low beam intensity and, therefore, reconstruction efficiency for the calibration data is expected to be higher. Most reduction in the reconstruction efficiency comes from the cuts on the beam track. One should expect the above-mentioned formulas to produce equal ratios for runs with nearly equal beam intensity. This was confirmed to be the case – number of Ξ^- production events in low intensity production runs is related to the number of Ξ^- production events on carbon in calibration runs in the same way as their corresponding live-time and target thickness corrected total beam fluxes.

The absolute value for the overall event reconstruction efficiency for free Ξ^- production on hydrogen in CH_2 target was found from Equation (6.4) to be $\langle \beta \rangle_{CH_2} \approx 19\%$, using the value of 35 μb/sr [31] for the cross section of Ξ^- production on hydrogen $K^- + p \to K^+ + \Xi^-$. Using (6.10) $\langle \beta \rangle_{diam} \approx 13\%$. The low values are not unexpected and are mostly due to the tightness of the cuts used for direct hypernuclear production analysis. A separate study showed that for a loose set of cuts, the value for $\langle \beta \rangle_{CH_2}$ becomes about 60%, consistent with expectations.

6.2.3 Normalization factor

The summary of parameters used for normalization in (6.7) is given below for two different acceptances: the first one is full spectrometer acceptance ($\theta_{K^+} < \theta_{max} = 14^\circ$) and the second one is for limited acceptance ($\theta_{K^+} < \theta_{max} = 8^\circ$). Note that the

maximum θ_{K^+}, degrees	α^H, %	$\alpha^C(-10\ MeV)$, %	$\lambda^H_{CH_2}/\lambda^C_{CH_2}$	$N^C_{CH_2}/N^C_{diam}$	$\langle d\sigma/d\Omega \rangle^H$, μb/sr	$N^H_{CH_2}$
14	8.1	14.3	2	1/125.6	35	480
8	14.4	16.4	2	1/127.9	35	240

Table 6.2: A summary of parameters used for normalization. The value used for the cross section of Ξ^- production on hydrogen is from C. B. Dover and A. Gal [31].

weak angular dependence of free Ξ^- production (see, for example, [31] for a plot of angular dependence) is neglected when calculating the averaged differential cross

section $\langle d\sigma/d\Omega \rangle^H$ and the nominal zero-angle value is used. The following values for normalization factor A, giving averaged differential cross section per event in a 1 MeV/c^2-wide bin, are obtained:

$$A = \begin{cases} 0.66 \pm 0.05 \text{ nb/sr} & \text{for } \theta_{\max} = 14^\circ \\ 2.00 \pm 0.2 \text{ nb/sr} & \text{for } \theta_{\max} = 8^\circ \end{cases} \tag{6.11}$$

For a histogram with 1 MeV/c^2-wide bins, this factor relates counts per MeV/c^2 to angle-averaged differential cross section per MeV/c^2 (A multiplied by counts in 1 MeV/c^2-wide interval will give cross section). The shown statistical errors of the cross section scale for the two different θ_{max} are mostly due to the limited amount of calibration data, namely the numbers of free Ξ^- production reactions on hydrogen and carbon in CH_2 target. The systematic uncertainty, excluding the uncertainty of the elementary cross section of Ξ^- production on hydrogen, is expected to be below the statistical error. The uncertainty of the elementary cross section of Ξ^- production on hydrogen does not affect the comparison of the data and theory because the theoretical DWIA calculations are normalized to the same elementary cross section. As long as the same value for the elementary cross section is used, which is the case here, in both the theoretical calculations and cross section scale calculation, the ratio data-to-theory is not affected.

6.3 Missing mass resolution

The data taken with CH_2 target can be used to study missing mass resolution. Two sets of data are available with CH_2 target. The first set used an 8 cm long target and the second set, which was acquired over a shorter time period, was run using a 13 cm long target. The first data set was used to study the spectrometer's intrinsic resolution and, in particular, evaluate the tails of the resolution function. The second set was used to derive the width of the resolution function. The contribution of energy loss effects to the resolution for the 13 cm long CH_2 target is expected to be similar to the contribution from the 5 cm long diamond target.

The numerical value of missing mass resolution depends on the target mass (mass of the target is included in the formula for missing mass). Therefore the resolution specific to Ξ^- production on hydrogen (what we can measure directly) is used to infer the missing mass resolution for carbon kinematics (not measurable directly), using simple algebraic considerations.

Due to the 2-body nature of the Ξ^- production on hydrogen the missing mass spectrum is a peak whose width equals the experimental resolution plus background from Ξ^- production on carbon. In addition to the peak width, we are also interested in the tail of the resolution. The study of the resolution tails is important in view of the need to correctly identify the weak signal of hypernuclear production that is not well separated on the missing mass scale from the huge signal of free Ξ^- production.

The background, represented by events of Ξ^- production on carbon, is subtracted using the missing mass spectrum for carbon target. The resulting peak, is shown in Figure 6.2. A special parameter representing a correction to the secondary momentum was adjusted to set the centroid of the peak at the exact value of the Ξ^- mass. The magnitude of the correction was about 30 MeV/c and it was most probably due to errors in the magnetic field map of the 48D48 spectrometer's magnet.

Width of the peak from the Gaussian fit is 3.8 MeV/c^2 r.m.s. It can be seen from the plot that the resolution is reasonably close to being Gaussian.

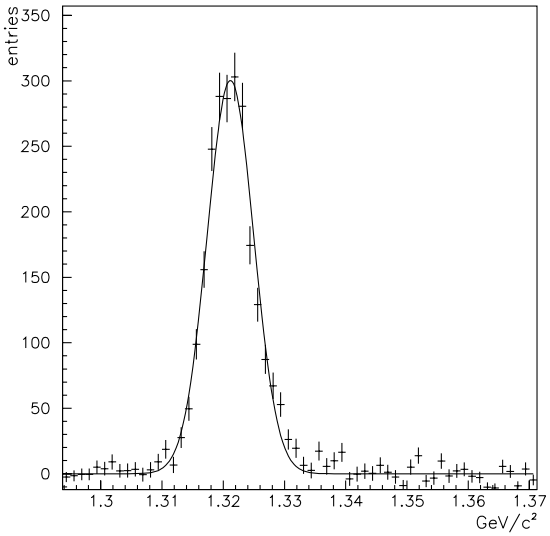

Figure 6.2: Missing mass for Ξ^- production on hydrogen in 8 cm long CH_2 target. Background from reactions on carbon is subtracted using data sample taken with carbon target. The solid line shows the best Gaussian fit.

The missing mass for the 13 cm CH_2 target is shown in Figure 6.1. The width of the missing mass resolution was measured to be 4.2 MeV/c^2 r.m.s. for hydrogen kinematics.

To calculate missing mass resolution in carbon kinematics (carbon nucleus mass as target mass) the following argument can be used. The missing mass error is caused by errors in determination of primary and secondary momenta and production angle. If we can relate the influence of the momentum errors on the missing mass errors for both hydrogen and carbon kinematics then the missing mass resolution in carbon kinematics can be calculated from the known resolution in hydrogen kinematics.

The missing mass depends on the magnitude of the primary and secondary momenta p_1 and p_2 and the polar angle of the secondary track θ (the beam track is assumed to have only z non-zero component). The missing mass error and contributions from momentum magnitude and angle errors can then be estimated by taking partial derivatives with respect to p_1, p_2 and θ and multiplying them by corresponding error estimates Δp_1, Δp_2 and $\Delta\theta$. Partial derivatives are:

$$\frac{\partial M}{\partial p_1}(\theta = 0^\circ) \;=\; \frac{1}{M}\left[\frac{p_1}{E_1}(M_{target} + E_2) - p_2\right],$$

$$\frac{\partial M}{\partial p_2}(\theta = 0^\circ) = -\frac{1}{M}\left[\frac{p_2}{E_2}(M_{target} + E_1) - p_1\right],$$
$$\left|\frac{\partial M}{\partial \theta}\right| = \frac{p_1 p_2 sin\theta}{M}$$

The derivatives taken with respect to momentum magnitude are shown for $\theta = 0^\circ$ for simplicity. An upper limit on the derivative with respect to θ can be set assuming $p_1 = 1.8$ GeV/c, $p_2 = 1.3$ GeV/c, $M = 11.7$ GeV/c^2 and $\theta = 14^\circ$. Then the derivative with respect to θ equals 0.045 GeV/c^2. The angle error $\Delta\theta$ can be estimated in several ways. Estimating the track position error in the x-y plane over Δz=300 mm ($\approx$ distance between drift chambers FD1 and FD2) to be 1 mm, we obtain the angle error $\Delta\theta$ = atan(1/300)=0.003 rad. In the alternative method, the angle error is estimated from the known missing mass error of $\approx$ 4 MeV/c^2. If it is attributed solely to the momentum magnitude error resulting from the error of determining the angle by which the K^+ is bent in the spectrometer and assuming the secondary momentum 1200 MeV/c and the bending angle 30°, the angle error is (4 MeV/c^2 missing mass error corresponds to about 6 MeV/c secondary momentum error) $\frac{6 \text{ MeV/c}}{1200 \text{ MeV/c}} \times 30^\circ = 0.15^\circ = 0.0026$ rad. Both methods give consistent results – an angle error of about 0.003 rad. Then the missing mass error due to the angle error is 0.045 GeV/c$^2\times$ 0.003 = 0.14 MeV/c^2. It is much smaller than the measured missing mass error. We conclude that the contribution to the missing mass error from using not exact figure for the angle θ in the missing mass formula is much smaller than the contribution from the momenta magnitude error and can be ignored.

derivative	free Ξ^- production	hypernuclear production	ratio of 3rd and 2nd columns
$\partial M/\partial p_1$	0.72	0.97	1.34
$\partial M/\partial p_2$	-0.60	-0.90	1.50

Table 6.3: Partial derivative values obtained for Ξ^- production on hydrogen and hypernuclear production.

Partial derivative values obtained for Ξ^- production on hydrogen and hypernuclear production are shown in Table 6.3. It can be seen that the errors in the determination of primary and secondary momenta contribute similarly to the missing mass resolution. The last column is the ratio of the values in the third and second columns and it can be seen that the ratios of derivatives in the third and second columns are close. The difference in the ratios means that without knowing the uncertainty in the primary and secondary momenta it would not be possible to predict the missing mass resolution in carbon kinematics exactly. However, the closeness of ratios means that a small error would be made, at most 10%. It is believed that the beam line

resolution is better than the spectrometer resolution. Then the statistical weight of the secondary momentum error must be greater than the one for primary momentum error. Therefore a value of 1.45 (closer to the ratio for $\partial M/\partial p_2$) was used as a factor relating missing mass resolutions in carbon and hydrogen kinematics. This value results in the missing mass resolution for carbon kinematics of 4.2 MeV/c^2 $\times$1.45 = 6.1 MeV/c^2.

6.4 Theoretical cross section

The theoretical cross section for different Ξ^--nucleus potentials can be compared with the experimental cross section. To make a meaningful comparison, theoretical differential cross section needs to be averaged over the same range of solid angle as the data and it needs to be folded with the measured resolution function.

Here the calculation of Y. Yamamoto *et al.* [39] for $\theta = 0^\circ$ differential cross section for $V_{0\,\Xi}$ = 16 MeV and 20 MeV is used. The angular dependence is calculated as described in Section 4.1 and shown in Figure 4.3.

The same angular dependence is used for both bound region, for which the angular dependence was calculated specifically, and for the unbound region, for which angular dependence was neither calculated nor found in the literature.

6.5 Comparison of data and theory for direct Ξ hypernuclear production

Excitation energy spectra for ^{12}C(K$^-$,K$^+$)X for two different limits on the polar angle of the outgoing K$^+$ θ <14° and θ < 8° are shown in Figure 6.3. The theoretical curves [39] for Ξ potential well depths 20 MeV (dashed curve) and 16 MeV (dotted curve), folded with 6.1 MeV r.m.s. experimental resolution are shown for comparison with the data. The expected location of the ground state of $^{12}_{\Lambda\Lambda}$Be (assuming $B_{\Lambda\Lambda}$ = 25 MeV) and the thresholds of $^{11}_{\Lambda}$Be + Λ and ^{11}B + Ξ^- production are indicated with arrows. A visual inspection shows that the theoretical curve for the value of the cascade-nucleus potential well depth $V_{0\,\Xi}$ = 16 MeV agrees with the data reasonably well in the region of excitation energy -20 MeV<E<0 MeV and much better so than the curve for $V_{0\,\Xi}$ = 20 MeV. There is notable disagreement between the data and theory for both values of the potential in the unbound region E>0, which might be explained by probably less reliable theoretical prediction for the unbound region. The event counts for the data and theory are summarized in Table 6.4.

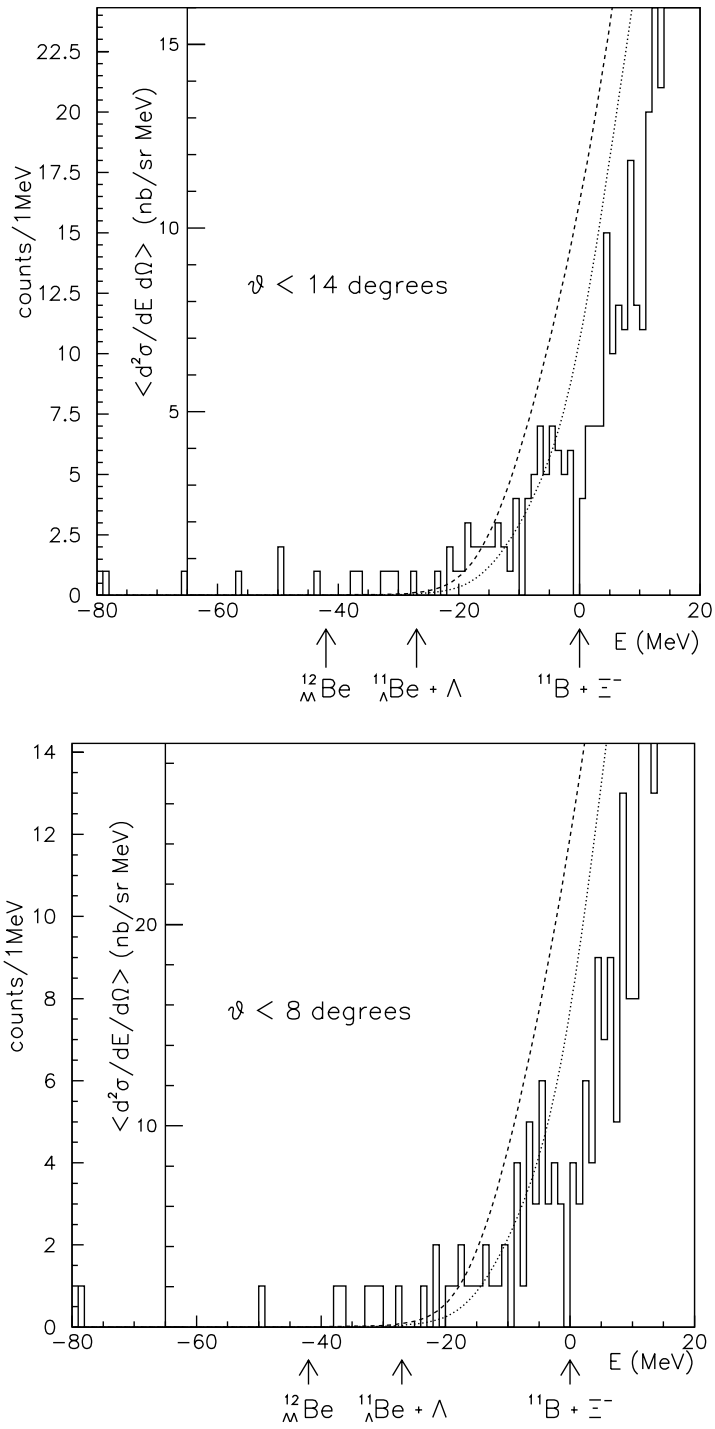

Figure 6.3: Excitation energy spectra for ^{12}C(K$^-$,K$^+$)X for θ_{K^+} <14° (top figure) and θ_{K^+} <8° (bottom figure) along with theoretical curves for $V_{0\,\Xi}$ equal to 20 MeV (dashed curve) and 16 MeV (dotted curve), folded with 6.1 MeV r.m.s. experimental resolution. The expected location of the ground state of $^{12}_{\Lambda\Lambda}$Be and the thresholds of $^{11}_{\Lambda}$Be + Λ and ^{11}B + Ξ$^-$ production are indicated with arrows.

θ_{max}, degrees	number of events in the interval -20 MeV<E<0 MeV		
	data	theory, $V_{0\,\Xi}$=16 MeV	theory, $V_{0\,\Xi}$=20 MeV
14	67	72	146
8	42	52	104

Table 6.4: The number of events in the region of excitation energy -20 MeV<E<0 MeV from the data and theory for two ranges of the K^+'s θ in the laboratory frame: θ <14° (full spectrometer acceptance) and θ <8°. The theoretical values are shown for two values of the cascade-nucleus potential well depth $V_{0\,\Xi}$ = 16 MeV and 20 MeV.

6.6 Upper limit on direct double-Λ hypernuclear production

Signal from direct double-Λ hypernuclear production is expected to appear lower on the excitation energy scale than the direct Ξ hypernuclear production:

$$E_{\Lambda\Lambda}^{12}\mathrm{Be} = M_{^{10}\mathrm{Be}} + 2M_\Lambda - B_{\Lambda\Lambda} - (M_{^{11}\mathrm{B}} + M_{\Xi^-}) = -17\ \mathrm{MeV} - B_{\Lambda\Lambda}.$$

Using B_Λ = 10 MeV and $\Delta B_{\Lambda\Lambda}$ = 5 MeV, the following value for excitation energy of the ground state double-Λ hypernuclei ${}^{12}_{\Lambda\Lambda}$Be is obtained:

$$E_{\Lambda\Lambda}^{12}\mathrm{Be} = -17\ \mathrm{MeV} - 2 \times 10\ \mathrm{MeV} - 5\ \mathrm{MeV} = -42\ \mathrm{MeV}.$$

Since the double-Λ hypernuclear states are expected to be much narrower than the resolution, they would appear as Gaussian peaks with the width close to the resolution width. Assuming that the signal in the excitation energy distribution comes from direct double-Λ hypernuclear production, an upper limit can be placed on the angle-averaged differential cross section of direct double-Λ hypernuclear state production. This is done by:

- calculating the number of events in an interval of excitation energy with the width equal to 2σ, where σ is the missing mass resolution and finding the corresponding 90% confidence level upper limit on the number of events (see Figure 6.4),
- multiplying the upper limit on the number of events in the interval of the width 2σ by 1/0.68, to account for the limited integration interval (68% of the total area is contained under a Gaussian in an interval centered at the mean and the 2σ total width) and
- converting the obtained upper limit on the number of events to an upper limit on the angle-averaged differential cross section using the earlier found (see Equation (6.11)) normalization factor $A = 0.66$ nb/sr.

The resulting upper limit as a function of the total binding energy of the two Λ's is shown in Figure 6.5.

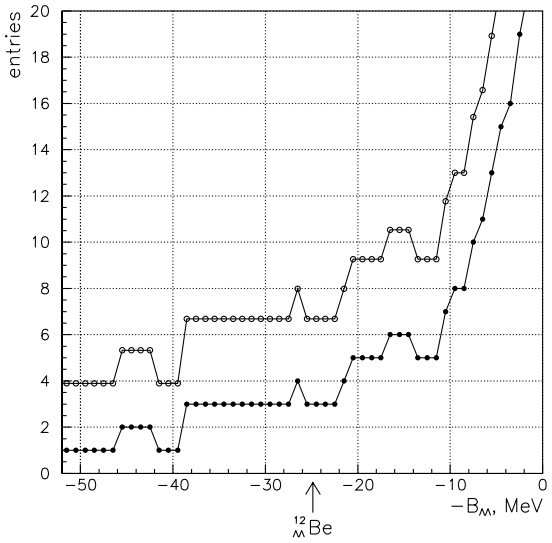

Figure 6.4: The number of events in an interval of the excitation energy spectrum with the width of $2\sigma = 12.2$ MeV (solid circles) and corresponding 90% upper limit (empty circles) as a function of the negative of the total binding energy of the two Λ's in ${}^{12}_{\Lambda\Lambda}$Be (this scale is shifted relative to the excitation energy scale by +17 MeV).

6.7 Background

Events in the region of negative values of excitation energy (E<0) are either background or hypernuclear events. Background in the region of negative values of excitation energy can be divided into two groups:

- Flat background caused by particle misidentification, severe tracking errors etc. Such background might have some structure over a wider region of the missing mass distribution, but on a sufficiently small, $\approx$ 100 MeV scale, it should be flat. This was confirmed when observing the background in the bound region of the excitation energy distribution obtained using a loose set of cuts (hence considerable background contamination).

- Leakage from E>0 due to finite missing mass resolution.

Background of the first kind can be easily estimated by observing the region further below zero where leakage becomes negligible. There are 6 events in the interval

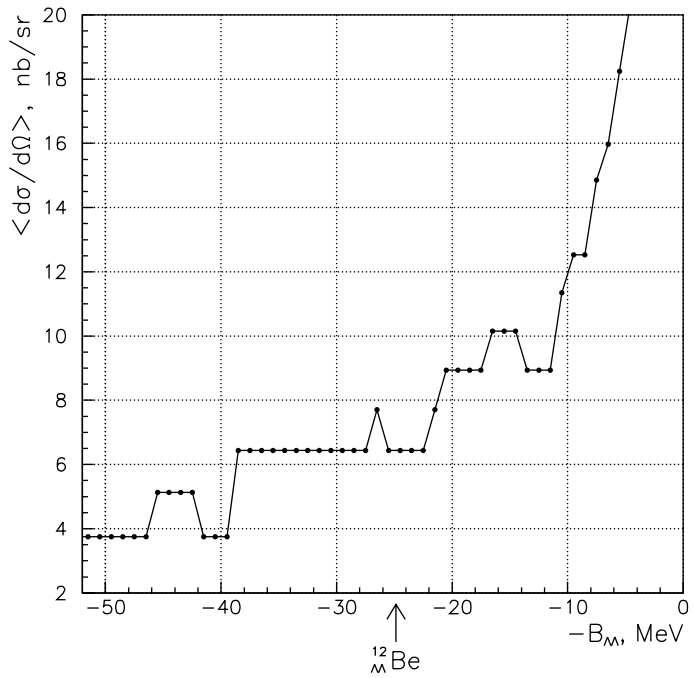

Figure 6.5: 90% confidence level upper limit on the double-Λ hypernuclear angle-averaged direct production cross section for a single state vs. the negative of the total binding energy of the Λ's in that state. Background is not subtracted. The expected location of the ground state is indicated with an arrow (this scale is shifted relative to the excitation energy scale by +17 MeV).

of excitation energy [-80 MeV,-40 MeV] (see Figure 6.3). Since the flatness of the background was confirmed by loosening the cuts, an extrapolation can be made that the number of background events of the first kind in the excitation energy region [-20 MeV,0 MeV] is about 3. It can be concluded then that the background of the first kind contributes only a small fraction of the total signal in the Ξ hypernuclear production region and it is ignored when a comparison of the data and theory is done.

Background of the second kind is more difficult to estimate because the exact shape of the missing mass spectrum is not known. The measurement of the excitation energy already has experimental resolution resolution folded in. In the next subsection an attempt at estimating the background in the bound region is made by using an E>0 part of the measured excitation energy spectrum and folding in the experimental resolution. This will overestimate background because the resolution will be effectively folded twice – once during the measurement and another time by hand when doing the background estimate. Another way of estimating background

is using the excitation energy spectrum obtained in Monte Carlo (where only free Ξ^- production is simulated and therefore no events with E<0) and folding in the resolution. The result is shown in Figure 6.6. The data (dashed line) well agree with Monte Carlo in the E>0 region. There are only 8 events with E<0 and the corresponding 90% C.L. upper limit is 13. So using Monte Carlo simulation the background in the E<0 from free Ξ^- production part of the spectrum is estimated to be less than 13 events at 90% C.L.

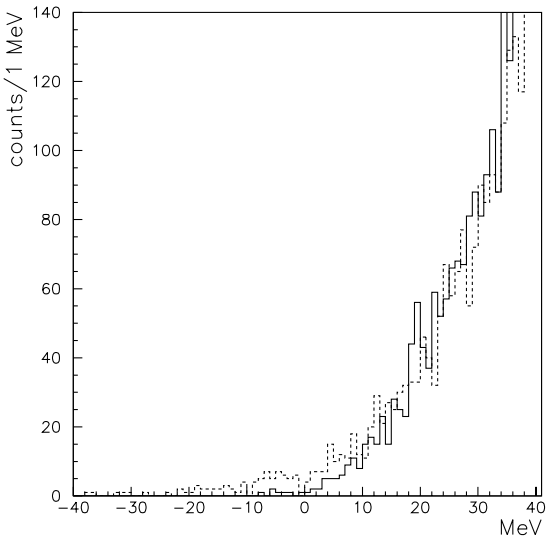

Figure 6.6: Excitation energy spectra as predicted by Monte Carlo (solid line) with the data overlayed on top (dashed line). The Monte Carlo shows only 8 events leaking to the region E<0.

One could also argue that the resolution function might have very long tails which are not easily detectable. But even if these tails had existed their magnitude would have to be very small (the existence of any significant resolution tails is ruled out by Figure 6.7); they would cause a flat-like (flat background from very long tails) kind of background and would not explain the structure that is seen in E885 in E<0 region. The intermediate case of long but still not very long tails of resolution function is treated below and shown not to explain the excess of events in the E<0 region even when absurdly large tails, contradicting the measurements, are added to the Gaussian resolution function.

6.7.1 Study of the effect of resolution tails on bound states

Figure 6.7 shows two fits of missing mass distribution for Ξ^- production on hydrogen. First it is fit with a single Gaussian. A fit with two Gaussians is also shown: the

first Gaussian with the width 3.8 MeV/c^2 r.m.s and the second Gaussian with the width of 10 MeV/c^2 r.m.s. The second fit represents the case of Gaussian resolution functions with non-Gaussian tails (tails are simulated by a wider Gaussian). Relative normalization of the two Gaussians in the second fit is 1:0.4. The two fits are used to test what effect non-Gaussian resolution tails would have on the missing mass spectrum. It must be noted that the fit with the two Gaussians is statistically much less favored relatively to the fit with the single Gaussian and is used for investigation purposes only and not as a working model.

Shown in Figure 6.8 is the excitation energy spectrum. Three rightmost lines represent the polynomial fit to the region of the spectrum above 0 folded with progressively worse resolution functions. The dashed line is for the case of perfect resolution, the dotted line for the case of Gaussian resolution function with the width equal to 6.1 MeV/c^2 and the dashed-dotted line for the case of the Gaussian resolution with non-Gaussian tails (simulated as the second wider Gaussian as discussed above). The widths of the Gaussians in the last case are 6.1 MeV/c^2 and 14.5 MeV/c^2 and relative normalization is 1:0.4. Due to the different kinematics in this case (carbon nucleus as the target as opposed to the proton) model resolution used for the hydrogen is scaled by a factor of 1.45, as discussed in Section 6.3. Clearly, the number of events leaking to the E<0 region is an overestimate since the resolution is folded twice. It can be seen that adding purposefully large non-Gaussian tails still does not account for the excess of events in the region E<0. The theoretical curves (solid line) for $V_{0\Xi}$ = 20 MeV (leftmost) and 16 MeV are also shown for comparison.

It can be concluded that:

- The measured resolution function can be reasonably approximated as being Gaussian.
- Adding tails to the Gaussian resolution function does not account for events below 0, even when the tails are taken to be quite long and large in magnitude.
- Severe tracking errors and particle misidentification would cause flat (over sufficiently small ≈100 MeV region) background and are excluded as potential source of the signal in the excitation energy region -20 MeV<E<0 MeV.

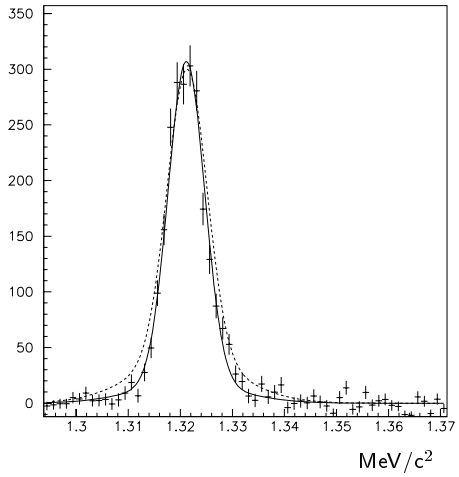

Figure 6.7: Two resolution functions that are used to study the influence of tails on the number of events in the bound region leaking from E>0. The distributions shows missing mass for Ξ^- production on hydrogen in CH_2 target. Background from reactions on carbon is subtracted using data sample taken with carbon target. The solid line shows the best Gaussian fit (3.8 MeV/c^2 r.m.s.). The dashed line shows the fit with two Gaussians: the first one having the width 3.8 MeV/c^2 and the second one the width 10 MeV/c^2 r.m.s.

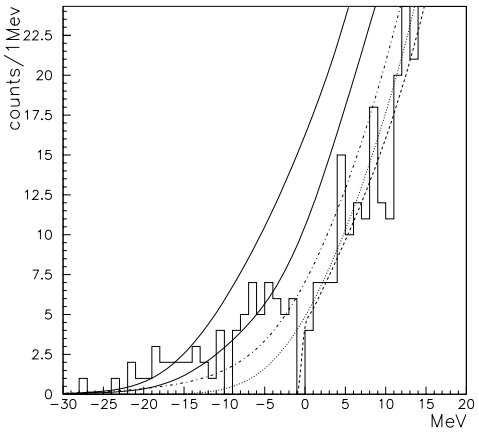

Figure 6.8: Excitation energy spectrum around E=0 for diamond target. Three rightmost lines represent a polynomial fit to the region of the spectrum E>0 folded with progressively worse resolution functions. The dashed line shows the fit itself. The other two lines represents two resolution functions as shown on the plot above: the dotted line shows the fit convoluted with the Gaussian resolution function without tails and the dashed-dotted line shows the fit convoluted with the "tailed" resolution function. The two solid lines show theoretical curves for $V_{0\,\Xi} = 20$ MeV (leftmost) and 16 MeV.

Chapter 7

Summary and Conclusions

A high statistics measurement of S=−2 hypernuclear production has been made using high intensity AGS D6 K^- beam line. Both direct production and production via Ξ^- capture on carbon modes have been measured. A total integrated flux of 8.0×10^{11} K^-'s has been accumulated. This chapter summarizes the analysis and presents conclusions that have been made.

7.1 Double-Λ hypernuclear production via Ξ^- capture on carbon

The high density diamond target and high integrated beam flux provided about 20 000 Ξ^- stops in the target. A stop, followed by Ξ^- capture by the carbon nucleus, can lead to a number of scenarios, one of which is a creation of a double-Λ hypernucleus after the conversion $\Xi^- + p \rightarrow \Lambda + \Lambda$ in the nucleus and emission of a neutron, which carries away the excess energy. Due to the two-body nature of such a reaction, the energy of the neutron would determine the energy of the hypernuclear state.

The Ξ^- stopping probability depends strongly on its initial energy, which in turn is strongly correlated with the missing mass in the (K^-,K^+) reaction. A cut study resulted in determining a missing mass cut value that maximized sensitivity to detection a mono-energetic neutron peak. After applying the missing mass cut, the neutron spectrum, shown in Figure 5.6, was searched for evidence of a peak. To find the number of neutrons in a hypothesized mono-energetic neutron peak for a particular neutron energy, the spectrum was fitted with a scaled background template and a Gaussian peak of known width. The fit procedure resulted in a 90% C. L. intervals on the branching ratio for the neutron-emission channel of double-Λ hypernuclear production $(\Xi^-, {}^{12}\mathrm{C})_{\mathrm{atom}} \rightarrow {}^{12}_{\Lambda\Lambda}\mathrm{B}^* + \mathrm{n}$. The confidence interval as a function of the neutron β^{-1} is shown in Figure 5.8. An arrow indicates the expected neutron energy with the following assumptions: a $(1s_\Lambda 1p_\Lambda)$ configuration is produced with excitation energy 10 MeV above the ground state energy and with corresponding Λ-Λ interaction energy $\Delta B_{\Lambda\Lambda} = 0$. The Λ-Λ interaction energy in the $(1s_\Lambda 1p_\Lambda)$ configuration should

be expected to be smaller than the value of 4 MeV–5 MeV which is currently assumed for the configuration ($1s_\Lambda 1s_\Lambda$) due to the smaller overlap of the Λs' wave functions. Therefore it is safe to assume that the real neutron energy should be within 4 MeV from the nominal value indicated with the arrow. From the plot, the upper limit on the branching ratio is $\approx$4% in the region $\pm$4 MeV around the arrow. It can be concluded that

- The neutron-emission channel of double-Λ hypernuclear production has a branching ratio at or below 4% at 90% confidence level.

7.2 Direct production of doubly-strange hypernuclei

7.2.1 Ξ hypernuclear production

The measurement of the missing mass allowed the determination of the energy of directly produced S=–2 systems, Ξ and double-Λ hypernuclei being particular examples of such system. It was convenient to plot excitation energy instead of missing mass, with the zero of excitation energy defined as the sum of the ^{11}B and Ξ^- masses. With this definition the Ξ hypernuclear states would map to the region just below zero of excitation energy and double-Λ hypernuclear states further down at $\approx$-40 MeV and upward. Due to the relative weakness of the signal of hypernuclear production and its proximity to the strong signal of free Ξ^- production, cut and resolution studies were of great importance. It was found that the main source of background came from the error in determination of the beam particle characteristics. This should be expected, taking into account the high intensity flux to which the detectors that measured the beam particles were exposed. Very tight cuts allowed the reduction of the background to a very low level, at the price of a reduction in the statistics by a factor of ≈ 5. The study of the acceptance for various reactions was needed in order to normalize the data to the known cross section of free Ξ^- production on hydrogen. The large volume of calibration data allowed the normalization of the differential cross section with only about 8% statistical error.

Since the resolution was not sufficient to observe hypernuclear states as discrete peaks, which would have allowed a direct inference of the hypernuclear binding energies, a method of comparison of the data and theoretical calculation, folded with experimental resolution, was used. The excitation spectra for two different values of cut-off angle θ of the K^+ are shown in Figure 6.3. A comparison of the data with the theoretical calculations for two values of Ξ-nucleus potential well depth $V_{0\,\Xi} = 16$ MeV and 20 MeV shows a good agreement of the data and theory for $V_{0\,\Xi} = 16$ MeV in the region of excitation energy -20 MeV<E<0 MeV and a significant disagreement between the data and theory for $V_{0\,\Xi} = 20$ MeV. The numbers of events in that region for the data and theory are summarized in Table 6.4. There is a disagreement

between the data and theory in the unbound region for both values of the potential, with a probable explanation that the theoretical prediction may be less reliable in the unbound region.

The accuracy of Distorted Wave Impulse Approximation (DWIA), which was used for the cross section calculation, was reported to be about 30% in the S=–1 sector (see discussion in Chapter 1). It can not be ruled out, however, that in our case the DWIA accuracy is worse due to the higher momentum transfer in E885. Therefore a value for the Ξ-nucleus potential well depth as high as 20 MeV, though less favored, can not be completely ruled out.

It was shown in Section 6.7 that the events in the bound region of excitation energy spectrum just below zero could not be explained by background or effects of limited resolution. It is most likely coming from production of Ξ hypernuclei. Another possible source of the signal in the bound region is production of ${}^{11}_{\Lambda}\mathrm{Be} + \Lambda$ (a ground state ${}^{11}_{\Lambda}\mathrm{Be}$ and a Λ in continuum). The threshold for the reaction is estimated to be at ≈-27 MeV and the spectrum is consistent with the threshold behavior for the reaction. The unavailability of cross section calculations for the process makes the estimation of its contribution impossible. It can be concluded that:

- There is a strong evidence of production of S=–2 systems in the bound region,
- The data is consistent with Ξ-hypernuclear existence and the $V_{0\,\Xi}$ potential depth being around 16 MeV,
- The agreement between the data and theory is significantly better for $V_{0\,\Xi} = 16$ MeV than for $V_{0\,\Xi} = 20$ MeV.

7.2.2 Double-Λ hypernuclear production

A. J. Baltz *et al.* [24] predicted the cross section of direct double-Λ production in the reaction ${}^{16}\mathrm{O}(\mathrm{K}^-,\mathrm{K}^+)^{16}_{\Lambda\Lambda}\mathrm{C}^*$ to be a few nb/sr (up to 9 nb/sr at zero degrees for population of $3^-(s_\Lambda p_\Lambda)$ state) for $p_{K^-} = 1.1$ GeV/c. Cross sections may be higher for the incident K^- momentum of 1.8 GeV/c, because 1.1 GeV/c is below threshold for Ξ^- production while 1.8 GeV/c is at the peak of the two-body Ξ^- production cross section [25]. C. B. Dover *et al.* [26] pointed out the possibility of Ξ and double-Λ hypernuclear states mixing which would introduce an amplitude for direct one-step double-Λ hypernuclear production and could result in much higher cross sections of direct double-Λ-hypernuclear production. The cross sections could be expected to be in excess of 10 nb/sr [25].

Attributing the signal below the Ξ hypernuclear production to direct double-Λ hypernuclear production allowed the setting of an upper limit on differential cross section of production of a double-Λ hypernuclear state. The upper limit as a function of the negative of the total binding energy of the two Λ's is shown in Figure 6.5.

- The differential cross section of direct double-Λ hypernuclei production, averaged over $\theta < 14^{\circ}$, is below ≈ 6.5 nb/sr for the ground state and below ≈ 10.2 nb/sr for a 10 MeV excitation at 90% confidence level.
- The use of theoretical calculation, if it becomes available, may result in a significantly better upper limit, because the contributions from the production of all hypernuclear states would be taken into account, as opposed to the current treatment where all the counts (within 2σ of resolution) are assumed to come from production of a single state.
- Our results rule out very high cross sections of direct double-Λ hypernuclear production which have been speculated to result from Ξ and double-Λ hypernuclear states mixing.

Appendix A

Statistics

A.1 Confidence intervals obtained using a new ordering principle

When calculating confidence intervals, a new unified ordering principle has the advantage of providing the desired coverage and avoiding the problem of non-physical upper limits [51]. In short, it is based on picking the points in the acceptance region $[x_1, x_2]$ in order of decreasing $R = P(x|\mu)/P(x|\mu_{best})$, where

- μ is the true value and x is the measured value,
- $P(x|\mu)$ is the probability density function of x, given the true value μ,
- μ_{best} is the physically allowed value of μ that maximizes $P(x|\mu)$.

The points are added to the acceptance region until the desired coverage is achieved: $\int_{x_1}^{x_2} P(x|\mu)dx = \alpha$, where α is the confidence level. x_1 and x_2 can be thought of as functions of μ. Once they are known, a confidence belt $\{x_1(\mu), x_2(\mu)\}$ can be constructed.

A.1.1 Simple example for the case of a Gaussian distribution

To define a prescription for mapping a measured quantity into a confidence interval for the true value, we start by considering the inverse problem, determining an acceptance region from a known true value μ. For example, consider finding the acceptance region $[x_1, x_2]$ for a Gaussian probability distribution function with $\mu = 1$, $\sigma = 1$ and $P(x|\mu) = (1/\sqrt{2\pi})e^{-(x-1)^2/2}$ for $\alpha = 90\%$. Also let μ be constrained to positive values. It is customary to pick the interval to be either symmetric about the value of x that maximizes $P(x|\mu)$ or one-sided with the upper boundary being $+\infty$. The former type of intervals are called central intervals and the latter type are called one-sided. If the latter choice is made, then the classical one-sided acceptance interval is $[x_1, +\infty]$ such that $\int_{x_1}^{+\infty} P(x|\mu)\, dx = \alpha$. This gives $[x_1, +\infty] = [\mu - 1.28\sigma, +\infty] = [-0.28, +\infty]$.

Now let us build the acceptance interval using the new ordering principle. First we note that $\mu_{best} = x$ for $x > 0$ and $\mu_{best} = 0$ for $x \leq 0$. Then $R(x) = \dfrac{P(x|\mu)}{P(x|\mu_{best})}$ is $e^{-(x-1)^2/2}$ for $x > 0$ and $e^{x-1/2}$ for $x \leq 0$. Now we need to find an interval $[x_1, x_2]$ such that $R(x_1) = R(x_2)$ and $\int_{x_1}^{x_2} P(x|\mu)\, dx = \alpha$. A numerical solution yields the interval $[-0.74, 2.57]$ that satisfies those conditions.

The intervals calculated using both methods are shown in Figure A.1. The set of intervals $[x_1(\mu), x_2(\mu)]$ are used to map a measured value to a confidence interval on μ. For any measured value x, $[\mu_1(x), \mu_2(x)]$ is defined as the set of values μ for which $x \in [x_1(\mu), x_2(\mu)]$.

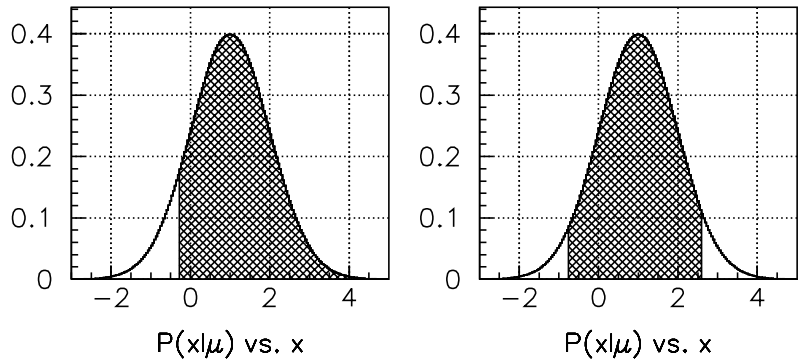

Figure A.1: 90% confidence level acceptance intervals for a Gaussian with the mean and sigma equal to 1. Shaded area on the left plot shows the classical one-sided acceptance interval. The plot on the right shows the acceptance interval obtained using the new unified ordering principle.

A.2 Application of the new ordering principle

In this section determination of 90% C. L. intervals on the branching ratio of the decay $(\Xi^-, {}^{12}\mathrm{C})_{\mathrm{atom}} \rightarrow {}^{12}_{\Lambda\Lambda}\mathrm{B}^* + \mathrm{n}$ for an arbitrarily chosen neutron energy corresponding to $\beta^{-1} = 5$ is demonstrated. The procedure has to be repeated for other neutron energies in order to obtain upper limits for a range of neutron energies.

The measured value here is the number of mono-energetic neutrons in a Gaussian peak, A_{fit}, which is obtained by fitting the neutron spectrum with a scaled background template and Gaussian peak. The mean of the peak is fixed at a particular β^{-1} and its width is derived in Monte Carlo calculations. The probability density function $P(A_{fit}|A_{true})$, where A_{true} is the true number of neutrons, is obtained in Monte Carlo calculations. It was found that $P(A_{fit}|A_{true})$ is a Gaussian distribution with the

mean equal to A_{true} and width weakly depending on A_{true}. Given $P(A_{fit}|A_{true})$, the ordering principle determines the 90% confidence interval $[A_1, A_2]$ with the property $\int_{A_1}^{A_2} P(A_{fit}|A_{true})dA_{fit} = 90\%$. Construction of the confidence belt is sufficient to produce the confidence interval for any measured value of neutrons in the peak A_{fit}.

The two parameters of the fit, the template scale factor and area under the peak ($\equiv$ number of mono-energetic neutrons) are found to be 0.206 and 12.7 respectively for $\beta^{-1} = 5$. The number of mono-energetic neutrons is used to read off the confidence interval from the confidence belt, as shown in Figure A.2. The number of neutrons is then converted to branching ratio. The plot on the right shows that even for a low negative fit value a non-empty interval is obtained if the new ordering principle is used. This results from the order in which the acceptance region for a given true value A_{true} is built (in the order of increasing R). For increasingly small A_{true} the left limit of the acceptance region goes to $-\infty$, which can be seen on the right plot in Figure A.2. The use of central intervals (left plot), however, results in obtaining null intervals for sufficiently low values of A_{fit}.

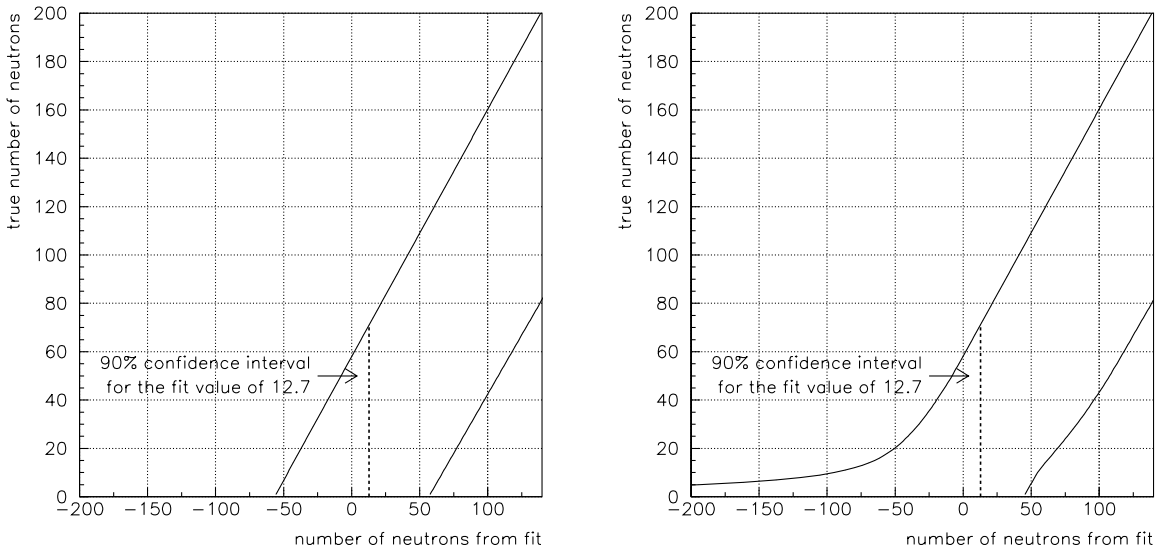

Figure A.2: Confidence belt for 90% confidence level for the number of mono-energetic neutrons with the energy corresponding to $\beta^{-1} = 5$. The left plot shows the case of using central intervals and the plot on the right shows the case of using the new ordering principle. The horizontal axis is the measured value A_{fit} and the vertical axis is the true value A_{true}. The fit value for $\beta^{-1} = 5$ is 12.7 and the corresponding 90% confidence level interval is shown by a vertical line segment. Non-empty intervals are obtained for any fit values if the new ordering principle is used.

Appendix B

Distorted Wave Impulse Approximation

A short description of DWIA follows. Notation and terminology from "Collision Theory" by M. Goldberger and K. Watson [52] is used.

Scattering matrix $\mathcal{T}$ is defined as

$$S_{fi} = \delta_{fi} - 2\pi i \delta(E_f - E_i)\mathcal{T}_{fi},$$

where S is the S-matrix. For an isolated system

$$\mathcal{T}_{fi} = \delta(P_f - P_i)T_{fi},$$

where T_{fi} is the T-matrix element. S-matrix elements are zero between the initial and final states that do not conserve momentum or energy. When the description of the interacting system involves an external potential, the system is not isolated and momentum is not conserved. Therefore the definition does not involve the momentum delta function and T and $\mathcal{T}$ can be used interchangeably. A common example of scattering with an external potential would be meson scattering off a bound nucleon. The external potential is provided by the nucleus, binding the nucleon to the nucleus. This is also the case when the 2-body scattering problem is reduced to the motion of center of mass and relative motion. For example, 2-body scattering with the potential depending on the relative coordinate (total momentum is conserved) can be reduced to the problem of 1-body scattering in an external potential (momentum of the scattered particle is not conserved).

Distorted Wave Impulse Approximation (DWIA), which is a combination of Distorted Wave Born Approximation (DWBA) and Impulse Approximation, may be used to estimate the matrix element. The following is a short description of the DWBA. It is sometimes the case that the potential can be decomposed into two parts $H = K + U + V$ and V can be treated perturbatively. If exact or approximate solutions for the part of the total Hamiltonian $K + U$ can be found, then it is possible to get an approximate expression for the T-matrix of the total Hamiltonian.

Let ψ_β^{T-} and ψ_α^+ be the Lippmann-Schwinger ingoing-wave and outgoing-wave type solutions for the partial Hamiltonians $K + U^*$ and $K + U$ respectively and ϕ_β be a plane wave. Subscripts α and β denote physical state. The outgoing-wave solution is asymptotically a superposition of a plane wave and outgoing spherical wave. Correspondingly, the ingoing-wave solution is asymptotically a superposition of a plane and ingoing spherical waves. Then $\mathcal{T}$-matrix for the total Hamiltonian is equal to:

$$\mathcal{T}_{fi} \equiv \langle f|\mathcal{T}|i\rangle \simeq \langle \phi_f|U|\psi_i^+\rangle + \langle \psi_f^{T-}|V|\psi_i^+\rangle,$$

Superscript T reflects the fact that the potential U for the ingoing-type solution is complex conjugated. The corresponding wave function is unphysical because the potential is a source of particles (unless U is real). The second term in the RHS is a correction, calculated as a T-matrix element between states distorted by the first potential. If U is chosen so that it does not cause transitions $i \to f$, then

$$\mathcal{T}_{fi} \simeq \langle \psi_f^{T-}|V|\psi_i^+\rangle$$

In our case, we choose the U to describe all elastic and inelastic processes on the nucleus except the Ξ^- production and V to describe Ξ hypernuclear production through an elementary process $K^- + p \to \Xi^- + K^+$ on protons in the nucleus. Then only V can connect the initial state to the final state of interest Ξ^- hypernucleus. We use the letter χ for the kaon distorted wave function and ψ for the many-particle wave function of the initial state and final states and approximating many-body operator $V = \sum_n V_n$, where V_n is a two-body operator converting a proton to a cascade and K^- to K^+. Also, V_n is approximated to be spin-independent. Separating baryon and kaon parts of the wave functions we can write:

$$\mathcal{T}_{fi} \simeq \langle \chi_f^{T-}\psi_f| \sum_n V_n|\chi_i^+\psi_i\rangle = \sum_n \langle \chi_f^{T-}\psi_f|V_n|\chi_i^+\psi_i\rangle$$

We can exploit the 2-body nature of the V_n to simplify the expression. Only one proton participates in the reaction and the rest of the nucleons are spectators. We should be able to reduce the many-body problem to a 2-body one. Let us specify the problem further. Protons in various nuclear shells can contribute to hypernuclear formation. We would like to calculate cross section of cascade hypernuclear formation off a proton in a closed (j,l) nuclear shell and we restrict ourselves to the case of doubly-closed shell nuclei. Since the shell is closed the initial state has angular momentum and parity $\mathrm{J}^\pi{=}0^+$. The final hadron state is a proton-hole cascade-particle excitation coupled to a total angular momentum (JJ_z), $[(jl)_N^{-1}(jl)_\Xi]_J$. We choose J to specify the final state because it is a good quantum number. The appearance of the proton hole in a sense is a combined effect of the rest of the protons in the (j,l) shell and we see that even though those protons are spectators they still affect the calculation because of the requirement of having definite total angular momentum. For the case of $\theta_{K^+} = 0^\circ$ there is no spin-flip, i.e. the cascade has the same spin orientation as the initial state proton. Also $J_z = 0$. We'll use the requirement of no spin-flip in our

calculation. Because of no spin-flip and initial $J^\pi = 0^+$ the final state will also have natural parity.

The operator V_n contains operators for proton destruction, cascade creation, K^- destruction and K^+ creation. In the impulse approximation V_n is replaced with V_n^{free}, a two-body operator in free space. Assuming that V_n is zero-range, i.e. the interaction happens in a point in space, and neglecting its momentum dependence, we can use a free-space T-matrix element for the elementary process. The above assumptions of zero-range and momentum independence mean that $\langle \mathbf{x_3}, \mathbf{x_4} | V_n^{free} | \mathbf{x_1}, \mathbf{x_2} \rangle = V_n^0 \delta(\mathbf{x_3} - \mathbf{x_1}) \delta(\mathbf{x_4} - \mathbf{x_2}) \delta(\mathbf{x_1} - \mathbf{x_2})$, where V_n^0 is a number. Further:

$$\begin{aligned} \langle \mathbf{k_3}, \mathbf{k_4} | \mathcal{T}_n^{free} | \mathbf{k_1}, \mathbf{k_2} \rangle &= \delta(\mathbf{k_3} + \mathbf{k_2} - \mathbf{k_1} - \mathbf{k_2}) \langle \mathbf{k_3}, \mathbf{k_4} | T_n^{free} | \mathbf{k_1}, \mathbf{k_2} \rangle \\ &= \langle \mathbf{k_3}, \mathbf{k_4} | V_n^{free} | \mathbf{k_1}+, \mathbf{k_2}+ \rangle \\ &\simeq \langle \mathbf{k_3}, \mathbf{k_4} | V_n^{free} | \mathbf{k_1}, \mathbf{k_2} \rangle, \end{aligned}$$

where $|\mathbf{k}+\rangle$ denotes the outgoing-wave type solution (plane plus outgoing scattered wave). In Born approximation $|\mathbf{k}+\rangle$ is replaced by a plane wave $|\mathbf{k}\rangle$ and $\langle \mathbf{k_3}, \mathbf{k_4} | V_n^{free} | \mathbf{k_1}, \mathbf{k_2} \rangle \simeq \langle \mathbf{k_3}, \mathbf{k_4} | \mathcal{T}_n^{free} | \mathbf{k_1}, \mathbf{k_2} \rangle$. Using coordinate space representation of the plane waves and the matrix element of V_n integration can be done and the result is a number, independent of the particles' momenta, multiplying momentum delta function: $V_n^0 \delta(\mathbf{k_3} + \mathbf{k_4} - \mathbf{k_1} - \mathbf{k_2})$, or

$$\langle \mathbf{k_3}, \mathbf{k_4} | T_n^{free} | \mathbf{k_1}, \mathbf{k_2} \rangle = V_n^0$$

Using $a^\dagger_{K^+}$, a_{K^-}, a_p and $a^\dagger_{\Xi^-{}^+}$ to designate creation and annihilation operators and writing them explicitly:

$$\mathcal{T}_{fi} \simeq \sum_n \langle \chi_f^{T-} \psi_f | V_n' a^\dagger_{K^+} a_{K^-} a^\dagger_{\Xi^-} p_n | \chi_i^+ \psi_i \rangle$$

Inserting completeness relations:

$$\sum_{spin} \int_{space} |\mathbf{x}_{K^+} \mathbf{x}_\Xi \ldots\rangle \langle \mathbf{x}_{K^+} \mathbf{x}_\Xi \ldots| = 1,$$
$$\sum_{spin} \int_{space} |\mathbf{x}'_{K^-} \mathbf{x}'_p \ldots\rangle \langle \mathbf{x}'_{K^-} \mathbf{x}'_p \ldots| = 1$$

and noting that V_n acts only on K^- and a single proton, all integrations and summations over all spins and other protons coordinates and spins are trivial and the only surviving integration are over coordinates space of the mesons and a proton and the cascade.

$$\mathcal{T}_{fi} \simeq \sum_n \langle \chi_f^{T-} \psi_f | V_n | \chi_i^+ \psi_i \rangle$$

$$
\begin{aligned}
&= \sum_n \int dx^3_{K^+} dx^3_{K^-} dx^3_\Xi dx^3_p \langle \chi_f^{T-} \psi_f | \mathbf{x}_{K^+} \mathbf{x}_\Xi \rangle \langle \mathbf{x}_{K^+} \mathbf{x}_\Xi | V_n | \mathbf{x}_{K^-} \mathbf{x}_p^n \rangle \langle \mathbf{x}_{K^-} \mathbf{x}_p | \chi_i^+ \psi_i \rangle \\
&= V_n^0 \sum_n \int dx^3 \langle \chi^{T-} | \mathbf{x} \rangle \langle \mathbf{x} | \chi^+ \rangle \langle \psi_f | K^n(\mathbf{x}) | \psi_i \rangle \\
&= \langle \mathbf{k}_{K^+}, \mathbf{k}_\Xi | T^{free} | \mathbf{k}_{K^-}, \mathbf{k}_p \rangle \sum_n \int dx^3 \langle \chi^{T-} | \mathbf{x} \rangle \langle \mathbf{x} | \chi^+ \rangle \langle \psi_f | K^n(\mathbf{x}) | \psi_i \rangle,
\end{aligned}
$$

where $K^n(\mathbf{x})$ is an operator with the matrix element $\langle \mathbf{x}_\Xi | K(\mathbf{x}) | \mathbf{x}_p \rangle = \delta(\mathbf{x} - \mathbf{x}_p)\delta(\mathbf{x} - \mathbf{x}_\Xi)$. The K($\mathbf{x}$) operator destroys a proton at $\mathbf{x}$ and creates a cascade at $\mathbf{x}$. The T-matrix element of the elementary process in free space is factored out. The last expression can be rewritten as

$$
\mathcal{T}_{fi} = \langle \mathbf{k}_{K^+}, \mathbf{k}_\Xi | T^{free} | \mathbf{k}_{K^-}, \mathbf{k}_p \rangle \langle \psi_f | \int dx^3 \langle \chi^{T-} | \mathbf{x} \rangle \langle \mathbf{x} | \chi^+ \rangle \sum_n K^n(\mathbf{x}) | \psi_i \rangle
$$

The meson waves can be calculated using eikonal approximation and optical potential. The optical potential is derived from the total cross section for $K^- + p \to$ *anything*. The product of meson distorted wave is written [52] as

$$
\langle \chi^{T-} | \mathbf{x} \rangle \langle \mathbf{x} | \chi^+ \rangle \approx e^{i\mathbf{Q}\cdot\mathbf{x} - (\sigma/2)T(b)},
$$

where $\mathbf{Q} = \mathbf{p}_{K^+} - \mathbf{p}_{K^-}$ and $e^{-(\sigma/2)T(b)}$ is the term describing absorption of the mesons inside the nucleus (see [52] for details on the eikonal approximation and what σ and $T(b)$ are).

Assuming that the $\mathcal{T}^{free}$-matrix element varies slowly it can be moved out of the integration with asymptotic values as its parameters:

$$
\begin{aligned}
\mathcal{T}_{fi} &\simeq \langle \mathbf{k}_f | T^{free} | \mathbf{k}_i \rangle \sum_n \int d^3k_1 d^3k_2 d^3k_3 d^3\mathbf{k}_4 \chi_f^{T-*}(\mathbf{k}_4) \psi_f^{n*}(\mathbf{k}_3) \\
&\times \delta(\mathbf{k}_4 + \mathbf{k}_3 - \mathbf{k}_2 - \mathbf{k}_1) \chi_i^+(\mathbf{k}_2) \psi_i^n(\mathbf{k}_1) \\
&= \langle \mathbf{k}_f | T^{free} | \mathbf{k}_i \rangle \sum_n \int d^3x \chi_f^{T-*}(\mathbf{x}) \psi_f^{n*}(\mathbf{x}) \chi_i^+(\mathbf{x}) \psi_i^n(\mathbf{x}),
\end{aligned}
$$

where subscripts i and f denote all the remaining quantum numbers and the summation is done over target particles.

Skipping intermediate calculation, the result for differential hypernuclear cross section is [31]:

$$
\left(\frac{d\sigma(0^\circ)}{d\Omega} \right)_{0^+ \to J^\pi} = \alpha \left(\frac{d\sigma(0^\circ)}{d\Omega} \right)_{K^- p \to K^+ \Xi^-} Z^J_{eff},
$$

where $\left(\frac{d\sigma(0^\circ)}{d\Omega} \right)_{K^- p \to K^+ \Xi^-}$ is the elementary cross section of cascade production on hydrogen for zero scattering angle, α is a kinematical factor arising from the transformation of T-matrices from the two-body to many-body lab system [52] and Z_{eff}

is the effective proton number:

$$Z_{eff} = (2J+1)(2j_\Xi+1)(2j_p+1) \begin{pmatrix} j_\Xi & j_p & J \\ \frac{1}{2} & -\frac{1}{2} & 0 \end{pmatrix} F(Q).$$

The factor

$$(2J+1)(2j_\Xi+1)(2j_p+1) \begin{pmatrix} j_\Xi & j_p & J \\ \frac{1}{2} & -\frac{1}{2} & 0 \end{pmatrix}$$

(the rightmost quantity in parentheses is a 3-j symbol) represents the angular momentum coupling of the proton hole and cascade to the state with the total momentum J and momentum projection $J_z = 0$ and the form factor $F(Q)$ is given by

$$F(Q) = \left(\int_0^\infty dr\, r^2\, R_\Xi(r)\, R_p(r)\, \tilde{j}(Qr) \right)^2,$$

where $R_\Xi(r)$ and $R_p(r)$ are the radial parts of the cascade and target proton wave functions and $\tilde{j}(Qr)$ is the $L = J$ component of the product of the meson distorted waves [53]:

$$\chi_f^{T-*}(\mathbf{x})\, \chi_i^+(\mathbf{x}) = \sum_{L=0}^{\infty} \sqrt{4\pi(2L+1)}\, i^L \tilde{j}_L(r)\, Y_L^0(\hat{\mathbf{x}}).$$

Appendix C

The bin content of selected histograms

The bin content of selected histograms in the main text are reported in this chapter in the form of tables. Each table caption provides a reference to the figure in the main text and a short description of the histogram.

bins 1–28	bins 29–56	bins 57–84	bins 85–112	bins 113–140	bins 141–168	bins 169–196	bins 197–224	bins 225–252	bins 253–280	bins 281–308	bins 309–336	bins 337–364	bins 365–392	bins 393–420	bins 421–448	bins 449–471
78	134	103	86	78	64	47	33	52	25	22	24	22	18	15	15	2
86	136	95	92	55	52	41	54	37	31	37	26	18	15	16	11	9
82	129	125	83	66	59	48	40	38	30	28	26	21	11	12	8	10
74	155	101	106	62	56	46	40	42	39	34	21	20	14	14	11	7
76	108	107	91	79	62	44	44	30	42	25	35	19	18	10	7	9
99	133	115	71	61	48	58	45	44	43	30	26	13	24	11	10	20
85	132	97	88	52	50	47	47	33	32	23	25	20	14	11	10	12
71	127	101	87	76	65	49	40	35	36	32	22	25	15	14	20	8
96	122	100	81	66	52	57	37	42	34	25	22	13	24	12	11	13
87	120	111	86	74	37	41	58	49	35	36	26	27	14	10	11	8
90	139	95	103	73	47	51	43	41	43	37	34	20	13	20	7	10
94	121	108	88	64	47	37	39	39	30	27	25	22	25	15	11	8
88	117	86	76	63	51	60	47	33	40	24	20	21	14	13	9	11
102	122	107	82	58	46	44	45	47	31	28	19	18	17	18	9	9
103	128	103	70	56	49	58	34	35	38	25	18	19	16	10	7	9
105	120	80	67	63	64	49	43	35	36	30	25	19	18	11	12	7
126	119	105	63	66	58	31	42	33	32	20	24	18	20	9	14	16
113	114	101	67	69	49	47	43	26	34	34	36	24	15	8	11	10
131	113	94	75	60	57	46	46	49	32	34	19	16	13	7	7	14
109	146	106	66	55	48	46	35	30	25	29	21	10	15	13	4	6
116	105	108	86	50	30	47	41	42	31	27	20	19	11	9	16	10
118	106	87	67	63	46	49	31	28	26	25	16	22	22	10	6	11
125	114	102	82	57	58	46	40	27	32	31	20	15	18	17	11	13
121	118	107	70	50	53	49	41	41	32	30	23	25	18	13	7	
115	109	95	79	49	49	42	42	31	28	26	17	15	13	14	10	
116	109	84	70	65	49	39	36	39	38	26	24	24	17	9	12	
138	105	88	72	52	37	48	39	36	34	26	21	12	11	8	13	
141	112	88	66	62	51	44	41	40	32	23	24	17	7	13	7	

Table C.1: The bin content of the neutron spectrum histogram for the events with likely Ξ^- stop, shown in Figure 5.6. The histogram has 471 bins with the lower and upper edges of 2.25 and 14 respectively.

bins 1–28	bins 29–56	bins 57–84	bins 85–112	bins 113–140	bins 141–168	bins 169–196	bins 197–224	bins 225–252	bins 253–280	bins 281–308	bins 309–336	bins 337–364	bins 365–392	bins 393–420	bins 421–448	bins 449–471
383	609	576	439	298	251	246	213	201	161	144	145	117	89	58	69	52
395	570	515	421	317	262	239	217	169	167	164	128	107	99	72	76	52
421	577	557	416	314	281	236	215	192	180	148	117	90	102	62	49	51
425	641	523	415	312	277	227	200	164	171	156	136	106	88	64	51	50
449	604	564	394	325	245	244	209	183	148	147	143	98	87	80	54	55
409	588	521	466	328	268	249	206	188	163	143	142	96	74	71	60	48
433	613	532	417	326	278	221	207	196	171	146	125	89	89	68	65	55
420	642	504	427	310	266	242	206	194	144	135	126	126	104	88	58	47
462	612	532	416	297	226	233	201	216	179	141	123	110	81	62	58	54
484	604	499	377	312	256	227	167	190	167	147	123	87	78	60	70	45
514	650	505	422	294	254	221	209	179	174	151	120	101	88	72	46	46
461	656	504	427	310	250	231	199	186	150	138	127	102	82	65	73	61
514	610	462	400	298	262	224	210	181	173	139	107	92	68	74	49	56
501	607	475	384	280	251	227	205	193	153	140	104	124	66	70	59	37
506	595	468	423	308	232	225	211	178	177	152	109	104	85	82	69	35
553	617	468	336	314	241	221	174	180	153	129	121	87	77	73	39	48
546	556	472	406	271	270	225	194	182	160	137	138	106	87	74	72	53
540	597	450	364	299	241	234	218	176	152	139	114	96	79	62	64	49
590	595	439	304	272	264	220	183	182	157	122	120	115	58	63	58	41
533	613	443	360	265	259	222	195	156	151	147	107	98	77	70	56	49
581	599	461	373	280	268	206	185	165	142	146	116	94	79	54	44	44
563	584	465	368	296	214	226	192	173	171	146	120	95	69	67	49	37
566	591	442	350	281	229	219	174	175	160	132	109	96	75	59	41	52
592	530	436	337	280	246	203	176	182	168	135	114	90	65	59	45	
609	536	465	370	288	234	224	170	199	136	131	130	100	90	55	59	
583	577	464	337	274	220	196	182	167	162	119	100	83	83	41	53	
598	576	427	358	284	241	236	203	180	159	120	134	95	68	50	56	
588	527	418	324	276	273	181	203	180	143	113	109	85	63	60	59	

Table C.2: The bin content of the neutron spectrum histogram for the events with unlikely Ξ^- stop, shown in Figure 5.5. The histogram has 471 bins with the lower and upper edges of 2.225 and 14 respectively.

bins 1–28	bins 29–56	bins 57–84	bins 85–112	bins 113–140	bins 141–168	bins 169–196	bins 197–224	bins 225–252	bins 253–280	bins 281–308	bins 309–336	bins 337–364	bins 365–392	bins 393–420	bins 421–448	bins 449–476	bins 477–504	bins 505–532	bins 533–560
48	112	933	441	782	721	583	448	354	327	272	242	238	212	182	147	123	91	80	60
56	124	921	458	786	704	614	479	374	311	293	234	246	174	170	155	121	113	76	75
34	147	910	434	766	745	584	443	370	294	261	237	228	216	158	133	113	108	54	70
40	209	873	460	802	741	550	467	358	304	308	259	238	211	158	163	114	87	61	76
29	292	872	480	796	701	548	432	363	351	252	267	232	192	151	142	117	78	79	71
49	419	793	489	811	730	567	413	347	319	266	281	206	177	180	149	115	80	91	56
51	656	761	515	781	671	559	406	340	303	288	216	210	213	166	135	121	90	92	68
35	1012	752	547	782	741	543	405	367	309	277	243	232	195	160	122	121	79	62	66
37	1531	669	530	859	680	571	410	358	299	264	230	228	201	172	135	108	89	72	60
49	2247	708	566	777	728	523	434	339	313	267	232	211	189	195	130	112	97	69	71
53	2872	671	542	775	683	580	417	347	331	270	248	220	185	181	119	101	86	75	72
52	3386	659	555	804	686	552	412	352	296	274	246	215	180	156	119	114	88	80	73
55	3591	673	534	832	657	558	425	358	309	276	244	199	190	160	160	127	110	84	61
47	3647	619	606	794	680	540	402	311	314	260	276	229	170	158	135	118	82	73	73
44	3552	613	616	792	653	500	422	327	300	245	253	219	194	163	126	101	76	90	56
44	3144	616	650	848	651	573	396	328	293	269	236	241	201	164	134	110	99	58	60
38	2850	547	616	851	671	555	398	319	294	253	242	198	173	164	134	110	89	91	74
52	2454	561	664	792	604	518	389	330	304	274	236	227	180	142	125	93	93	63	74
52	2222	521	651	815	647	512	375	323	297	272	255	199	184	137	148	91	93	78	53
58	1920	505	659	786	624	524	388	304	302	262	232	227	184	146	133	106	99	89	47
62	1700	542	702	800	613	448	410	327	300	246	235	212	173	158	113	99	87	58	59
48	1556	488	728	726	632	508	374	354	274	261	242	212	171	176	131	112	89	95	76
46	1408	508	710	777	598	480	401	322	305	271	219	210	189	159	130	98	76	83	66
54	1258	485	776	772	592	414	359	341	292	258	243	209	171	149	142	77	75	70	58
64	1163	512	699	819	606	460	346	329	287	246	200	186	195	138	116	99	88	68	55
50	1131	469	753	761	625	497	362	321	275	244	231	192	186	145	120	97	70	67	58
83	1035	518	736	760	592	466	389	294	292	238	226	210	194	144	122	97	84	60	51
86	977	429	737	756	597	471	365	327	284	227	222	208	176	136	119	101	79	57	67

Table C.3: The bin content of the neutron spectrum histogram for all events, shown in Figure 5.1. The histogram has 560 bins with the lower and upper edges of 0 and 14 respectively.

bins 1–28	bins 29–56	bins 57–84	bins 85–112	bins 113–140	bins 141–168	bins 169–196	bins 197–224	bins 225–252	bins 253–280	bins 281–308	bins 309–336	bins 337–364	bins 365–378
-58.8	50.2	-45.9	49.4	27.5	-5.7	23.2	28.8	21.3	33.8	1.5	-17.9	-52.9	-11.5
-72.2	40.6	-45.7	49.5	31.6	-10.0	27.5	29.2	20.5	35.2	1.6	-20.2	-52.1	-10.2
-82.8	32.9	-45.7	47.1	34.9	-13.7	31.1	29.2	19.4	36.1	1.8	-22.5	-51.2	-9.0
-89.9	26.4	-45.3	41.7	37.1	-16.3	34.1	28.8	17.9	36.4	2.0	-24.9	-50.2	-7.9
-93.7	20.7	-44.1	33.6	37.9	-17.9	36.4	28.1	16.1	36.3	2.2	-27.3	-49.2	-7.1
-92.8	15.3	-41.8	23.1	37.3	-18.4	37.9	27.1	14.1	35.7	2.4	-29.8	-48.2	-6.4
-85.1	10.3	-37.8	11.1	35.4	-18.2	38.8	25.8	11.9	34.7	2.6	-32.2	-47.0	-5.9
-69.8	5.7	-31.6	-1.1	32.3	-17.4	39.0	24.2	9.6	33.2	2.8	-34.7	-45.9	-5.6
-48.6	1.6	-23.2	-12.1	28.3	-16.4	38.7	22.5	7.4	31.4	2.9	-37.1	-44.7	-5.4
-25.8	-1.8	-12.8	-20.3	23.7	-15.5	37.9	20.8	5.3	29.3	3.0	-39.4	-43.4	-5.4
-6.6	-5.1	-1.2	-24.7	18.9	-14.9	36.7	19.1	3.3	27.1	2.9	-41.7	-42.1	-5.6
5.6	-8.7	10.6	-24.8	14.2	-14.7	35.3	17.5	1.8	24.6	2.8	-43.8	-40.7	-6.0
10.0	-13.6	21.4	-21.2	10.0	-14.9	33.6	16.2	0.6	22.1	2.6	-45.8	-39.3	-6.5
8.8	-19.9	30.2	-15.1	6.5	-15.4	31.9	15.2	0.0	19.6	2.2	-47.6	-37.8	-7.1
5.5	-27.7	36.3	-7.7	4.1	-16.1	30.2	14.4	-0.2	17.2	1.8	-49.3	-36.2	
3.4	-36.3	39.4	-0.4	3.0	-16.8	28.5	14.1	0.3	14.8	1.2	-50.8	-34.6	
4.9	-45.0	39.8	5.9	3.0	-17.3	27.0	14.1	1.4	12.6	0.5	-52.1	-32.9	
11.8	-52.9	38.2	10.5	4.2	-17.3	25.8	14.4	3.0	10.6	-0.3	-53.2	-31.1	
25.3	-59.3	35.5	13.2	6.1	-16.8	24.8	15.0	5.2	8.8	-1.3	-54.0	-29.3	
44.1	-63.8	32.6	14.1	8.5	-15.5	24.2	15.8	7.7	7.2	-2.4	-54.7	-27.4	
64.5	-66.0	30.5	13.7	10.6	-13.4	23.8	16.8	10.7	5.8	-3.6	-55.2	-25.5	
82.4	-65.7	29.7	12.7	12.2	-10.5	23.9	17.9	13.9	4.6	-5.0	-55.5	-23.6	
94.4	-63.2	30.4	11.9	12.8	-6.7	24.2	19.0	17.2	3.6	-6.4	-55.5	-21.7	
98.7	-59.2	32.6	11.8	12.3	-2.3	24.8	19.9	20.5	2.9	-8.1	-55.4	-19.9	
95.4	-54.8	35.8	12.9	10.4	2.7	25.6	20.8	23.8	2.3	-9.8	-55.2	-18.0	
86.4	-50.9	39.7	15.2	7.4	7.9	26.5	21.4	26.8	1.9	-11.7	-54.8	-16.3	
74.4	-48.1	43.7	18.8	3.4	13.2	27.4	21.7	29.5	1.7	-13.6	-54.3	-14.6	
61.8	-46.5	47.2	23.0	-1.1	18.4	28.2	21.7	31.9	1.5	-15.7	-53.6	-13.0	

Table C.4: The bin content of the histogram of the best fit value for the number of neutrons, shown as a dashed line in Figure 5.7. The histogram has 378 bins with the lower and upper edges of 2.375 and 11.825 respectively.

bins 1–28	bins 29–56	bins 57–84	bins 85–112	bins 113–140	bins 141–168	bins 169–196	bins 197–224	bins 225–252	bins 253–280	bins 281–308	bins 309–336	bins 337–364	bins 365–378
0.0	3.8	0.0	0.3	0.0	0.0	0.0	0.0	0.0	0.0	0.0	0.0	0.0	0.0
0.0	0.0	0.0	1.8	0.0	0.0	0.0	0.0	0.0	0.0	0.0	0.0	0.0	0.0
0.0	0.0	0.0	0.0	0.0	0.0	0.0	0.0	0.0	0.0	0.0	0.0	0.0	0.0
0.0	0.0	0.0	0.0	0.0	0.0	0.0	0.0	0.0	0.0	0.0	0.0	0.0	0.0
0.0	0.0	0.0	0.0	0.0	0.0	0.0	0.0	0.0	0.0	0.0	0.0	0.0	0.0
0.0	0.0	0.0	0.0	0.0	0.0	0.0	0.0	0.0	0.0	0.0	0.0	0.0	0.0
0.0	0.0	0.0	0.0	0.0	0.0	0.0	0.0	0.0	0.0	0.0	0.0	0.0	0.0
0.0	0.0	0.0	0.0	0.0	0.0	0.0	0.0	0.0	0.0	0.0	0.0	0.0	0.0
0.0	0.0	0.0	0.0	0.0	0.0	0.0	0.0	0.0	0.0	0.0	0.0	0.0	0.0
0.0	0.0	0.0	0.0	0.0	0.0	0.0	0.0	0.0	0.0	0.0	0.0	0.0	0.0
0.0	0.0	0.0	0.0	0.0	0.0	0.0	0.0	0.0	0.0	0.0	0.0	0.0	0.0
0.0	0.0	0.0	0.0	0.0	0.0	0.0	0.0	0.0	0.0	0.0	0.0	0.0	0.0
0.0	0.0	0.0	0.0	0.0	0.0	0.0	0.0	0.0	0.0	0.0	0.0	0.0	0.0
0.0	0.0	0.0	0.0	0.0	0.0	0.0	0.0	0.0	0.0	0.0	0.0	0.0	0.0
0.0	0.0	0.0	0.0	0.0	0.0	0.0	0.0	0.0	0.0	0.0	0.0	0.0	
0.0	0.0	0.0	0.0	0.0	0.0	0.0	0.0	0.0	0.0	0.0	0.0	0.0	
0.0	0.0	0.0	0.0	0.0	0.0	0.0	0.0	0.0	0.0	0.0	0.0	0.0	
0.0	0.0	0.0	0.0	0.0	0.0	0.0	0.0	0.0	0.0	0.0	0.0	0.0	
0.0	0.0	0.0	0.0	0.0	0.0	0.0	0.0	0.0	0.0	0.0	0.0	0.0	
0.0	0.0	0.0	0.0	0.0	0.0	0.0	0.0	0.0	0.0	0.0	0.0	0.0	
17.0	0.0	0.0	0.0	0.0	0.0	0.0	0.0	0.0	0.0	0.0	0.0	0.0	
28.8	0.0	0.0	0.0	0.0	0.0	0.0	0.0	0.0	0.0	0.0	0.0	0.0	
37.9	0.0	0.0	0.0	0.0	0.0	0.0	0.0	0.0	0.0	0.0	0.0	0.0	
40.7	0.0	0.0	0.0	0.0	0.0	0.0	0.0	0.0	0.0	0.0	0.0	0.0	
37.7	0.0	0.0	0.0	0.0	0.0	0.0	0.0	0.0	0.0	0.0	0.0	0.0	
30.8	0.0	0.0	0.0	0.0	0.0	0.0	0.0	0.0	0.0	0.0	0.0	0.0	
21.2	0.0	0.0	0.0	0.0	0.0	0.0	0.0	0.0	0.0	0.0	0.0	0.0	
13.9	0.0	0.0	0.0	0.0	0.0	0.0	0.0	0.0	0.0	0.0	0.0	0.0	

Table C.5: The bin content of the histogram of the lower limit on the number of neutrons, shown as the lower edge of a dashed band in Figure 5.7. The histogram has 378 bins with the lower and upper edges of 2.375 and 11.825 respectively.

bins 1–28	bins 29–56	bins 57–84	bins 85–112	bins 113–140	bins 141–168	bins 169–196	bins 197–224	bins 225–252	bins 253–280	bins 281–308	bins 309–336	bins 337–364	bins 365–378
8.2	111.7	25.3	111.2	84.4	49.1	79.5	86.6	79.6	91.5	57.5	37.6	14.7	37.8
7.6	101.3	26.8	111.1	88.6	45.6	83.0	86.6	78.5	93.9	58.6	35.3	14.5	38.4
6.4	93.3	26.7	108.2	92.9	42.5	87.2	86.4	77.7	93.2	57.1	33.6	14.4	39.9
6.7	87.7	26.5	104.0	94.8	39.1	90.1	85.1	75.8	94.3	59.0	31.2	16.0	39.1
6.8	82.6	28.0	94.5	94.2	38.2	93.8	85.1	75.0	93.1	58.9	30.8	14.0	40.5
6.3	76.2	28.9	83.5	93.1	37.1	95.9	84.6	71.4	93.6	58.8	29.0	15.2	42.0
7.5	71.5	30.2	71.3	92.9	38.6	95.1	83.8	69.7	92.5	58.7	26.7	16.9	41.3
9.3	67.9	35.4	58.4	88.0	40.0	95.1	81.2	66.0	91.9	58.2	24.5	16.5	41.4
15.5	63.6	42.9	47.5	86.0	40.8	95.6	79.4	65.7	88.1	58.2	23.8	16.1	42.9
29.8	59.4	51.8	40.8	80.9	42.0	94.1	79.0	62.2	86.3	58.1	21.1	17.7	41.4
45.4	56.6	61.1	36.7	74.2	41.7	93.3	76.4	62.0	84.3	58.3	20.3	17.1	40.2
58.2	53.4	74.7	35.1	70.5	41.7	92.9	75.7	58.0	81.1	58.3	19.6	18.5	40.0
63.5	48.0	85.6	38.2	65.1	41.5	90.5	73.3	57.0	79.9	57.1	18.6	18.0	40.8
62.2	45.0	94.7	44.8	62.9	40.1	88.8	72.3	56.1	76.4	57.2	17.2	19.5	39.8
59.3	37.7	100.2	50.7	59.6	40.6	87.9	71.2	57.9	74.6	57.7	16.2	20.4	
58.6	31.6	103.2	57.5	58.6	39.5	85.8	71.3	57.7	71.1	56.6	16.9	21.6	
59.2	25.4	103.3	63.3	58.8	39.5	83.1	71.9	58.3	69.6	55.1	15.2	22.5	
67.3	21.2	101.5	68.9	59.5	38.2	82.4	72.8	60.6	67.5	54.1	15.9	23.9	
82.7	19.7	98.0	71.3	61.6	39.1	81.2	72.8	62.3	65.8	54.9	14.2	24.9	
101.2	17.0	95.4	71.3	64.4	42.0	80.1	73.6	65.8	63.2	52.5	14.5	25.6	
122.0	17.8	93.1	71.8	66.6	42.6	80.7	74.5	68.8	63.0	50.0	13.1	26.3	
142.6	17.7	92.2	70.7	67.2	44.3	80.3	75.6	71.2	60.4	49.2	13.1	27.2	
154.8	18.6	93.8	69.9	68.3	48.4	81.8	76.4	74.6	59.4	48.5	13.1	29.4	
159.7	20.7	95.9	68.0	67.1	53.6	81.2	78.7	78.8	59.9	48.0	13.3	30.2	
156.6	21.4	98.1	70.7	65.2	58.7	82.2	78.5	81.4	58.0	45.9	14.9	31.2	
147.1	23.6	102.5	72.5	63.8	63.5	84.9	78.2	84.5	59.0	43.9	13.4	33.4	
135.8	24.3	106.8	77.0	58.3	69.3	84.2	79.3	87.6	58.9	41.6	14.9	34.6	
122.8	25.6	109.5	80.9	53.1	74.3	85.4	79.3	89.3	57.3	39.1	14.6	35.0	

Table C.6: The bin content of the histogram of the upper limit on the number of neutrons, shown as the upper edge of a dashed band in Figure 5.7. The histogram has 378 bins with the lower and upper edges of 2.375 and 11.825 respectively.

bins 1–28	bins 29–56	bins 57–84	bins 85–112	bins 113–140	bins 141–168	bins 169–196	bins 197–224	bins 225–252	bins 253–280	bins 281–308	bins 309–336	bins 337–364	bins 365–378
-5.2	3.4	-2.5	2.5	1.6	-0.3	1.1	1.4	1.0	1.8	0.1	-1.4	-5.5	-1.9
-6.4	2.7	-2.5	2.5	1.9	-0.6	1.3	1.4	1.0	1.8	0.1	-1.5	-5.5	-1.7
-7.3	2.2	-2.5	2.4	2.0	-0.7	1.5	1.4	0.9	1.9	0.1	-1.7	-5.4	-1.5
-7.9	1.7	-2.4	2.1	2.2	-0.9	1.7	1.3	0.8	1.9	0.1	-1.9	-5.4	-1.4
-8.2	1.3	-2.4	1.7	2.2	-1.0	1.8	1.3	0.8	1.9	0.1	-2.1	-5.4	-1.3
-8.0	1.0	-2.2	1.2	2.2	-1.0	1.8	1.3	0.7	1.9	0.2	-2.4	-5.3	-1.2
-7.3	0.7	-2.0	0.6	2.1	-1.0	1.9	1.2	0.6	1.8	0.2	-2.6	-5.3	-1.1
-6.0	0.4	-1.7	-0.1	1.9	-0.9	1.9	1.1	0.5	1.8	0.2	-2.8	-5.2	-1.1
-4.1	0.1	-1.2	-0.6	1.7	-0.9	1.9	1.0	0.4	1.7	0.2	-3.0	-5.2	-1.1
-2.2	-0.1	-0.7	-1.1	1.4	-0.8	1.8	1.0	0.3	1.6	0.2	-3.3	-5.1	-1.1
-0.5	-0.3	-0.1	-1.3	1.1	-0.8	1.8	0.9	0.2	1.5	0.2	-3.5	-5.0	-1.2
0.5	-0.5	0.5	-1.3	0.8	-0.8	1.7	0.8	0.1	1.3	0.2	-3.7	-4.9	-1.3
0.8	-0.8	1.1	-1.1	0.6	-0.8	1.6	0.8	0.0	1.2	0.2	-3.9	-4.8	-1.4
0.7	-1.2	1.5	-0.8	0.4	-0.8	1.5	0.7	0.0	1.1	0.1	-4.1	-4.7	-1.6
0.4	-1.7	1.9	-0.4	0.2	-0.8	1.4	0.7	0.0	0.9	0.1	-4.3	-4.6	
0.3	-2.2	2.0	0.0	0.2	-0.9	1.4	0.7	0.0	0.8	0.1	-4.5	-4.5	
0.4	-2.7	2.0	0.3	0.2	-0.9	1.3	0.7	0.1	0.7	0.0	-4.7	-4.3	
0.9	-3.1	1.9	0.6	0.2	-0.9	1.2	0.7	0.1	0.6	0.0	-4.8	-4.2	
1.9	-3.5	1.8	0.7	0.4	-0.9	1.2	0.7	0.3	0.5	-0.1	-4.9	-4.0	
3.3	-3.7	1.6	0.8	0.5	-0.8	1.1	0.7	0.4	0.4	-0.2	-5.1	-3.8	
4.8	-3.8	1.5	0.8	0.6	-0.7	1.1	0.8	0.5	0.3	-0.3	-5.2	-3.6	
6.1	-3.8	1.5	0.7	0.7	-0.5	1.1	0.8	0.7	0.3	-0.4	-5.3	-3.4	
6.9	-3.6	1.5	0.7	0.7	-0.3	1.1	0.9	0.9	0.2	-0.5	-5.3	-3.2	
7.1	-3.4	1.6	0.7	0.7	-0.1	1.2	0.9	1.0	0.2	-0.6	-5.4	-3.0	
6.8	-3.1	1.8	0.7	0.6	0.1	1.2	1.0	1.2	0.1	-0.7	-5.4	-2.7	
6.1	-2.9	2.0	0.9	0.4	0.4	1.2	1.0	1.4	0.1	-0.9	-5.5	-2.5	
5.2	-2.7	2.2	1.1	0.2	0.7	1.3	1.0	1.5	0.1	-1.0	-5.5	-2.3	
4.2	-2.6	2.4	1.3	-0.1	0.9	1.3	1.0	1.6	0.1	-1.2	-5.5	-2.1	

Table C.7: The bin content of the histogram of the best fit value for the branching ratio (%) of $(\Xi^-, {}^{12}\mathrm{C})_{\mathrm{atom}} \rightarrow {}^{12}_{\Lambda\Lambda}\mathrm{B}^* + \mathrm{n}$, shown as a dashed curve in Figure 5.8. The histogram has 378 bins with the lower and upper edges of 2.375 and 11.825 respectively.

bins 1–28	bins 29–56	bins 57–84	bins 85–112	bins 113–140	bins 141–168	bins 169–196	bins 197–224	bins 225–252	bins 253–280	bins 281–308	bins 309–336	bins 337–364	bins 365–378
0.0	0.3	0.0	0.0	0.0	0.0	0.0	0.0	0.0	0.0	0.0	0.0	0.0	0.0
0.0	0.0	0.0	0.1	0.0	0.0	0.0	0.0	0.0	0.0	0.0	0.0	0.0	0.0
0.0	0.0	0.0	0.0	0.0	0.0	0.0	0.0	0.0	0.0	0.0	0.0	0.0	0.0
0.0	0.0	0.0	0.0	0.0	0.0	0.0	0.0	0.0	0.0	0.0	0.0	0.0	0.0
0.0	0.0	0.0	0.0	0.0	0.0	0.0	0.0	0.0	0.0	0.0	0.0	0.0	0.0
0.0	0.0	0.0	0.0	0.0	0.0	0.0	0.0	0.0	0.0	0.0	0.0	0.0	0.0
0.0	0.0	0.0	0.0	0.0	0.0	0.0	0.0	0.0	0.0	0.0	0.0	0.0	0.0
0.0	0.0	0.0	0.0	0.0	0.0	0.0	0.0	0.0	0.0	0.0	0.0	0.0	0.0
0.0	0.0	0.0	0.0	0.0	0.0	0.0	0.0	0.0	0.0	0.0	0.0	0.0	0.0
0.0	0.0	0.0	0.0	0.0	0.0	0.0	0.0	0.0	0.0	0.0	0.0	0.0	0.0
0.0	0.0	0.0	0.0	0.0	0.0	0.0	0.0	0.0	0.0	0.0	0.0	0.0	0.0
0.0	0.0	0.0	0.0	0.0	0.0	0.0	0.0	0.0	0.0	0.0	0.0	0.0	0.0
0.0	0.0	0.0	0.0	0.0	0.0	0.0	0.0	0.0	0.0	0.0	0.0	0.0	0.0
0.0	0.0	0.0	0.0	0.0	0.0	0.0	0.0	0.0	0.0	0.0	0.0	0.0	0.0
0.0	0.0	0.0	0.0	0.0	0.0	0.0	0.0	0.0	0.0	0.0	0.0	0.0	
0.0	0.0	0.0	0.0	0.0	0.0	0.0	0.0	0.0	0.0	0.0	0.0	0.0	
0.0	0.0	0.0	0.0	0.0	0.0	0.0	0.0	0.0	0.0	0.0	0.0	0.0	
0.0	0.0	0.0	0.0	0.0	0.0	0.0	0.0	0.0	0.0	0.0	0.0	0.0	
0.0	0.0	0.0	0.0	0.0	0.0	0.0	0.0	0.0	0.0	0.0	0.0	0.0	
0.0	0.0	0.0	0.0	0.0	0.0	0.0	0.0	0.0	0.0	0.0	0.0	0.0	
1.3	0.0	0.0	0.0	0.0	0.0	0.0	0.0	0.0	0.0	0.0	0.0	0.0	
2.1	0.0	0.0	0.0	0.0	0.0	0.0	0.0	0.0	0.0	0.0	0.0	0.0	
2.8	0.0	0.0	0.0	0.0	0.0	0.0	0.0	0.0	0.0	0.0	0.0	0.0	
2.9	0.0	0.0	0.0	0.0	0.0	0.0	0.0	0.0	0.0	0.0	0.0	0.0	
2.7	0.0	0.0	0.0	0.0	0.0	0.0	0.0	0.0	0.0	0.0	0.0	0.0	
2.2	0.0	0.0	0.0	0.0	0.0	0.0	0.0	0.0	0.0	0.0	0.0	0.0	
1.5	0.0	0.0	0.0	0.0	0.0	0.0	0.0	0.0	0.0	0.0	0.0	0.0	
0.9	0.0	0.0	0.0	0.0	0.0	0.0	0.0	0.0	0.0	0.0	0.0	0.0	

Table C.8: The bin content of the histogram of the lower limit on the branching ratio (%) of $(\Xi^-, {}^{12}\mathrm{C})_{\mathrm{atom}} \rightarrow {}^{12}_{\Lambda\Lambda}\mathrm{B}^* + \mathrm{n}$, shown as the lower edge of the dashed band in Figure 5.8. The histogram has 378 bins with the lower and upper edges of 2.375 and 11.825 respectively.

bins 1–28	bins 29–56	bins 57–84	bins 85–112	bins 113–140	bins 141–168	bins 169–196	bins 197–224	bins 225–252	bins 253–280	bins 281–308	bins 309–336	bins 337–364	bins 365–378
0.7	7.6	1.4	5.6	4.9	2.7	3.9	4.1	3.7	4.7	3.5	2.8	1.5	6.2
0.7	6.8	1.5	5.6	5.2	2.5	4.1	4.1	3.6	4.9	3.6	2.7	1.5	6.5
0.6	6.2	1.4	5.5	5.4	2.3	4.3	4.0	3.6	4.9	3.5	2.6	1.5	6.9
0.6	5.8	1.4	5.3	5.6	2.1	4.4	4.0	3.5	5.0	3.6	2.4	1.7	6.9
0.6	5.4	1.5	4.9	5.5	2.1	4.6	4.0	3.5	4.9	3.7	2.4	1.5	7.3
0.5	4.9	1.5	4.3	5.5	2.0	4.7	4.0	3.4	5.0	3.7	2.3	1.7	7.7
0.6	4.6	1.6	3.7	5.4	2.1	4.6	3.9	3.3	4.9	3.7	2.1	1.9	7.8
0.8	4.3	1.9	3.1	5.2	2.1	4.6	3.8	3.1	4.9	3.7	2.0	1.9	8.0
1.3	4.0	2.2	2.5	5.0	2.2	4.6	3.7	3.1	4.7	3.7	1.9	1.9	8.5
2.5	3.7	2.7	2.2	4.7	2.2	4.5	3.7	3.0	4.7	3.7	1.7	2.1	8.4
3.8	3.5	3.2	2.0	4.4	2.2	4.5	3.6	3.0	4.6	3.8	1.7	2.0	8.4
4.8	3.3	3.8	1.9	4.1	2.2	4.4	3.5	2.8	4.4	3.8	1.7	2.2	8.6
5.2	3.0	4.4	2.1	3.8	2.1	4.3	3.4	2.8	4.4	3.7	1.6	2.2	9.0
5.1	2.7	4.9	2.4	3.7	2.1	4.2	3.4	2.7	4.2	3.8	1.5	2.4	9.1
4.8	2.3	5.1	2.8	3.5	2.1	4.2	3.3	2.8	4.1	3.8	1.4	2.6	
4.7	1.9	5.3	3.1	3.4	2.0	4.1	3.3	2.8	4.0	3.8	1.5	2.8	
4.6	1.5	5.3	3.5	3.4	2.0	3.9	3.3	2.9	3.9	3.7	1.4	3.0	
5.2	1.2	5.2	3.8	3.5	1.9	3.9	3.4	3.0	3.8	3.7	1.4	3.2	
6.3	1.2	5.0	4.0	3.6	2.0	3.8	3.4	3.1	3.7	3.8	1.3	3.4	
7.6	1.0	4.8	4.0	3.8	2.1	3.8	3.4	3.3	3.6	3.6	1.3	3.5	
9.1	1.0	4.7	4.0	3.9	2.1	3.8	3.4	3.4	3.6	3.5	1.2	3.7	
10.5	1.0	4.6	4.0	3.9	2.2	3.8	3.5	3.6	3.5	3.5	1.2	3.9	
11.2	1.1	4.7	4.0	3.9	2.4	3.9	3.5	3.8	3.5	3.5	1.3	4.3	
11.5	1.2	4.8	3.9	3.8	2.7	3.8	3.6	4.0	3.5	3.5	1.3	4.5	
11.1	1.2	4.9	4.1	3.7	2.9	3.9	3.6	4.2	3.4	3.3	1.5	4.7	
10.3	1.3	5.1	4.2	3.6	3.1	4.0	3.6	4.3	3.5	3.2	1.3	5.2	
9.4	1.4	5.3	4.5	3.3	3.4	4.0	3.6	4.5	3.5	3.1	1.5	5.5	
8.4	1.4	5.5	4.7	3.0	3.7	4.0	3.6	4.6	3.4	2.9	1.5	5.7	

Table C.9: The bin content of the histogram of the upper limit on the branching ratio (%) of $(\Xi^-, {}^{12}\mathrm{C})_{\mathrm{atom}} \rightarrow {}^{12}_{\Lambda\Lambda}\mathrm{B}^* + \mathrm{n}$, shown as the lower edge of the dashed band in Figure 5.8. The histogram has 378 bins with the lower and upper edges of 2.375 and 11.825 respectively.

Bibliography

[1] M.R. Woloshyn, Nucl. Phys. A **A543**, 99c (1992); F. Butler *et al.*, Phys. Rev. Lett. **70**, 2849 (1993); C. Michael *et al.*, Phys. Rev. D **51**, 3745 (1995); M. Goeckeler *et al.*, Phys. Lett. B **391**, 388 (1997).

[2] P. E. Hodgson, *Nuclear Reactions and Nuclear Structure*, Clarendon Press, Oxford (1971); G. R. Satchler, In: *Isospin in Nuclear Physics*, North-Holland, Amsterdam (1969); W. J. Thompson, AIP Conference Proceedings **69**, 204 (1981).

[3] G. Alexander *et al.*, Phys. Rev. **173**, 1452 (1968); B. Sechi-Zorn *et al.*, Phys. Rev. **175**, 1735 (1968); G. A. Kadyk *et al.*, Nucl. Phys. **B27**, 13 (1971); Alexander *et al.*, Phys. Rev. Lett. **7**, 348 (1961).

[4] R. Engelmann *et al.*, Phys. Lett. **21**, 587 (1966); F. Eisele *et al.*, Phys. Lett. **B37**, 204 (1971).

[5] M. M. Nagels *et al.*, Phys. Rev. **D12**, 744 (1975); **D15**, 2547 (1977); **D20**, 1633 (1979); P. M. M. Maessen *et al.*, Phys. Rev. **C40**, 226 (1989); Nucl. Phys. **A547**, 245c (1992).

[6] B. Holzenkamp *et al.*, Nucl. Phys. **A500**, 485 (1989); A. Reuber *et al.*, Czech. J. Phys. **42**, 1115 (1992).

[7] T.A. Rijken *et al.*, Phys. Rev. C **59**, 21 (1999).

[8] M. Ieiri *et al.*, Nucl. Phys. **A639**, 21c (1998).

[9] M. May *et al.*, Phys. Rev. Lett. **47**, 1106 (1981).

[10] C. Milner *et al.*, Phys. Rev. Lett. **54**, 1237 (1985).

[11] D.J.Millener *et al.*, Phys. Rev. C **38**, 2700 (1988).

[12] W. Brükner *et al.*, Phys. Lett. **79B**, 157 (1978).

[13] M. May *et al.*, Phys. Rev. Lett. **47**, 1106 (1981).

[14] M. May *et al.*, Phys. Rev. Lett. **51**, 2085 (1983).

[15] T. Nagae, In: *Proceedings of 23rd INS symposium on Nuclear and Particle Physics with meson beams in the 1 GeV/c region*, Universal Academic Press, Tokyo, 175 (1983).

[16] R. H. Dalitz, it International Symposium on Exotic Atoms and Nuclei, June 1995, Hakone, Japan.

[17] E. Hiyama at al, Phys. Rev. C **53**, 2075 (1996).

[18] T. Nagae at al, Phys. Rev. Lett. **80**, 1065 (1998).

[19] R. Sawafta *et al.*, Nucl. Phys. **A639**, 103c (1998).

[20] T. Harada *et al.*, Nucl. Phys. **A507**, 715 (1998).

[21] T. Harada, Nucl. Phys. **A639**, 185c (1998).

[22] C. B. Dover and A. Gal, In: *Progress in Particle and Nuclear Physics*, Pergamon Press, Oxford (1984).

[23] Y.Yamamoto *et al.*, Prog. Theor. Phys. Suppl. **117**, 361 (1994).

[24] A. J. Baltz *et al.*, Phys. Lett. **123B**, 9 (1983).

[25] M. May, private communications.

[26] C. B. Dover *et al.*, Nucl. Phys. **A572**, 85 (1994).

[27] M. Danysz *et al.*, Phys. Rev. Lett. **11**, 20 (1963).

[28] D. J. Prowse, Phys. Rev. Lett. **17**, 782 (1966)

[29] S. Aoki *et al.*, Prog. Theor. Phys. **95**, 1287 (1991).

[30] A. R. Bodmer *et al.*, Nucl. Phys. **A468**, 653 (1987).

[31] C. B. Dover *et al.*, Annals of Phys. **146**, 309 (1983).

[32] D. H. Wilkinson *et al.*, Phys. Rev. Lett. **8**, 397 (1959).

[33] J. Catala *et al.*, In: *"Proceedings of the International Conference on Hypernuclear Physics"*, Argonne, Illinois 758 (1969).

[34] A. S. Mondal *et al.*, Nuovo Cim. **54A**, 333 (1979).

[35] A. Bechdolff *et al.*, Phys. Lett. **26B**, 174 (1968).

[36] J. K. Ahn *et al.*, Phys. Rev. C **58**, 1306 (1998);

[37] P. H. Pile *et al.*, Nucl. Instr. Meth. **A321**, 48 (1992).

[38] B. Bassaleck, private communications.

[39] Y.Yamamoto *et al.*, Prog. Theor. Phys. Suppl. **117**, 281 (1994).

[40] F. Merrill, PhD thesis, Carnegie Mellon University, 1995.

[41] R. C. Byrd *et al.*, Nucl. Instr. Meth. **A313**, 437 (1994).

[42] Myung Shin Chung, PhD thesis, Korea University.

[43] C.Dover *et al.*, Phys. Rep. **184**, 24 (1989).

[44] C. Baltay *et al.*, Phys. Rev. D **9**, 49 (1974).

[45] T.Ijima *et al.*, Nucl. Phys. **A546**, 588 (1992).

[46] D.Zhu *et al.*, Phys. Rev. Letters **67**, 2268 (1991).

[47] Y. Akaishi *et al.*, Nucl. Phys. **A585**, 367 (1995).

[48] D.J.Millener *et al.*, Prog. Theor. Phys. Suppl. **117**, 307 (1994).

[49] Y. Nara *et al.* Nucl. Phys. **A614**, 433 (1997); J. K. Ahn *et al.* Nucl. Phys. **A625**, 231 (1997).

[50] J. K. Tuli, "Nuclear Wallet Cards", Brookhaven National Laboratory, New York, Appendix V (1995).

[51] G.J. Feldman and R.D. Cousins, Phys. Rev. **D57** 3873 (1998).

[52] M. L. Goldberger and K. M. Watson, "Collision Theory", Wiley, New York (1964).

[53] J. Hüfner *et al.*, Nucl. Phys **A234**, 429 (1974).